Cerium dioxide - based Nanomaterials and Investigation of Their Photocatalytic Performances

By

Sàisài Yuán

A DISSERTATION

Presented to the Department of Material Science

at Kyushu Institute of Technology

In Partial Fulfillment of the Requirements

for The Degree of Doctor of Philosophy

Major : Applied Chemistry

Under the supervision of Professor Teruhisa Ohno

Kitakyushu, Japan

January 2018

Contents

Chapter 1 General Introduction

1.1 Research background

The environmental pollution and energy shortages are becoming serious tissues with the rapid development of societies in 21st century. According to the monitoring data (Figure 1.1a ~ c) from National Oceanic and Atmospheric Administration (NOAA), the emissions of greenhouse gases have dramatically increased recent years, especially the carbon dioxide (CO_2), nitrous oxide (N_2O), and methane. More importantly, these greenhouse gases are dominated by the fossil combustion (Figure 1.1d). With the increase in world population and the rampant unregulated industrial growth, leading to accelerated energy consumption, unabated release of toxic agents and industrial waste into the air. Worse, it has resulted in pollution-related diseases, global warming, and abnormal climatic changes. Although, nuclear energy is a clean and sustainable energy source, it is very dangerous. For instance, the earthquake-tsunami disaster of March 11, 2011, which crippled the nuclear reactors in Fukushima, Japan, has raised serious concerns due to nuclear waste and coolants polluted with radioactive materials. It should therefore be our goal to contribute to the development of environmentally harmonious, ecologically clean and safe, sustainable, and energy-efficient chemical technologies, the most urgent challenges scientists are facing today. And green or sustainable chemistry has attracted the researchers' attention, which could help us solving the series of crises. In 1972, Fujishima and Honda[1] discovered the phenomenon of photocatalytic splitting of water on a TiO_2 electrode under ultraviolet (UV) light. Since then, enormous efforts have been devoted to the research of photocatalysts. It is a great discovery and it cleaves a new field, providing people a clean, safe, and sustainable strategy to obtain energy from sunlight and purify the environment.

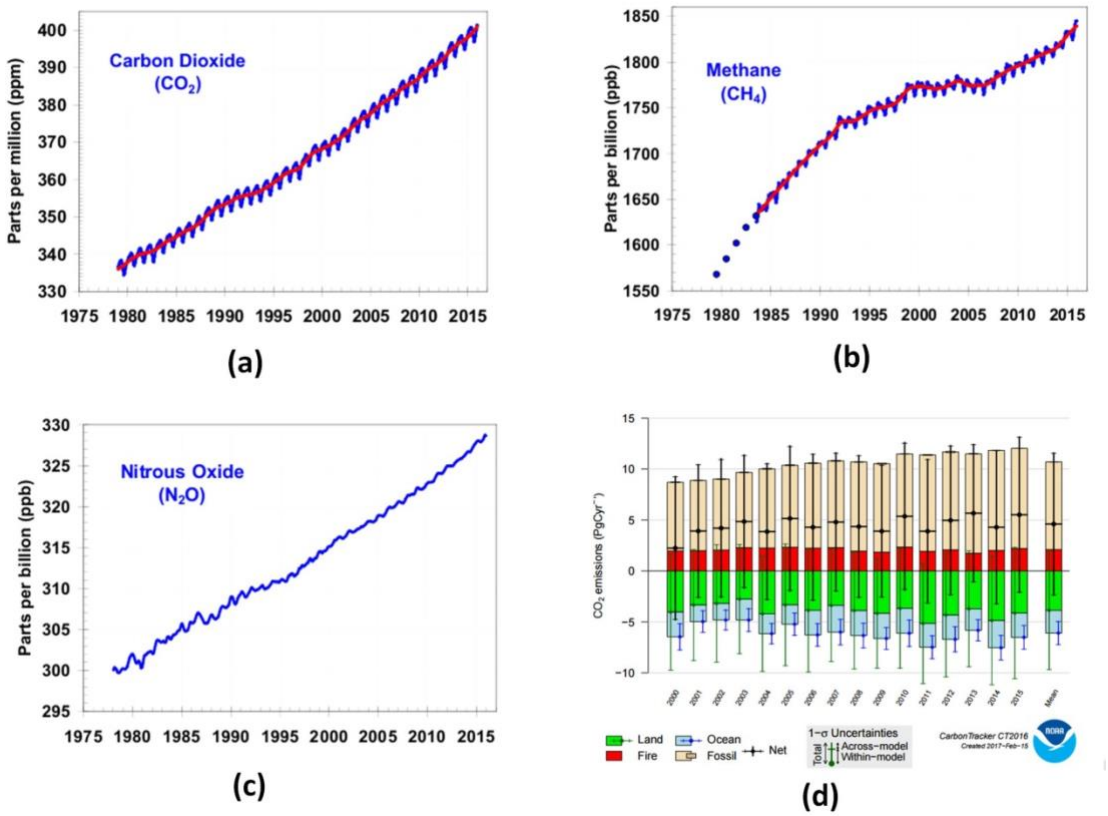

Figure 1.1. Greenhouse gases monitoring data from the NOAA.

In chemistry, photocatalysis is the acceleration of a photoreaction in the presence of a catalyst. Photocatalysis is particularly relevant in order to realize chemical transformations of synthetic interest with a minimal environmental impact. In fact, photochemical reactions require milder conditions than thermal processes and may allow for the conception of short and efficient reaction sequences, minimizing side processes. In general, the photocatalytic cycle is comprised of three parts shown in Figure 1.2a. Firstly, with the illumination, a transition of photo – generated electrons from valence band to the conduction band, leaving an equal number of vacant holes. Secondly, the excited electrons and holes migrate to the surface. Thirdly, the photo – generated electrons and holes will participate the reduction and oxidation processes with absorbed substrates, respectively. Pollution, water, and CO_2 are the candidates of electron donors (D) and electron acceptors (A), in which the inexhaustibly abundant, clean, and safe energy of the sun can be harnessed for sustainable,

nonhazardous, and economically viable technologies, is a major advance in this direction. However, the recombination of electron – holes is the disease node for the prohibition of photocatalytic activity.

Titanium - oxide materials in different types and forms have shown great potential as ideal and powerful photocatalysts for various significant reactions due to their chemical stability, non - toxicity, and high reactivity. Investigations of well-defined photocatalytic reaction systems and of their detailed reaction mechanisms and kinetics using a number of molecular spectroscopies have led to the development of various Ti - oxide - based photocatalytic materials. In particular, photocatalysts have been employed for such significant applications (Figure 1.2b) as the purification of polluted water and air, self-cleaning glasses, tiles, and tents coated with Ti - oxide materials with unique photo - induced super hydrophilic, and bone - implant fixation using photofunctionalized titanium enabling more rapid and complete bone-titanium integration, just to name a few.[2] Investigations have also been carried out into the development of visible light-responsive Ti - oxide photocatalysts by adding small amounts of components such as cations and metal oxides by both chemical doping and physical – ion – implantation methods.[3] Moreover, it has also been possible to prepare Ti - oxide photocatalysts, enabling the absorption of light not only in the ultraviolet but also in the visible light wavelength region to operate effectively under natural sunlight irradiation.[4, 5]

Other semiconductors also have been investigated by researchers for photocatalytic applications. It wasn't until Kudo[6] et al. began doping the perovskite $SrTiO_3$ with metals such as Cr, Ru, Ir, Mn, Sb, Ta, Ni, and Rh, that quantum efficiencies started to increase. Rh (1 %) doped strontium titanate demonstrated a quantum efficiency of 5.2 % for hydrogen production at 420 nm, the highest value among the different dopants. In addition, other rear earth oxides also have been utilized for photocatalysis. For instance, CeO_2 has

been applied for pollution degrading, organic reaction and photoelectrochemical sensors due to the special transformation between Ce^{3+} and Ce^{4+}.[7-9] In 2009, an organic-polymer-based photocatalyst, graphitic carbon nitride (g - C_3N_4), was found to show sufficient redox power to dissociate water under visible light in a suspension system.[10] The compound was fabricated by simply calcining cyanamide in either air, or a nitrogen atmosphere.

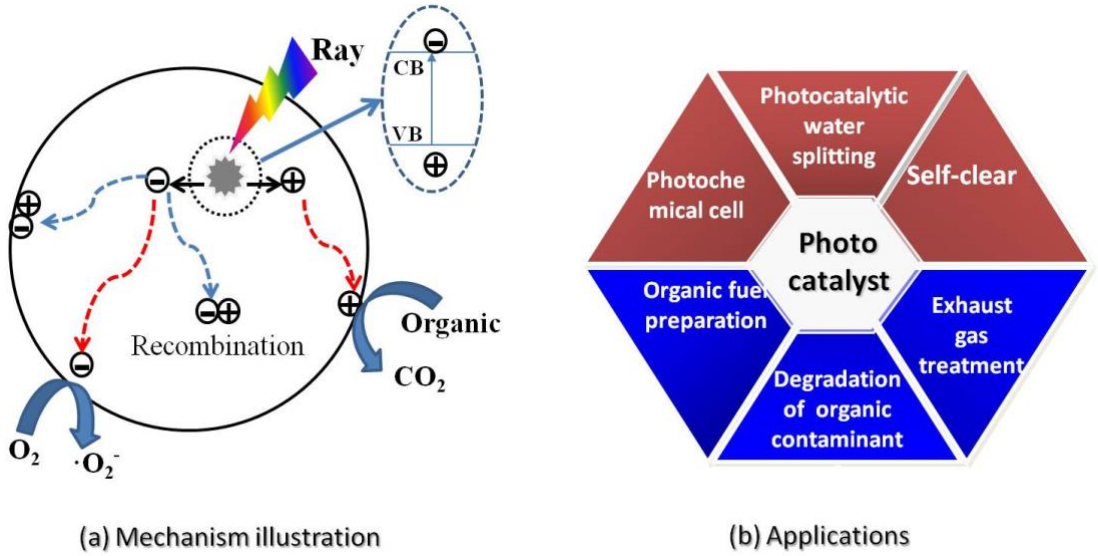

(a) Mechanism illustration (b) Applications

Figure 1.2. (a) Scheme of photocatalysis, (b) applications of photocatalysis.

1.2 Introduction of cerium dioxide

1.2.1 History of cerium dioxide

Cerium is the most abundant rare earth, which is far more abundant in the upper crust, 64 ppm, than any other rare earth elements it is more abundant than copper, 60 ppm, or tin, 2.3 ppm. However, the exact values of crustal abundance (average concentration in the earth's crust) are still controversial. Its high abundance, combined with excellent catalytic activity for a variety of reactions, makes cerium the element of choice for the automotive industry enabling the catalytic conversion of the exhaust system of automobiles.

Cerium is in the lanthanide group with an atomic number of 58. The electron configuration of cerium is $[Xe]4f^15d^16s^2$. Cerium has III and IV oxidation

states. Cerium (IV) oxide (CeO_2) is an oxide form of cerium metal, usually obtained by heating cerium metal, $Ce(OH)_3$, or any of Ce (III) oxosalts such as oxalate, nitrate or carbonate in air or oxygen. The dioxide CeO_2 has fluorite structure, with a face-centered cubic unit cell and space group of Fm-3m. In each unit cell, the lattice constant is 5.411 Å; each cerium ion is surrounded by eight equivalent oxygen anions, and each anion is tetrahedrally coordinated by four cerium cations. (See Figure 1.3) The eight coordination sites are alternately empty and occupied by a cerium cation. This clearly shows that there are large vacant octahedral holes in the structure, and this feature plays an important role in the applications of cerium oxides. Also, CeO_2 owns three kinds of crystal facets (See Figure 1.3), (111), (110), and (100), which are closely related with their performance.

Cerium oxide is one of the most important earth metal oxides, which has been extensively used in various applications including applications in UV blockers, polishing materials, catalysts, electrolytes, sensors, and solar cells due to its favorable properties including chemical stability, redox property, and high oxygen storage capacity.[11-23] Notably, ceria is a vital component in three-way catalysts (TWCs) mainly due to its high degree of tolerance to reversible oxygenation-deoxygenation cycles without disruption of fluorite lattice structure. Their sizes, surface structure and shape can determine some unique properties and improve performances of nanomaterials, thus it is essential to investigate the controllable morphology of ceria nanomaterials. So all kinds of ceria nanomaterials, such as nanorods, nanotubes, nanospheres, nanocubes, and nanowires, are fabricated and their properties have been examined.[8, 24-69]

The main defect in ceria nanocrystals originates in oxygen vacancies.[70, 71] Oxygen vacancies can be produced via the following defect reaction:

$$O_O^X \leftrightarrow V_O^{\bullet\bullet} + 2e' + \tfrac{1}{2} O_2$$

where O_O^X, $V_O^{\cdot\cdot}$, and e' are oxide ions in the lattice, doubly charged oxygen vacancies, and electrons in the conduction band made up of Ce 4f energy states, respectively. The transformation between Ce^{3+} and Ce^{4+} has a great impact on the formation of the oxygen vacancies. The higher Ce^{3+} concentration of the ceria nanomaterials that exist, the more defects form. Based on density functional theory calculations,[72-80] the stability follows the sequence: (111) > (110) > (100), while the activity follows the opposite order. The energy required to form oxygen vacancies on the (111) surface is greater than those on the (110) and (100) surfaces, so the amount of oxygen vacancies on different planes is different. There are more oxygen vacancies on (110) and (100) planes, which are favourable in catalytic performance.

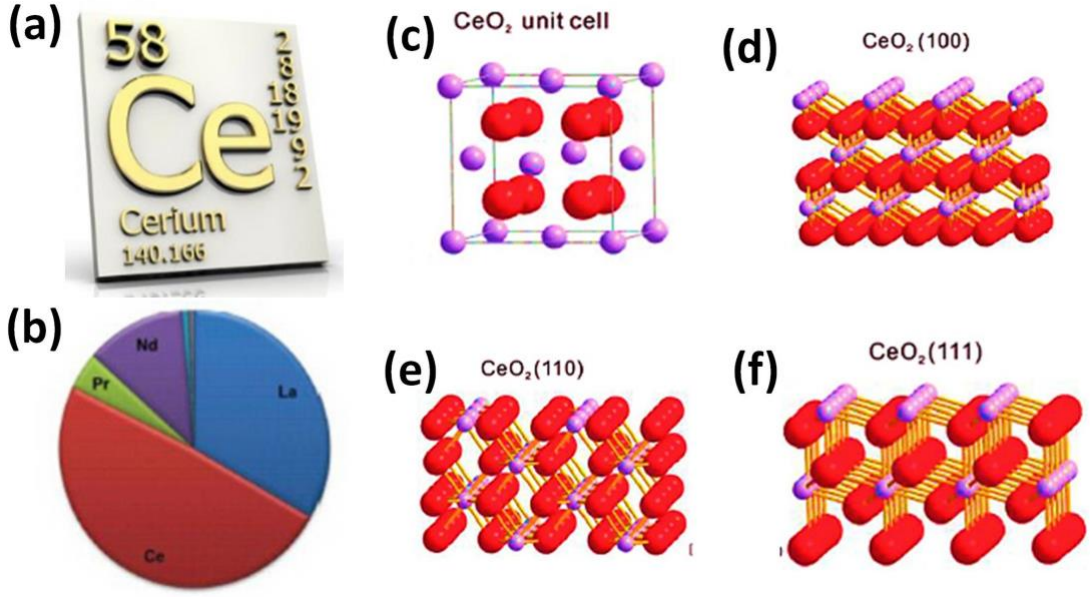

Figure 1.3. (a) element information of cerium, (b) ratio of cerium in earth, (c) unit cell of CeO_2, (d) ~ (f) three kinds of crystal facets.

1.2.2 Preparation of cerium dioxide

Nanocubes

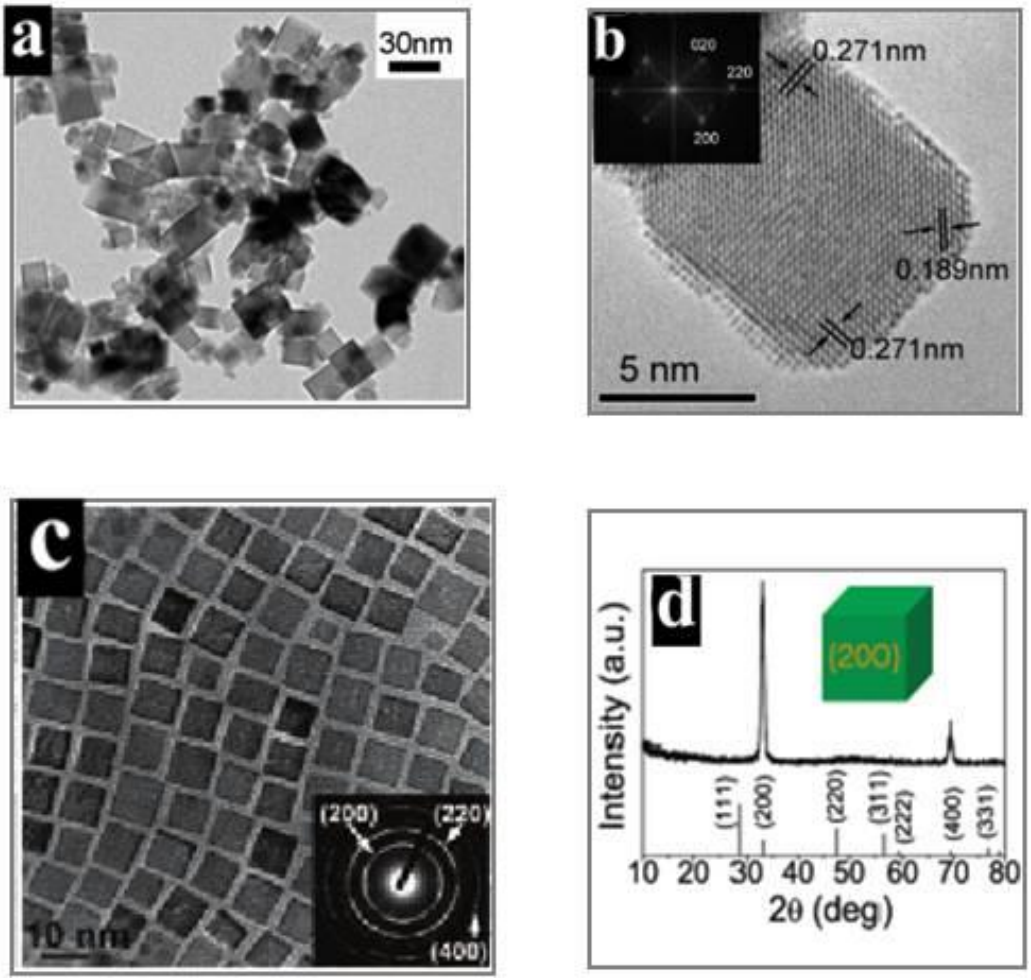

Figure 1.4. (a) ~ (c) TEM images of ceria nanocubes; the insets are SAED patterns and individual NPs. (d) A typical XRD pattern of the ceria nanocubes assembled on a Si wafer; the inset is the schematic illustration of the facets of an individual cube.[81]

The hydrothermal/solvothermal treatment is a common method to synthesize inorganic nanomaterials. It involves the use of an autoclave under controlled temperature and pressure with the reaction in an aqueous solution. The reflux of solvent vapour can elevate the reaction temperature and promote the liquid

to reach the pressure of vapour saturation. The internal pressure produced in an autoclave is determined by the temperature and the amount of solution.

The anions in solvents have a great influence on the morphology and properties of CeO_2 nanomaterials synthesized via a hydrothermal/solvothermal treatment. The precursor of the cubic ceria in Figure 1.4 is $Ce(NO_3)_3{\cdot}6H_2O$. The anion has a selective interaction with specific facets, which leads to the growth of nanocrystals with varying morphologies. The NO_3^- anions have a strong interaction with (100) planes and results in the anisotropic growth of (110) planes. Thus CeO_2 nanocubes enclosed with (100) planes are prepared. Compared with Figure 1.4a, Figure 1.4c is monodisperse, which is attributed to adding a capping reagent. The HRTEM images in part b of Figure 1.4 combine with SAED pattern analysis (inset) diaplays the clear (200) and (220) lattice fringes with the interplanar spacings of 0.271nm and 0.189 nm, respectively, implying that the CeO_2 nanocubes are only enclosed by (200) planes. The SAED of Figure 1.4c inside and the XRD pattern of Figure 1.4d both also confirm the (200) planes of the cubic ceria.

Nanorods

Morphology - controlled synthesis of nanostructured materials, such as single - crystalline one - dimensional (1D) nanomaterials (wires, rods, belts, and tubes), may present an opportunity for the synthesis of catalytic materials with such desirable features because these novel materials nucleate and grow in an epitaxial manner, exposing defined crystal planes. Moreover, they are usually synthesized under unusual conditions, and some reactive crystal planes may be obtained. Figure 1.5 (a) ~ (c) is one sample synthesized by the solvothermal treatment method. Figure 1.5 (b) & (c) clearly show the (100) and (110) lattice fringes with the interplanar spacing of 0.27 nm and 0.19 nm. The (100) and (110) planes are predominantly exposed in this ceria nanorods, which is associated with its properties.

Electrochemical deposition is another way to obtain nanomaterials by the aid of an electric current at specific conditions. The synthesized nanomaterials can be influenced by the current density, the organic additive, the pH value, temperature and other factors. Increased current density is helpful to the formation of nanocrystals. The hexagonal ceria with (110) as predominant exposed planes in Figure 1.5 (d) is synthesized by facile electrochemical method. The aligned CeO_2 nanorods were directly grown on Ti substrates via an electrochemical assembly process without any templates or surfactants. Due to their special redox capacity, the nanorods were used in photocatalysis.

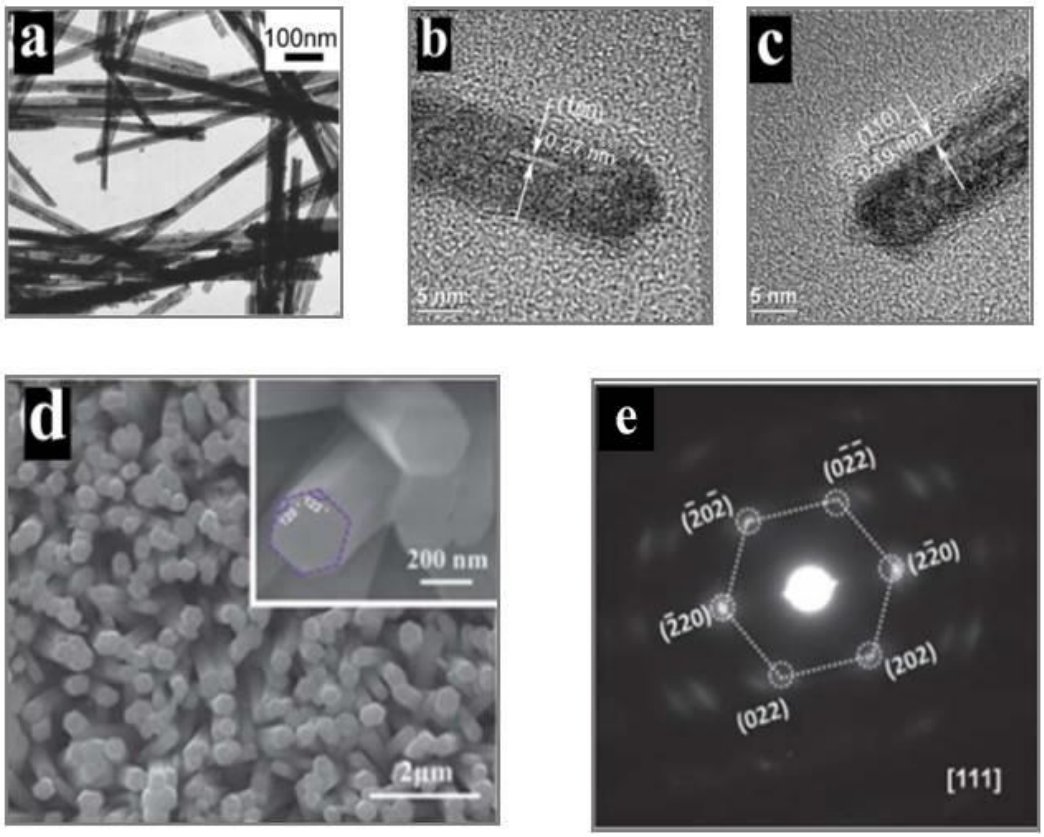

Figure 1.5. (a) TEM image of ceria nanorods;[31] (b) & (c) HRTEM images of ceria nanorods;[82] (d) SEM image of ceria nanorods grown on Ti substrates;[83] (e) SAED patterns.

Hollow structures

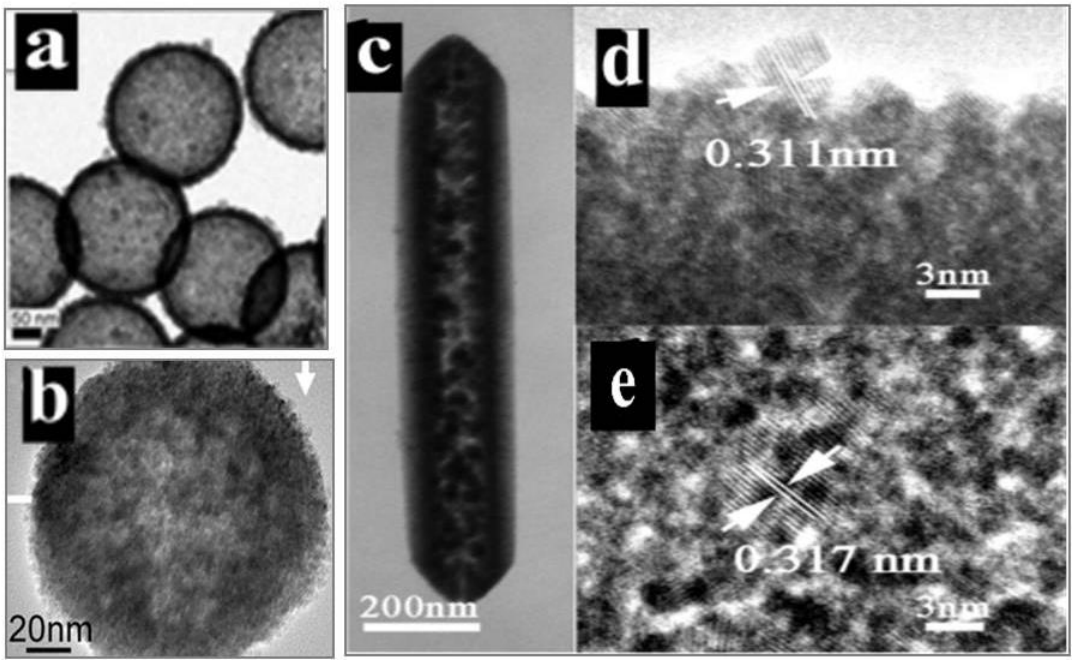

Figure 1.6. (a) & (b) TEM image of ceria hollow spheres;[54] (c) TEM image of ceria nanotubes,[53] and HRTEM images from shell (d) and interior space

Hollow materials with interiors or voids and pores are a class of lightweight nanostructured matters that promise many future technological applications, and they have received significant research attention in recent years. On the basis of well-known physicochemical phenomena and principles, for example, several solution-based protocols have been developed for the general preparation of these complex materials under mild reaction conditions.

In this section, we present a comprehensive overview of synthetic approaches for hollow structures. We broadly divide these approaches into four categories: (1) conventional hard templating synthesis, (2) sacrificial templating synthesis, (3) soft templating synthesis, and (4) template-free methods.

The perfect ceria hollow spheres (Figure 1.6a) are synthesized by conventional hard templating method with the silica template particles. The CeO_2 nanomaterials synthesized by template methods are uniform in size and easily

be controlled and operated. Moreover, these CeO_2 hollow structures often have a high surface area due to the two surfaces, which may be favourable for application in catalytic reactions. However, it is difficult to remove the template completely. The remaining templates can influence the properties of CeO_2. So exploring a better method to remove the template is very important in the synthesis of CeO_2 hollow structures.

Figure 1.6b shows another type of ceria hollow sphere, which is prepared by the template-free method via Ostwald ripening process. Ostwald ripening is a physical phenomenon that has been well known for more than a century. This process can be briefly summarized as "the growth of larger crystals from those of smaller size which have a higher solubility than the larger ones". Compared with template method, this method is economical and environmentally friendly. However, the mechanism of the intermediate state is difficult to understand.

In order to obtain the ceria hollow nanotubes, another theory has been applied, which is Kirkendall Diffusion.[53] The Kirkendall effect is a consequence of the different diffusivities of atoms in a diffusion couple causing a supersaturation of lattice vacancies. Ceria hollow nanotubes (Figure 1.6c) have been obtained by this theory. HRTEM images from shell (Figure 1.6d) and interior space (Figure 1.6e) show that the lattice spacing of 0.317 and 0.311 for the (111) planes is typical of cubic ceria structure.

Methods for CeO_2 preparation

The synthetic methods are divided into two categories: chemical and physical methods. Ball milling is the major physical method. The chemical methods, such as hydrothermal, co-precipitation and sol - gel methods, are the most common methods in producing ceria nanoparticles for catalytic applications. Co-precipitation synthetic method is another extensively used approach for preparing nanomaterials. This method has typical advantages: (i) simple and

rapid preparation process (ii) easily controllable particle size and composition, and (iii) flexible in modifying the particle surface state and overall homogeneity. Sol-gel method is widely used in ceramics industry and materials science for producing solid materials such as ceramic fibers and dense films. The method is highly suitable for the fabrication of metal oxides. It is easy to perform and does not need any special conditions.

1.2.3 Cerium dioxide – based nanomaterials

In order to improve the performance of pristine cerium dioxide, adding other materials is a direct and effective route. So many strategies have been explored by the researchers, planetary grinding, ions doping, noble metals loading, In situ growth, etc.

1.2.4 Applications

Cerium oxide based materials have been applied in numerous areas, including catalysis, ceramics, fuel cells, glass, and phosphors.[11, 84-86] All these applications are based on its potential redox chemistry between Ce^{3+} and Ce^{4+} , high oxygen affinity and absorption/excitation energy bands associated with electronic structure. The redox property and Lewis acid and base sites on ceria make this oxide suitable as a catalyst or a support for chemical reactions. Ceria is an important ingredient in three-way catalysts for catalytic converters to convert the toxic gases in automobile emissions to less or non-toxic ones. Due to its oxygen storage and release capability, ceria can oxidize the toxic carbon monoxide to less toxic carbon dioxide, oxidize the unburnt hydrocarbons to carbon dioxide and water, and help reduce NO_x to N_2 gas. In catalytic converters, ceria also acts as a stabilizer for high surface area support alumina and a sintering-resistant support for noble metals. It helps noble metal dispersion on its surface and provides oxygen to the supported metal particles for oxidizing the adsorbents. Ceria is of interest as a material for solid oxide fuel cell (SOFC) due to its decrease of internal electrical resistance in an

SOFC.[87-90] The internal resistance comes from both electrolyte, and the fuel and air electrode. Ceria-containing fuel electrode has lower susceptibility towards coke formation and is less sensitive to the fuel impurities such as sulfur. Oxygen vacancies are essential for ceria possessing these properties. Doped ceria has been reported as a low-temperature electrolyte for about fifty years, such as $Ce_{1-y}Gd_yO_{2-y/2-x}$, and $Ce_{1-y}Sm_yO_{2-y/2-x}$.[91] Around 500 - 650 °C in SOFC, ceria doped materials have high oxygen ion conductivity which enables ceria act as a good electrolyte.

1.3 Research purposes

Although the cerium dioxide materials are very attractive catalysts, there are some disadvantages that we should overcome. Firstly, we should explore a mild method to obtain the morphology controlled CeO_2 nanoparticles. Because pristine CeO_2 is bulk particles and its activity is greatly prohibited. We investigated various method for CeO_2 preparation, the detail information would be presented in following chapters.

Secondly, in order to fulfill with the requirement of visible light response photocatalysts , tuning the contents of cerium (III) and OVDs routes are utilized. In future, we will construct the cerium dioxide – based hybrid materials to improve the visible light absorption.

Lastly, the mechanisms of special morphologies formation and improved photocatalytic activity have been discussed.

Chapter 2 Preparation and properties of pristine cerium dioxide

2.1 Introduction

Hydrothermal, co-precipitation and sol - gel methods are the most general methods for preparation of ceria nanomaterials. In this chapter, we prepared bulk CeO_2, nano octahedron CeO_2 via solvothermal method. With the addition of ethanol, CeO_2 - Octa nano particles formed. Smaller particle size generated lager surface area, and the absorption of reactants improved a lot. However, the activity of CeO_2 – Octa was not excellent due to its low light harvest.

2.2 Experimental section

2.2.1 Materials

Cerium (III) Nitrate Hexahydrate (Wako) Assay min 98.0%;

Commercial cerium dioxide particles (HIGH PURITY CHEMICALS Co. Ltd.);

Ethanol (Wako) Assay min 99.5%;

Deionized water;

Polyvinylpyrrolidone K30 (Wako);

Acetaldehyde (SIGMA-ALDRICH) ACS reagent Assay min 99.5%;

Pure air (Taiyo Nippon Sanso) CO_2 < 0.1 ppm;

2.2.2 Synthesis of pristine cerium dioxide

Octahedral Cerium dioxide nanoparticles with ca. 120 nm in diameters were synthesized by a simple one-step solvothermal method with reaction in a mixed solution of water and ethanol with PVP (polyvinyl pyrrolidone) as a surfactant. Typically, 1.0 g of Cerium (III) nitrate hexahydrate and 0.10 g of PVP were dissolved in a mixture of C_2H_5OH (60 mL) and H_2O (20 mL) with magnetic stirring for 30 min. Then the suspension was transferred to a 100-mL Teflon-lined autoclave and heated at 180 °C for 24 h. After cooling to room temperature, the product was collected by centrifugation, washed with ethyl alcohol and water until the ionic strength was less than 10 μs/cm, and dried at

70 °C overnight. Finally, we obtained Octahedral Cerium dioxide nanoparticles, which was denoted as CeO_2 - Octa. For control experiments, ceria nanoparticles were obtained under same conditions as those described above but in the absence of ethanol and PVP, and the bulks were denoted as CeO_2 - pristine. All the samples will be reserved under black - UV illumination for photocatalytic evaluation.

2.2.3 Characterization

The CeO_2 materials were characterized using X - ray diffraction (XRD), field emission scanning electron microscopy (FESEM), ultraviolet-visible absorption spectroscopy (UV - vis), Brunauer-Emmett-Teller (BET) surface area.

The crystal structure and composition were determined by XRD using a Rigaku MiniFlex II X-ray diffractometer with a Cu-Kα radiation source (γ = 1.5405Å). The morphologies of the samples were observed by FESEM (JEOL, JSM-6701FONO). Nitrogen adsorption/desorption measurements were performed at 77 K using a Quantachrome Nova 4200e to calculate the specific surface area using the BET model. The pore size distribution was obtained from desorption-isotherm curves by the Barrett Joyner Halenda (BJH) method. Prior to measurements, the samples were degassed in vacuum at 180 ^{0}C for 3 h. Diffuse reflectance (DR) spectra were measured using a UV–vis spectrophotometer (Shimadzu, UV-2500PC) equipped with an integrating sphere unit (Shimadzu, ISR-240A). Raman spectra were obtained by a laser Raman spectrum (JASCO, NRS-5100).

2.2.4 Evaluation of activity

Photocatalytic activity of the samples was evaluated by photocatalytic decomposition of acetaldehyde in gas phase (Figure 2.1). Samples powder (150 mg), which had completed extinction of incident radiation, was spread on a glass dish, and the glass dish was put into a Tedlar bag (AS ONE Co. Ltd.)

with a volume of 125 mL mixed air (79% N_2, 21% O_2, <0.1 ppm of CO_2, 500 ppm of acetaldehyde). After 2-h adsorption equilibrium in the dark, the photocatalysts were exposed under the visible light. A light-emitting diode (LED; Lumileds, Luxeon LXHL - NRR8), which emitted light at a wavelength of *ca.* 435 nm with an intensity of 3.0 mW cm^{-2}, was used as visible-light irradiation source. In the photocatalysis process, generation of carbon dioxide and consumption of acetaldehyde were monitored by online gas

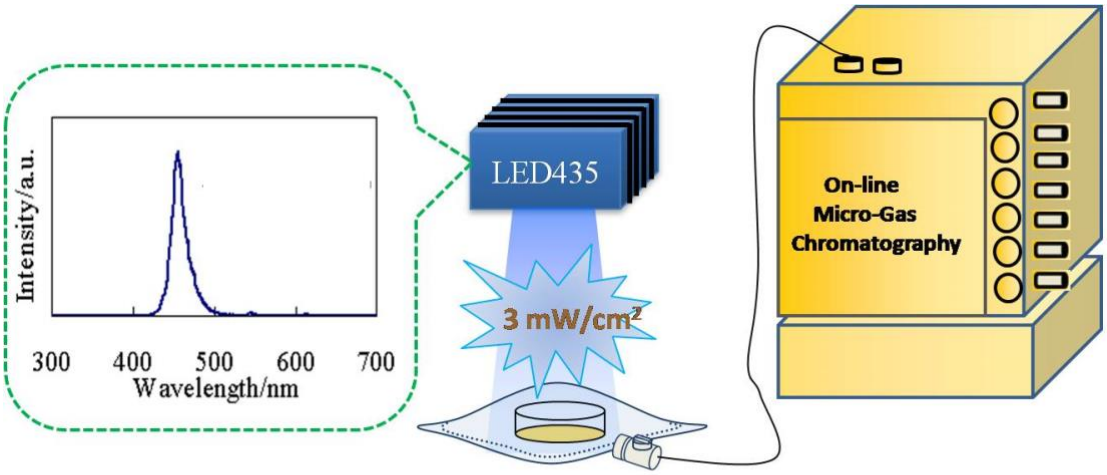

$$2CH_3CHO + 5O_2 \xrightarrow[3mW/cm^2]{LED435} 4CO_2 + 4H_2O$$

500 ppm 1000 ppm

chromatography (Agilent Technologies, 3000A Micro - GC, TCD detector) equipped with OV1 and PLOT - Q columns.

Figure 2.1. Schematic illustration of photoactivity evaluation.

2.3 Results and discussion

2.3.1 Structure and composition

FE - SEM

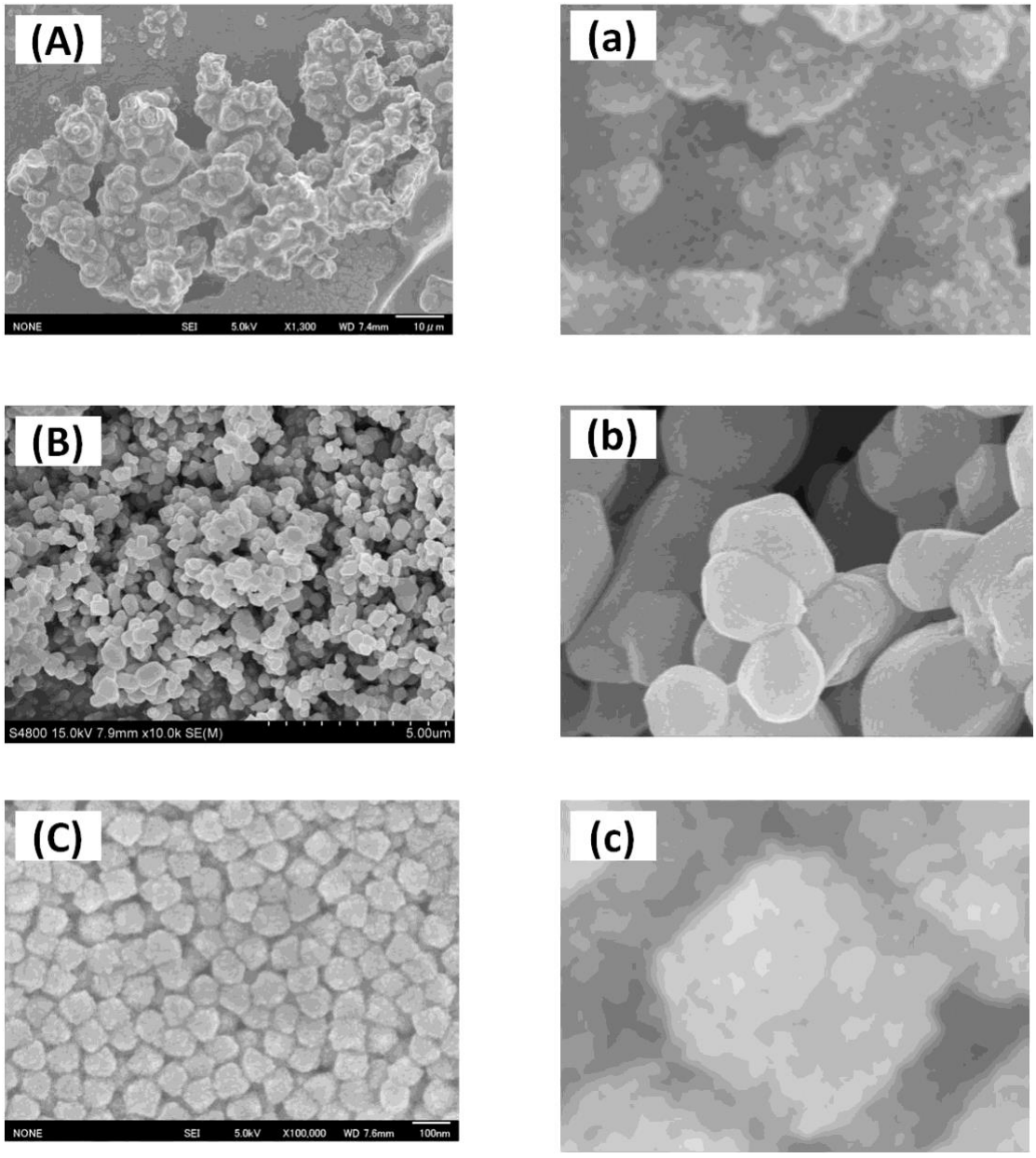

Figure 2.2. FE – SEM images of all the samples, (A) & (a) CeO_2-pristine, (B) & (b) CeO_2-HPC, (C) & (c) CeO_2-Octa.

The morphology information were characterized by FE – SEM technology. Figure 2.2 (A) & (a) show the pristine CeO_2, which were prepared via solvothermal method. Without PVP, the particles will aggregate together, and then form the bulk particles. The particle size of CeO_2 - pristine increased to the 200 nm ~ 2000 nm. It will greatly prohibit its performance. Compared with CeO_2 - pristine, the particle size of CeO_2 - HPC (Figure 2.2 (B) & (b)) decreased a lot (ca. 20 nm). Although the problem of particle size has been solved, the aggregation and monodispersity tissues still troubled us. When the ratio of ethanol and water was fixed to 60 mL and 20 mL, and the addition of PVP surfactant, the octahedral nanoparticles with excellent monodispersity would be obtained. As shown in Figure 2.2 (C) & (c), the particles exhibit octahedral morphology and the monodispersity is very great. The particle size is approximate 100 nm, which is under the nanoscale. We are convinced of that the performance of CeO_2 - Octa will be improved.

XRD patterns

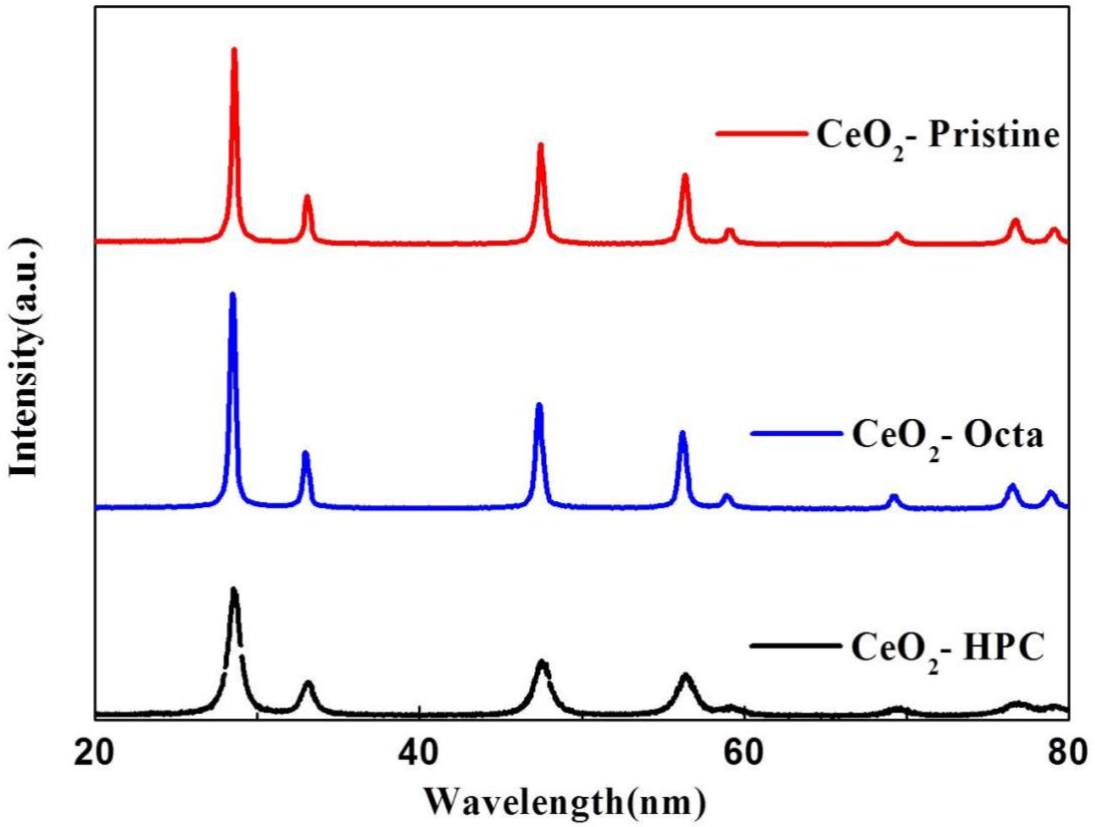

Figure 2.3. XRD patterns of all the samples.

The phase purity of the prepared products was estimated by the XRD patterns. Figure 2.3 Shows the XRD patterns of CeO_2 – pristine, CeO_2 – HPC and CeO_2 - Octa. All of the characteristic peaks were indexed to the face-centered cubic phase with space group Fm3m of ceria (JCPDS card no. 34-0394). No other peaks were detected, and the sharp peaks indicated that the high purity and the highly crystalline nature of CeO_2 – pristine and CeO_2 – Octa. The peaks of CeO_2 - HPC was relatively broad, demonstrating that the CeO_2 - HPC was composed of smaller crystals. The average primary particle size was ca. 8.7 nm (Table 2.1), which is according to the calculation with the Debye–Scherrer formula for the strongest peak (111). The calculated values of all the samples are coincide with the results of the FE – SEM images.

UV – vis spectra

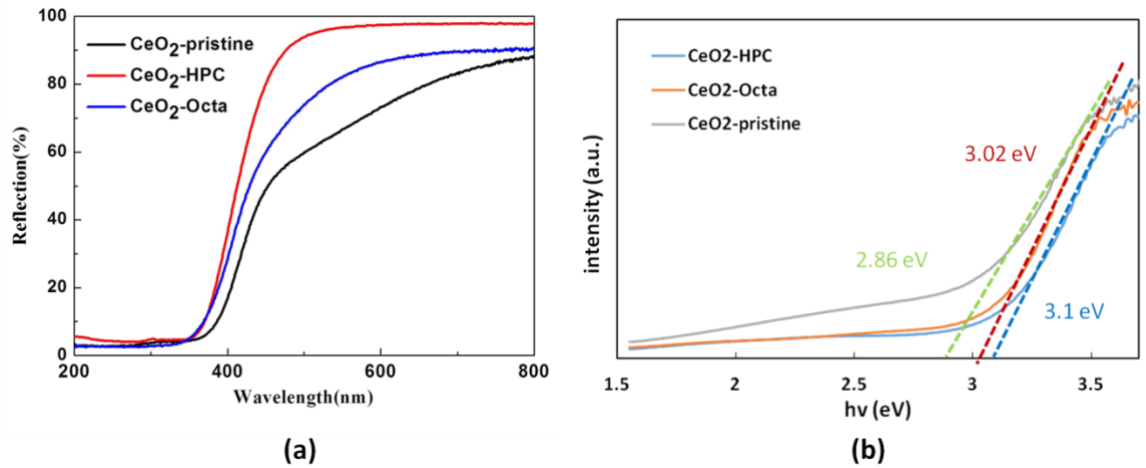

Figure 2.4. UV-vis spectra and KM transformed spectra of all the samples.

Optical information of all the samples will be shown in UV – vis spectra (Figure 2.4). There is a strong absorption band from 300 nm to 350 nm in the spectra, which is assigned to the charge transfer from O^{2-} in O 2p to Ce^{4+} in Ce 4f. Compared with CeO_2 – pristine, CeO_2 – HPC and CeO_2 – Octa have a relative blue shift. As semiconductor materials, the indirect band gap (Eg) can be calculated from the equation of $ahv = A (hv - Eg)^2$, where hv is the photon energy, a is the absorption coefficient, and A is a constant of CeO_2. Calculated Eg values for CeO_2 – HPC, CeO_2 - pristine and CeO_2 – Octa were 3.1 eV, 2.86 eV and 3.02 eV, respectively (Figure 2.4b). The possible reason is that The existence of quantum confinement effect due to the nanoscale size of the primary particles forming the CeO_2 – pristine, and CeO_2 – HPC resulted in a blue-shift in the UV-vis diffuse reflectance spectrum. Also, the UV – vis spectra we can confirm all the samples owned a partial of visible light absorption (wavelength > 400 nm). As a result, we could choose the LED 435 nm as the light source.

2.3.2 Photocatalytic activities of pristine cerium dioxide

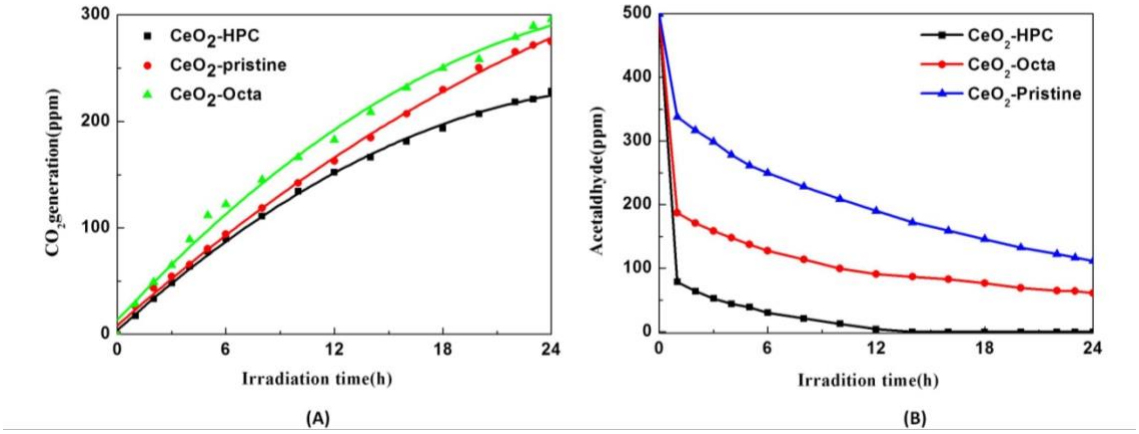

Figure 2.5. Photocatalytic activities of all the samples.

The photocatalytic activity of CeO_2 – pristine, CeO_2 – HPC and CeO_2 – Octa were examined in acetaldehyde decomposition reaction under visible light irradiation. Figure 2.5 (A) shows the CO_2 evaluation activities of all the samples. Figure 2.5 (B) shows the amount of acetaldehyde in the photocatalytic process. After 24 h visible light irradiation, the adsorption and degradation efficiencies of CeO_2 – pristine, CeO_2 – HPC and CeO_2 – Octa were ca. 76 %, 100 % and 88 %, respectively. This results could be ascribed to particle size effect. CeO_2 – HPC owns the least particle size (largest surface area showing Table 2.1), indicating that it can absorb more reactants. However, the activity of CeO_2 – HPC is disappointing, which is attributed to that the light absorption of CeO_2 – HPC at 435 nm wavelength is under 10 %. Photocatalytic activities of CeO_2 – pristine and CeO_2 – Octa have improved, and that of CeO_2 – Octa better than that of CeO_2 – pristine. One reason is that the visible light of both samples has increased, and another one is that the monodispersity of CeO_2 – Octa is much better than CeO_2 – HPC.

2.4 Conclusions and improvement

Table 2.1 BET results and calculated values from XRD patterns

Samples	Surface area/g.m^{-2}	Band gap/eV	Grain size/nm
CeO_2 - pristine	1.212	2.86	27.2
CeO_2 - Octa	11.213	3.02	22.1
CeO_2 - HPC	119.312	3.1	8.7

Calculated surface area and grain size values are shown in Table 2.1. Octahedral cerium dioxide nanoparticles with ca. 100 nm diameter were prepared via a simple solvothermal method. The surface area of CeO_2 – Octa is lager than that of CeO_2 – pristine, providing more reaction sites. The visible light absorption of CeO_2 – Octa is more than that of CeO_2 – HPC, which enhance the light yield. Both of the reasons impel the best activity in the all samples.

However, the activity of the CeO_2 – Octa is not satisfactory. We think that there are two aspects should be improved. Firstly, the visible light absorption should be improved. Secondly, the morphology of nanoparticles should be modified to obtained larger surface area.

Chapter 3 is focus on morphology control of cerium dioxide.

Chapter 3 Improvement of photocatalytic activity by morphology control of cerium dioxide

3.1 Introduction

Morphology has a great impact on the properties of nanomaterials, we will focus on the morphology controlled of CeO_2 nanomaterials in this chapter. Nano – Spindles, nano – flakes, nano – hollow structures of CeO_2 have been prepared via solvothermal and reflux methods. 1 – D and 2 – D materials are favor to the reaction between reactants and photogenerated holes or electrons and then inhibit the recombination of electron – hole pairs due to the sterically hindered. Nanomaterials with a hollow structure have attracted considerable interest in the past few decades due to their low density and high surface area. In this chapter, porous hollow spherical CeO_2 and hollow octahedral CeO_2 were prepared by solvothermal method. The activities of prepared CeO_2 were improved a lot due to their special morphologies.

3.2 Nano - Spindles

3.2.1 Experimental section

Materials

Diammonium cerium(IV) nitrate (Wako) Assay min 98.0%;

Ethanol (Wako) Assay min 99.5%;

Ethylene glycol (Wako) Assay min 99.5%;

Deionized water;

Polyvinylpyrrolidone K30 (Wako).

Synthesis process

Typically, 0.66 g of diammonium cerium (IV) nitrate was dissolved in 30 mL of ethylene glycol containing 0.53 g PVP under vigorous stirring until a homogeneous solution was obtained. The mixture was heated under reflux to

the boiling point of ethylene glycol (ca. 190°C) for 24 h. The color of the solution changed initially to yellowish brown and a brown gas was evolved during reflux. A white precipitate started to appear after about 2 h and the reaction mixture became milky. At the end of the predetermined reaction time, the mixture was centrifuged and washed with deionized water and absolute ethanol to remove excess ethylene glycol and PVP. After drying overnight in a vacuum oven at 80 °C, the product was calcined at 400 °C for 4 h for crystallization. All the samples will be reserved under black - UV illumination for photocatalytic evaluation.

Characterization

The crystal structure and composition were determined by XRD using a Rigaku MiniFlex II X-ray diffractometer with a Cu-Kα radiation source (γ = 1.5405Å). The morphologies of the samples were observed by FESEM (JEOL, JSM - 6701FONO) and TEM (Hitachi, H-9000NAR, 200 kV). HRTEM analysis was conducted using a Tecnai G2 F30 S-TWIN (300 kV). Diffuse reflectance (DR) spectra were measured using a UV - vis spectrophotometer (Shimadzu, UV - 2500PC) equipped with an integrating sphere unit (Shimadzu, ISR - 240A).

3.2.2 Results and discussion

FE - SEM and TEM

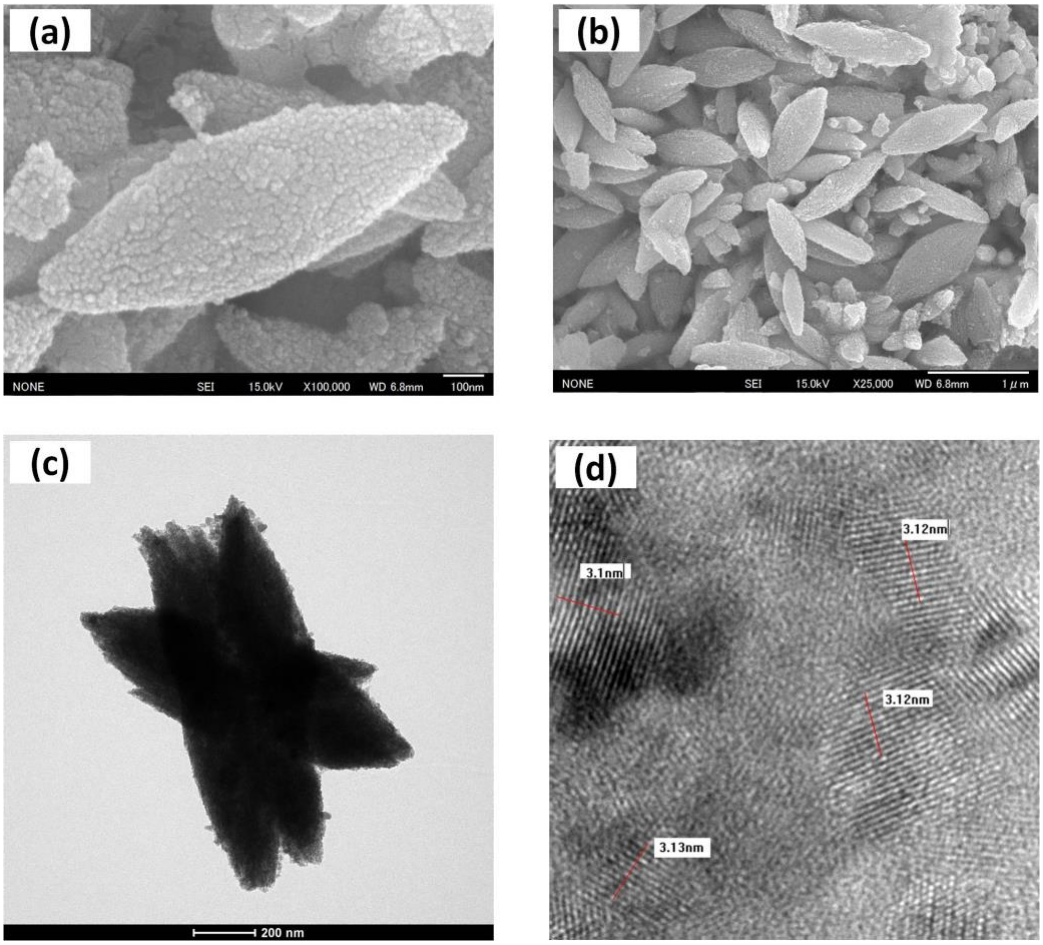

Figure 3.1. Morphology and crystal information of the CeO_2-spindle.

Morphology and crystal information of the CeO_2 - spindle were be characterized by FE – SEM and HRTEM technologies. Figure 3.1a & b are the SEM images of CeO_2 – spindle. The shape is almost like a spindle, and the aspect ratio of CeO_2 – spindle is 2.4 : 1. The aggregation was effectively suppressed due to the steric effect. In addition, the surface of CeO_2 – spindle is rough, which could supply more reactive sites. According to the TEM image (Figure 3.1c), we can confirm that it is a 3D spindle shape, not a 2D – like spindle. HRTEM (Figure 3.1d) shows the interplanar spacing is 0.31 nm indexing to (111) crystal facet.

XRD patterns

Figure 3.2. Crystal phase information of both CeO_2 - HPC and CeO_2 - spindle.

The phase purity of the prepared products was estimated by the XRD patterns. Figure 3.2 Shows the XRD patterns of CeO_2 – HPC and CeO_2 - spindle. All of the characteristic peaks were indexed to the face-centered cubic phase with space group Fm3m of ceria (JCPDS card no. 34-0394). No other sharpen peaks were detected, exception of the broad and flat peak around 20° ~ 25° in CeO_2 – spindle. It indicated that there some amorphous phase in CeO_2 – spindle, which could be observed in HRTEM image (Figure 3.1d). This amorphous phase will generate a positive or negative impact on its performance. The peaks

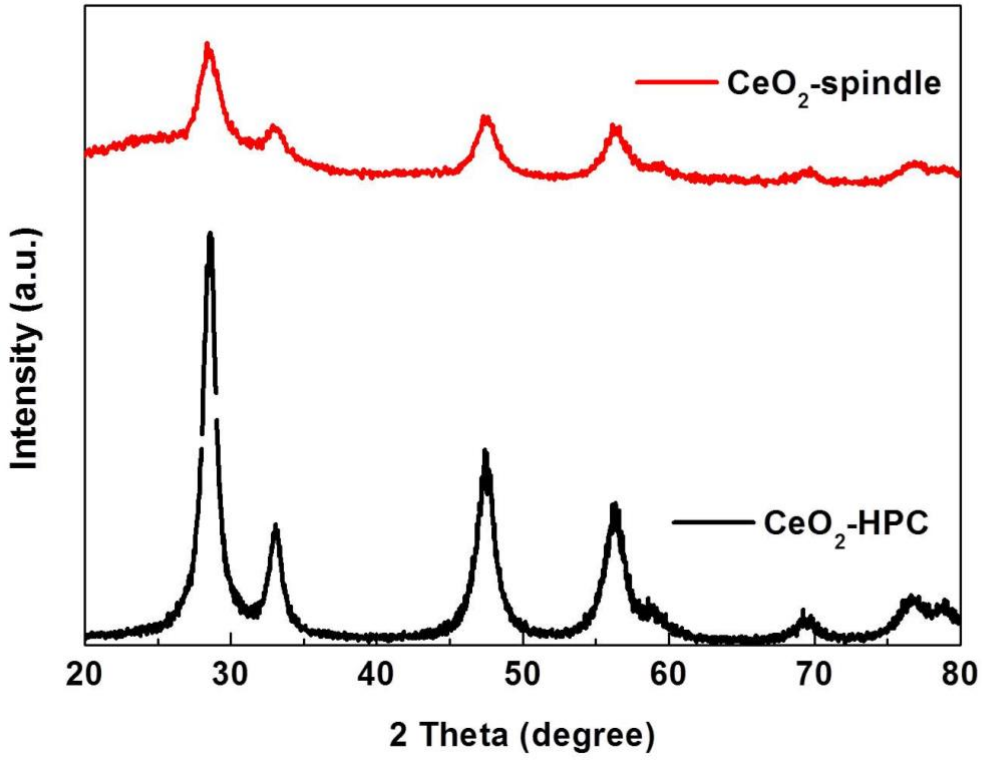

of CeO_2 - spindle was relatively broad, demonstrating that the CeO_2 - spindle was composed of smaller crystals. The average primary particle size was ca. 4.2 nm (Table 3.1), which is according to the calculation with the Debye–Scherrer formula for the strongest peak (111).

UV-vis spectra and band gap values

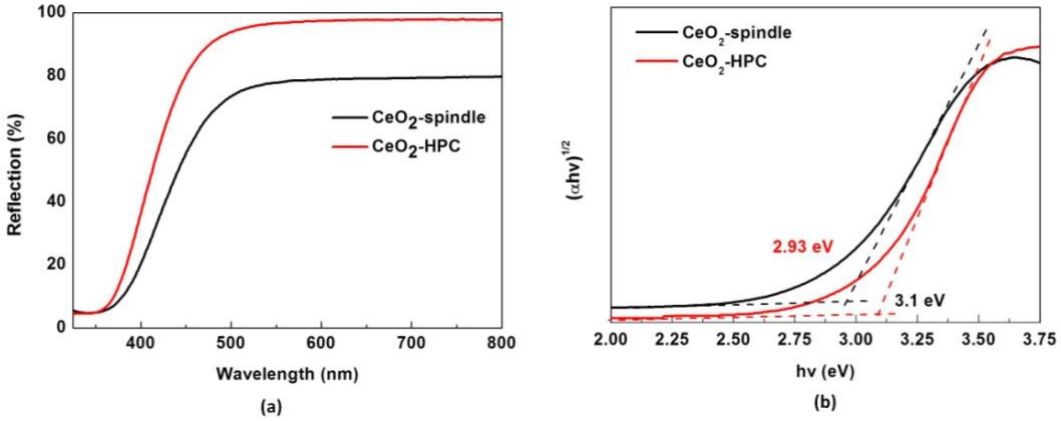

Figure 3.3. UV-vis spectra and KM transformed spectra of both CeO_2 - HPC and CeO_2 - spindle.

For ultraviolet-blocking materials, ceria has a strong absorption in the ultraviolet range. Optical information of all the samples will be shown in UV – vis spectra (Figure 3.3a). There is a strong absorption band from 300 nm to 350 nm in the spectra, which is assigned to the charge transfer from O^{2-} in O 2p to Ce^{4+} in Ce 4f. As semiconductor materials, the indirect band gap (Eg) can be calculated from the equation of $ahv = A (hv - Eg)^2$, where hv is the photon energy, a is the absorption coefficient, and A is a constant of CeO_2. Calculated Eg values for CeO_2 - HPC and CeO_2 – spindle were 3.1 eV and 2.93 eV, respectively (Figure 3.3b), which are smaller than the theoretical value of 3.2 eV for bulk CeO_2. Compared with CeO_2 – HPC, CeO_2 – spindle have a relative red shift. The possible reason is that The existence of quantum confinement effect due to the nanoscale size of the primary particles forming the CeO_2 – HPC. Also, the UV – vis spectra we can confirm the light absorption of both samples and then choose the suitable light source.

3.2.3 Conclusions

Here, a special spindle – like cerium dioxide materials have been prepared by a simple reflux method. It possesses rough surface and narrower band gap (more

visible light absorption), which is in favor to enhance the photocatalytic activity. However, the effect of amorphous phase on the photocatalytic activity should be investigated.

Table 3.1 Band gap results and calculated values from XRD patterns

Samples	Band gap/eV	Grain size/nm
CeO_2 - spindle	2.93	4.2
CeO_2 - HPC	3.1	8.7

3.3 Nano – flakes

3.3.1 Experimental section

Materials

Diammonium cerium(IV) nitrate (Wako) Assay min 98.0%;

Cerium (III) Nitrate Hexahydrate (Wako) Assay min 98.0%;

Ethanol (Wako) Assay min 99.5%;

Ethylene glycol (Wako) Assay min 99.5%;

Acetic acid (Wako) Assay min 99.5%;

Deionized water;

Hexamethylenetetramine (HMT);

Polyvinylpyrrolidone K30 (Wako).

Synthesis process

Reflux method. The method is similar to the preparation of Spindle-CeO_2. The 2-times amplification amount of precursor was added into the same Pyrex reactor (100 mL). The prepared product was marked as CeO_2-FR.

Solvothermal method. All chemicals were of analytical grade and used without further purification. In a typical synthesis procedure, 0.75 mmol cerium (III) nitrate hexahydrate was dissolved in 15 ml deionized water to form a transparent solution, then 5.25 mmol hexamethylenetetramine (HMT) and 0.6 ml acetic acid were added. The solution was stirred vigorously for 30 min and then poured into a Teflon-lined stainless steel autoclave. After being sealed, the vessel was placed into a thermostat oven at 140 °C for 9 h. After cooling down to room temperature naturally, the white powder was collected by centrifugation, washed with deionized water and anhydrous alcohol for three times to remove other ions and then dried at 60 °C in air for 12 h. The CeO_2 nano - flakes were obtained via annealing the precursor at 600 °C for 2 h. The prepared product was marked as CeO_2-FS.

All the samples will be reserved under black-UV illumination for photocatalytic evaluation.

Characterization

All the characterization technologies are same as that of CeO_2-spindle.

3.3.2 Results and discussion

FE – SEM and TEM

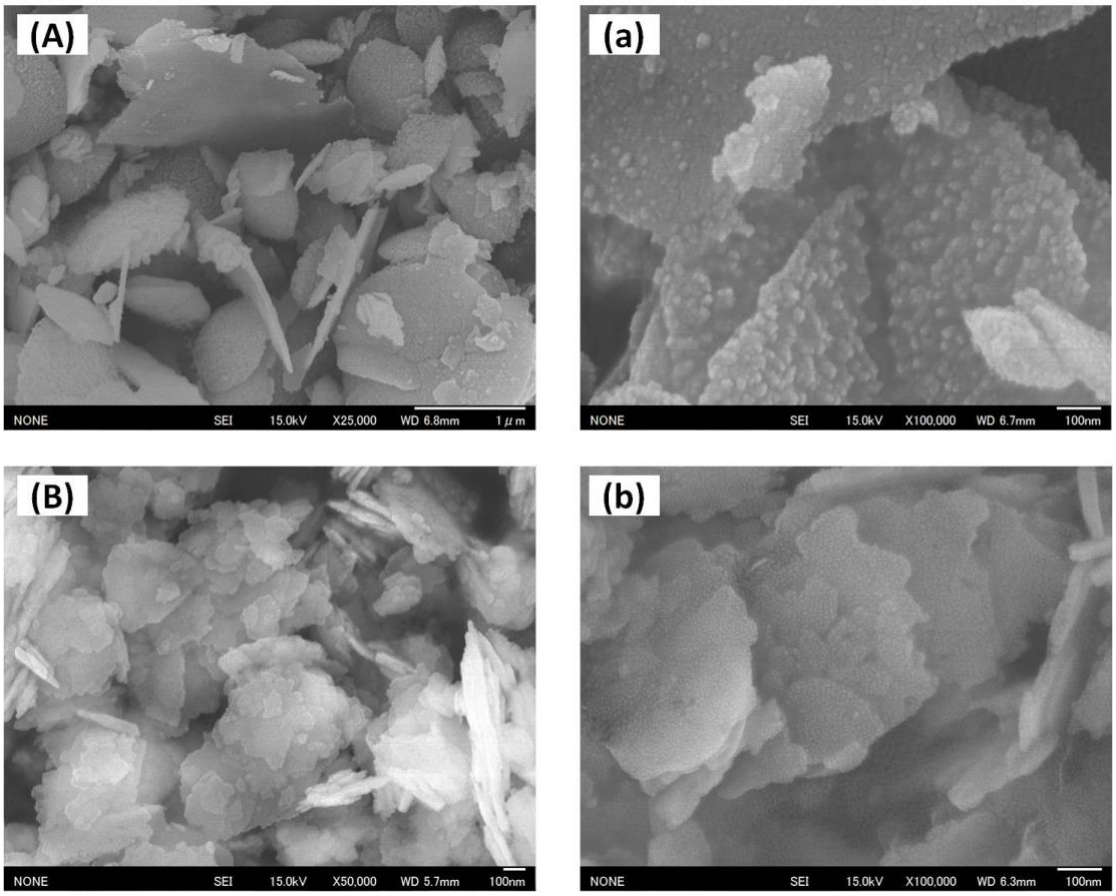

Figure 3.4. Morphology and crystal information of the two kinds of CeO_2. (A - a) CeO_2 - FR, (B - b) CeO_2 - FS.

Two-dimensional plane structure has attracted a lot of attentions due to its high surface are and special charge limitation effect. Here, we prepared the two-dimensional nano - flake cerium dioxide materials via two methods. Figure

3.4A ~ a are the prepared nano – flake cerium dioxide by reflux method. CeO_2 – FR is very special due to the different sharp of the two sides. One side is very smooth and other side is greatly rough, which will have a great effect on its performance. In case of CeO_2 – FS (Figure 3.4B ~ b), it is prepared via a simple solvothermal method. It is also a nano – flake morphology, while the area of the two-dimensional plane is smaller than that of CeO_2 – FR. In addition, we can find that CeO_2 – FS is composed with smaller flakes.

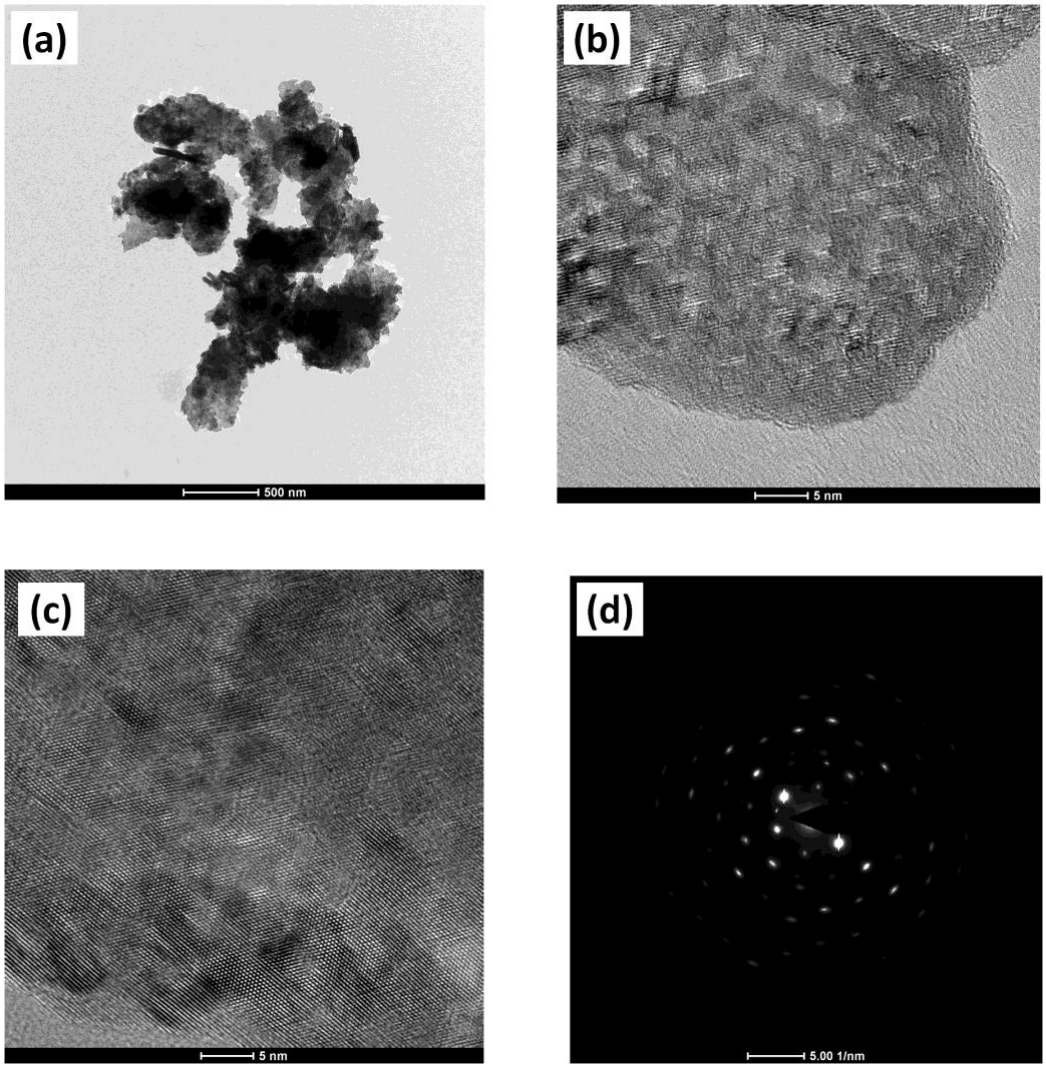

Figure 3.5. TEM, HRTEM and SAED information of CeO_2 - FS.

In order to further observe the morphology of CeO_2 – FS, TEM technology has been conducted. In high resolution, uneven surface of CeO_2 – FS can be

clearly observed. However, the crystallinity is excellent according to the results of HRTEM and SAED (Figure 2.5c ~ d).

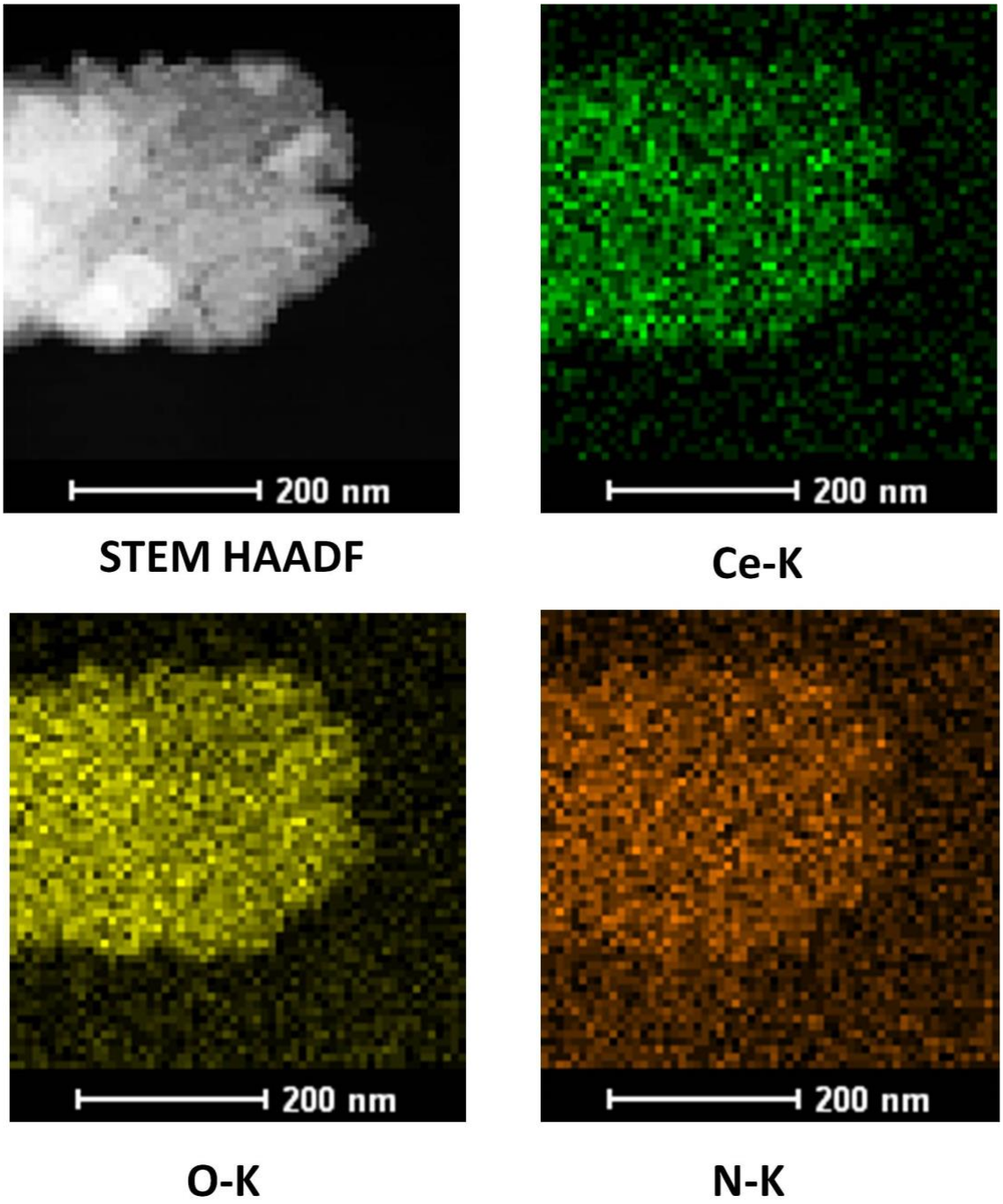

Figure 3.6. Element mapping information of CeO_2 - FS.

Element mapping results show that cerium and oxygen elements are evenly distributed over the entire nano – flakes. However, additional element

(nitrogen) is observed, which should be originated from the surfactant (Hexamethylenetetramine).

XRD patterns

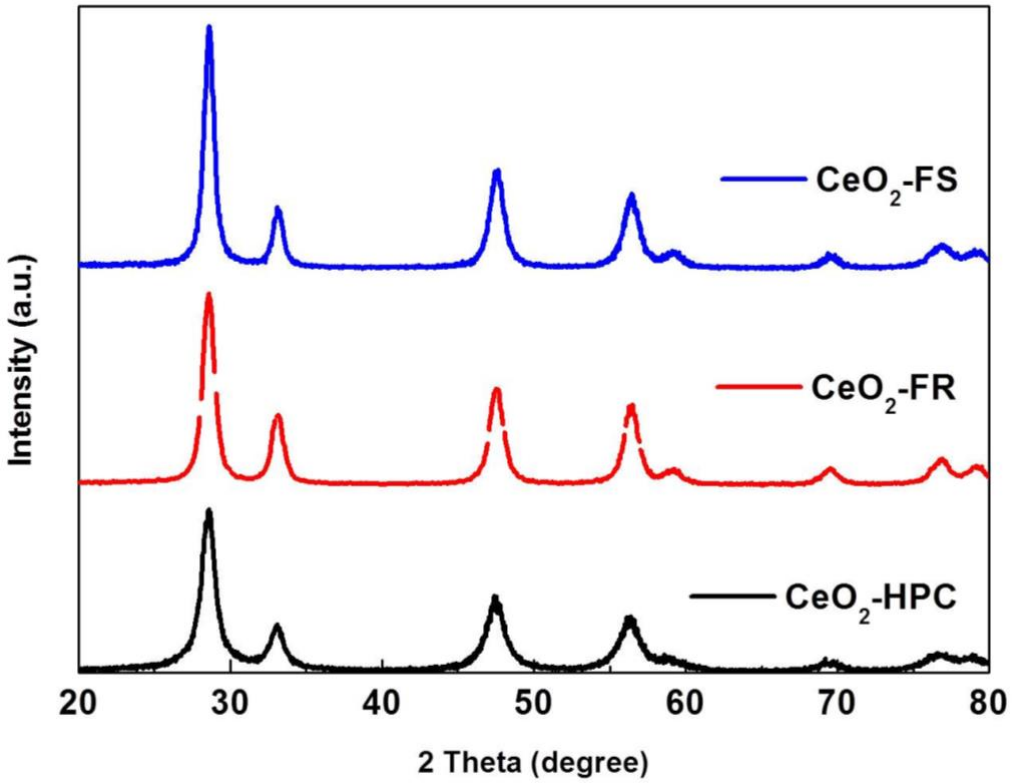

Figure 3.7. XRD patterns of CeO_2 - HPC, CeO_2-FR and CeO_2 - FS.

The phase purity of the prepared products was estimated by the XRD patterns. Figure 3.7 Shows the XRD patterns of CeO_2 – HPC, CeO_2 - FR and CeO_2 - FS. All of the characteristic peaks were indexed to the face-centered cubic phase with space group Fm3m of ceria (JCPDS card no. 34-0394). No other sharpen peaks were detected, indicating their pure crystal. The average primary particle size (grain size) of CeO_2 – HPC, CeO_2 - FR and CeO_2 - FS. are ca. 8.9 nm, 9.3nm and 11 nm. (Table 3.2), which are according to the calculation with the Debye–Scherrer formula for the strongest peak (111).

UV-vis spectra and band gap values

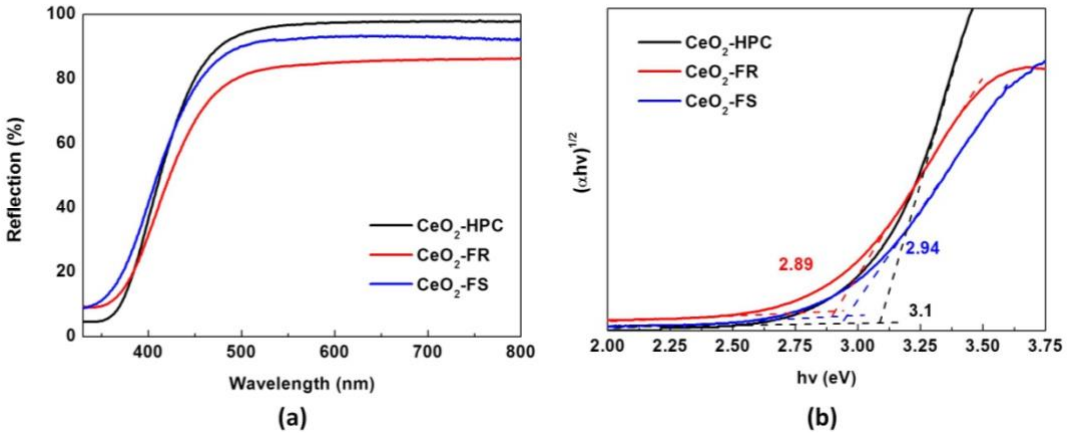

Figure 3.8. UV-vis spectra and KM transformed spectra of CeO_2 - HPC, CeO_2 - FR and CeO_2 - FS.

Optical information of all the samples will be shown in UV – vis spectra (Figure 3.8a). There is a strong absorption band from 300 nm to 350 nm in the spectra, which is assigned to the charge transfer from o^{2-} in O 2p to Ce^{4+} in Ce 4f. As semiconductor materials, the indirect band gap (Eg) can be calculated from the equation of $ahv = A (hv - Eg)^2$, where hv is the photon energy, a is the absorption coefficient, and A is a constant of CeO_2. Calculated Eg values for CeO_2 – HPC, CeO_2 – FR and CeO_2 – FS were 3.1 eV, 2.94 eV and 2.89 eV, respectively (Figure 3.8b), which are smaller than the theoretical value of 3.2 eV for bulk CeO_2. Compared with CeO_2 – HPC, CeO_2 – FR and CeO_2 – FS have a relative red shift. The possible reason is that The existence of quantum confinement effect due to the nanoscale size of the primary particles forming the CeO_2 – HPC. Also, the UV – vis spectra we can confirm the light absorption of both samples and then choose the suitable light source.

3.3.3 Conclusions

In section, two kinds of nano – flake cerium dioxide materials have been prepared by reflux and solvothermal methods. Both kind of nano – flakes show

the thin layers and excellent dispersibility. CeO_2 – FR even shows the different properties of two sides, which is a very absorbing discovery. However, the exist of nitrogen may be effect the performance of CeO_2 – FS. We should remove the nitrogen from hexamethylenetetramine by increase the duration of calcined treatment.

Table 3.2 Band gap results and calculated values from XRD patterns

Samples	Band gap/eV	Grain size/nm
CeO_2 - FR	2.94	9.3
CeO_2 - FS	2.89	11

3.4 Hollow nano – octahedrons

3.4.1 Experimental section

Materials

Cerium (III) Nitrate Hexahydrate (Wako) Assay min 98.0%;

Ethanol (Wako) Assay min 99.5%;

Deionized water;

Air, CO_2, and Argon (Q – SAN);

Polyvinylpyrrolidone K30 (Wako).

Synthesis process

All chemicals used in the experimental section were analytical grade and used as received without further purification. Typically, 1.0 g of Cerium(III) nitrate hexahydrate and 0.10 g of PVP were dissolved in a mixture of C_2H_5OH (40 mL) and H_2O (40 mL) with magnetic stirring for 30 min. Consecutively, fully mixed solution will be bubbled with Ar, O_2, and CO_2 for 30 min. Then the suspension was transferred to a 100-mL Teflon-lined autoclave and heated at 180 °C for 24 h. After cooling to room temperature, the product was collected by centrifugation, washed with ethyl alcohol and water until the ionic strength was less than 5 μs/cm, and dried at 70 °C overnight. Finally, we obtained various CeO_2, and reserved them under black-UV illumination.

Characterization

The crystalline phase of various CeO_2 were characterized by using a powder X-ray diffraction (XRD) instrument (MiniFlex II, Rigaku Co.) with Cu Kα (λ = 1.5418 Å) radiation (cathode voltage: 30 kV, current: 15 mA). The morphologies of the samples were observed by FESEM (JEOL, JSM-6701FONO) and TEM (Hitachi, H-9000NAR, 200 kV). An absorption spectrum was acquired at room temperature with a UV–vis spectrometer (UV-2600, Shimadzu Co.). An XPS experiment was carried on a Thermo ESCALAB 250Xi

system at room temperature under Al Kα using monochromatic radiation and C1s peak (284.70 ± 0.1 eV) reference.

Evaluation of activity

Photocatalytic activity of the samples was evaluated by photocatalytic decomposition of isopropyl alcohol to acetone in gas phase. Samples powder (150 mg), which had completed extinction of incident radiation, was spread on a glass dish, and the glass dish was put into a Tedlar bag (AS ONE Co. Ltd.) with a volume of 125 mL mixed air (79% N_2, 21% O_2, <0.1 ppm of CO_2, 500 ppm of 2-propanol). After 3-h adsorption equilibrium in the dark, the photocatalysts were exposed under the LED 365 nm. The light intensity was fixed to 1 mW/cm^2. In the photocatalysis process, generation of acetone and consumption of 2-propanol were monitored by online gas chromatography (Agilent Technologies, 3000A Micro-GC, TCD detector) equipped with OV1 and PLOT-Q columns.

3.4.2 Results and discussion

FE – SEM and TEM

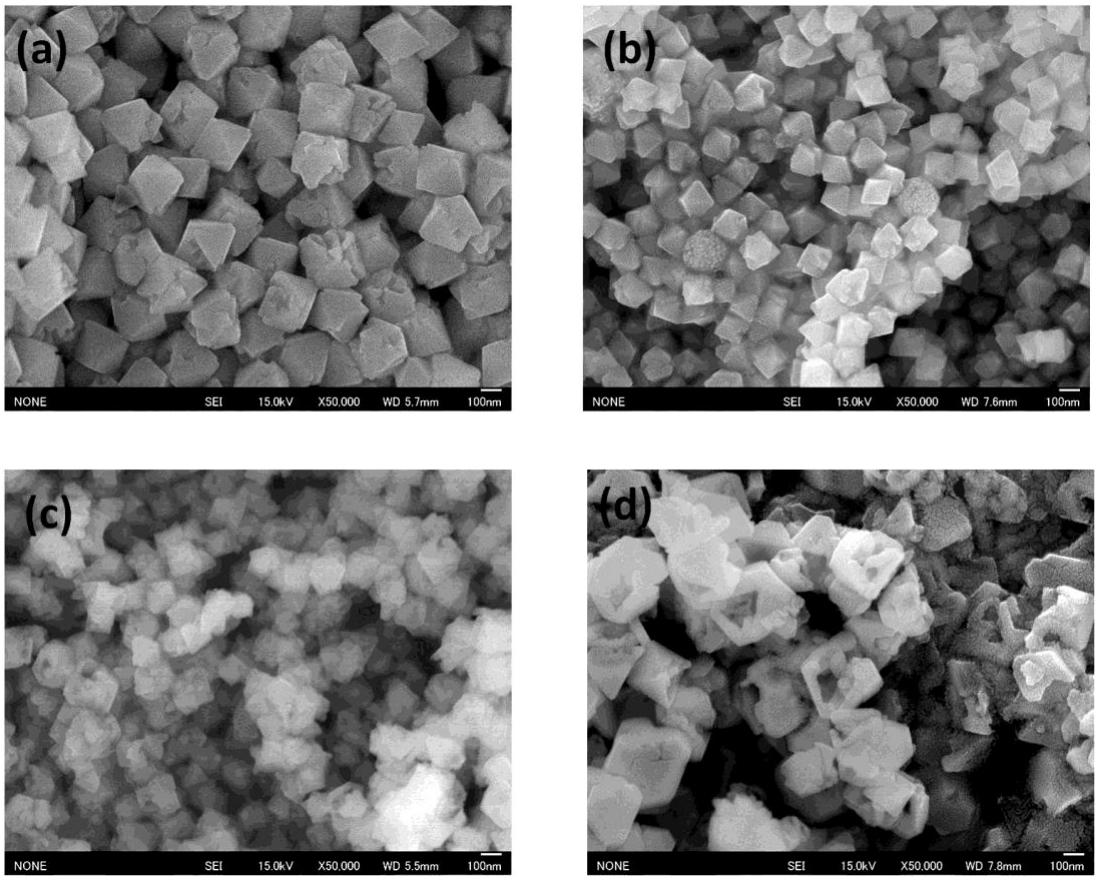

Figure 3.9. FE – SEM images of all the samples. (a) CeO_2 – normal, (b) CeO_2 – Ar, (c) CeO_2 – O_2, (d) CeO_2 – CO_2.

Morphologies and surface structure information have been characterized by FE-SEM technology. Figure 3.9 (a) ~ (d) show the FE-SEM images of as-prepared samples. Compare with CeO_2 - normal, the structures of CeO_2 - O_2 and CeO_2 - CO_2 generated different degrees of distortion. Hollow structure even was observed in CeO_2 - CO_2 sample, which could provide more active sites for photocatalytic process and improve the activity. On the contrary, the CeO_2 - Ar maintained a complete octahedron structure, which could be contributed to moderate hydrothermal process due to the protection of the inert atmosphere.

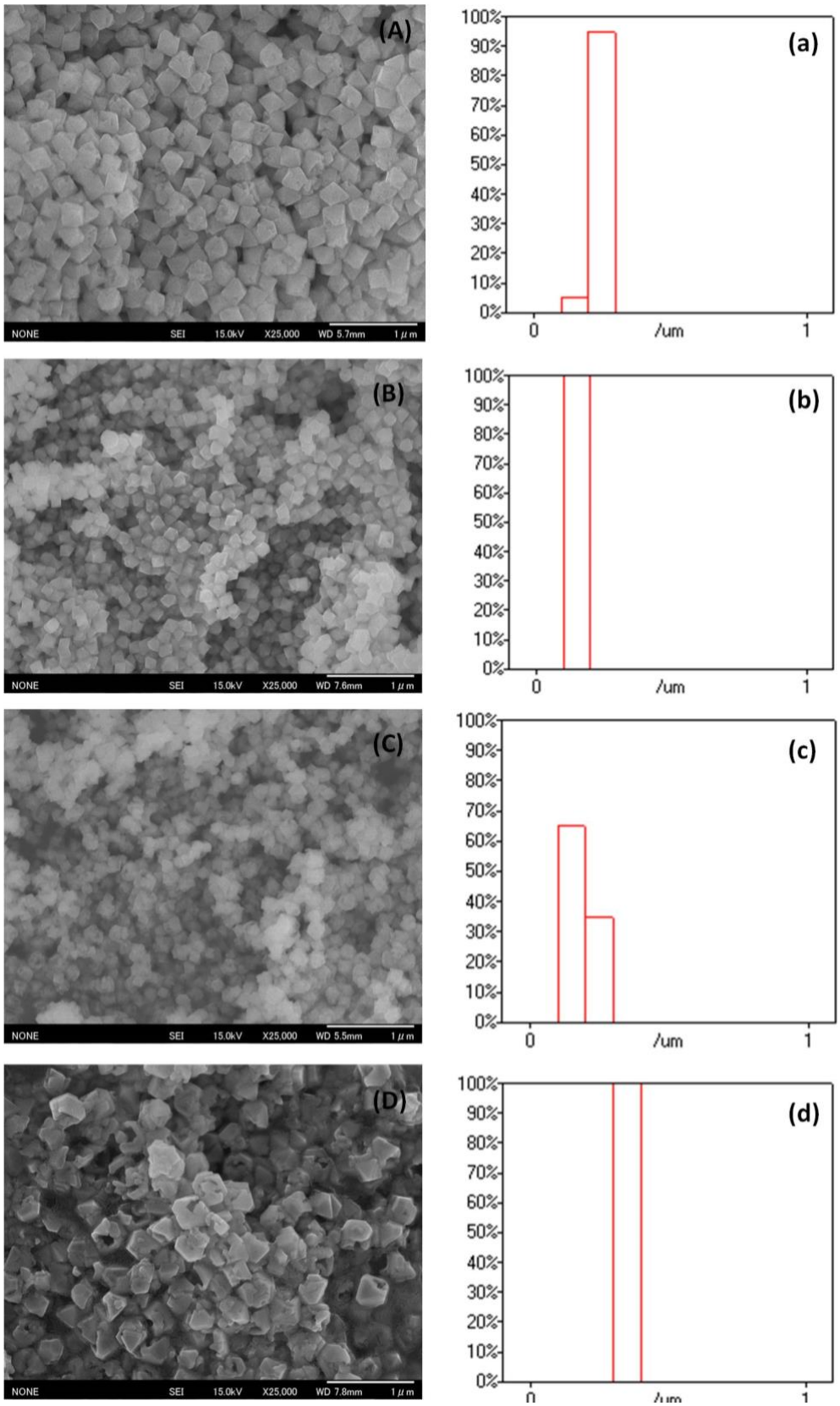

Figure 3.10. Low magnification SEM images and diameter distribution histograms of (A) - (a) CeO_2 - normal, (B) - (b) CeO_2 - Ar, (C) - (c) CeO_2 - O_2, (D) - (d) CeO_2 - CO_2.

In addition, the size distributions were tested via statistical results in Figure 3.10, indicating a significant change. Samples of CeO_2 - normal, CeO_2 - Ar, and CeO_2 - CO_2 were monodisperse, and the mean size were 220 nm, 150 nm, and 350 nm, respectively. Meanwhile, CeO_2 - O_2 owned two range of size distributions, 170 nm (complete octahedron) and 250 nm (partially hollow structure). CeO_2 - O_2 could be considered as a "transition state" between CeO_2 - normal and CeO_2 - CO_2.

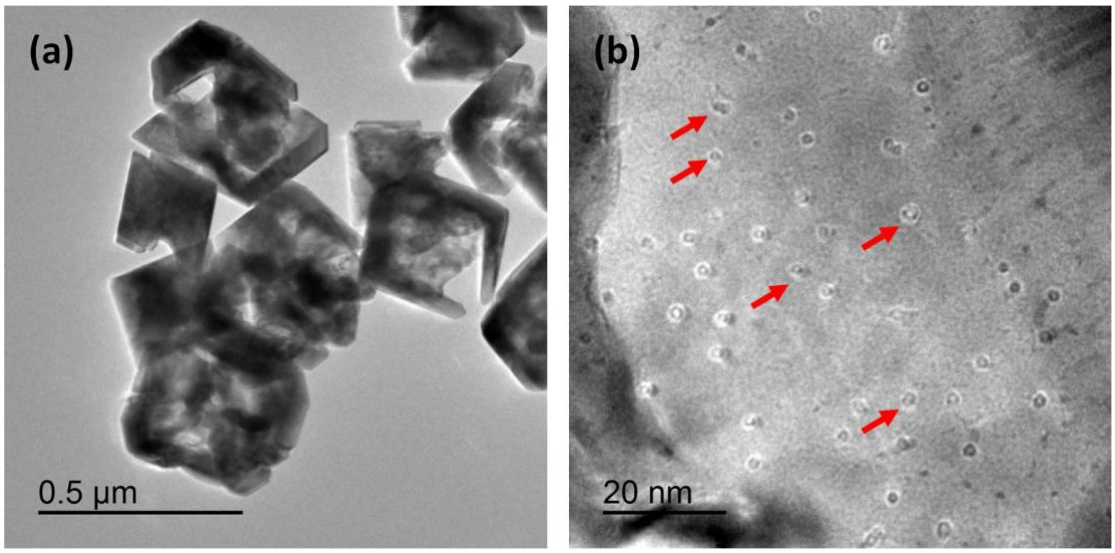

Figure 3.11. amplified TEM image of the surface structure from CeO_2 - CO_2.

In order to further observe the hollow structure in CeO_2 - CO_2, TEM characterization has been conducted. The hollow structure could be confirmed by light and dark contrast in Figure 3.11. Complete octahedral, distorted and damaged nanoparticles with hollow structure could be observed, which was attributed to the effect of the CO_2 atmosphere. According to the Laurence Vivier's research results, CeO_2 exhibits the highest number of surface basic sites among some selected metal oxides, indicating that CeO_2 is advantageous regarding acid gas capture. CO_2 as an acid gas could be quickly absorbed on the surface and inside, and then played a crucial role in hollow structure formation process. Figure 3.11a shows amplified TEM image of surface

information in Figure 3.11b Many little voids were appeared on the surface, which could be as the mass exchange channels for hollow structure formation.

Formation schemes

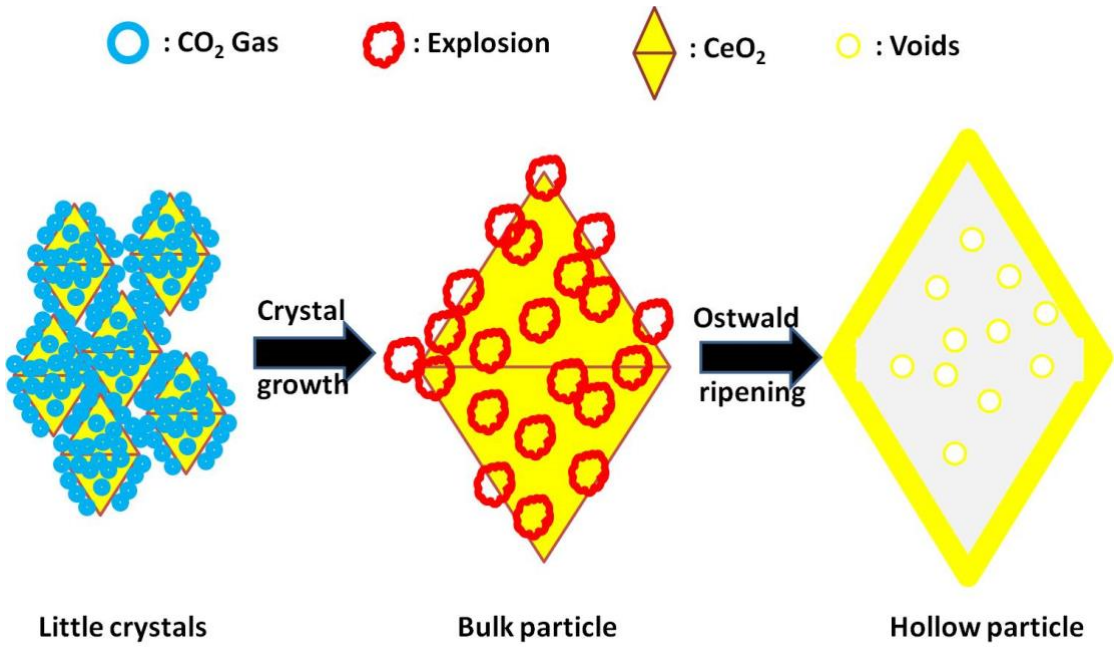

Scheme 3.1. Feasible mechanism hollow structure formation in CeO_2 - CO_2.

Based on the above results, a feasible mechanism could be speculated (Scheme 3.1). Firstly, amount of CO_2 absorbed on the basic sites of CeO_2 in the hydrothermal process. When the accumulation of CO_2 in basic sites approached critical point, generated CO_2 bubbles would explode and form the void channels. Continuously, Ostwald ripening process got underway. As the time going, the hollow structure formed.

XRD patterns

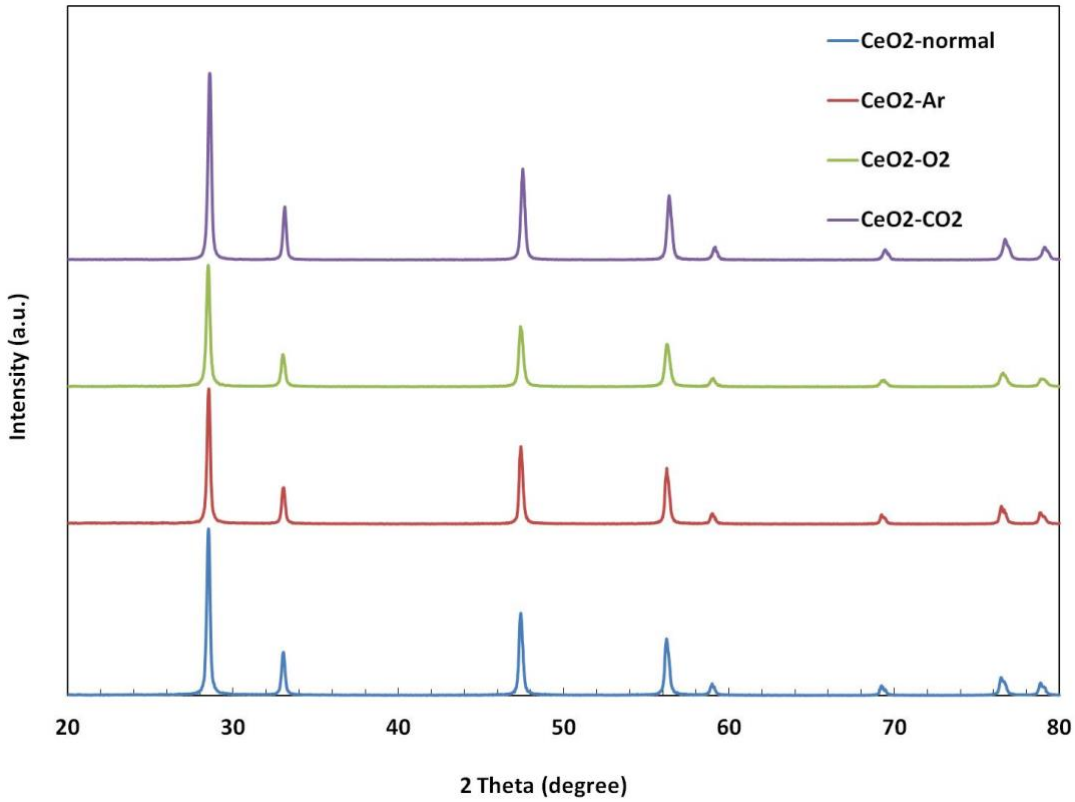

Figure 3.12. XRD patterns of all the samples.

Although the atmosphere generates a significant effect on the morphologies of all the samples, it does not change the composition and phase of CeO_2. As shown in Figure 3.12, all of the characteristic peaks were indexed to the face-centered cubic phase with space group *Fm3m* of ceria (JCPDS card no. 34-0394) . No other peaks were detected, and the sharp peaks indicated that the high purity and the highly crystalline nature of both samples.

XPS spectra

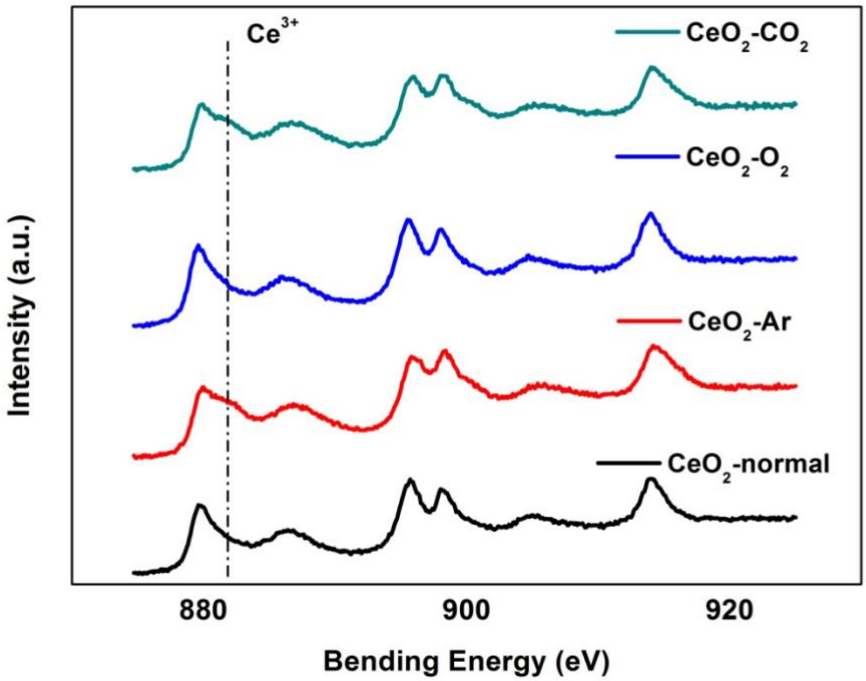

Figure 3.13. XPS spectra of all the samples.

XPS analysis was carried out to obtained the more detail the surface composition and chemical state in Figure 3.13. The CeO_2 spectrum is composed of two multiplets (v and u), which correspond to the spin–orbit split $3d_{5/2}$ and $3d_{3/2}$ core holes. Here, we briefly estimated the Ce^{3+} content of each sample based on the characteristic peak (881.1 eV), CeO_2 - Ar > CeO_2 - CO_2 > CeO_2 - normal > CeO_2 - O_2. Ce^{3+} is generated from the reducing process of CeO_2 by ethanol, while oxygen will transfer Ce^{4+} to Ce^{3+}, CeO_2 - O_2 has the lowest content of Ce^{3+}. Moderate amount of Ce^{3+} will improve the photocatalytic activity because Ce^{3+} can generate oxygen vacancies and provide active sites for reactants. However, exceed Ce^{3+} will become the recombination center and then depress the activity.

UV-vis spectra and band gap values

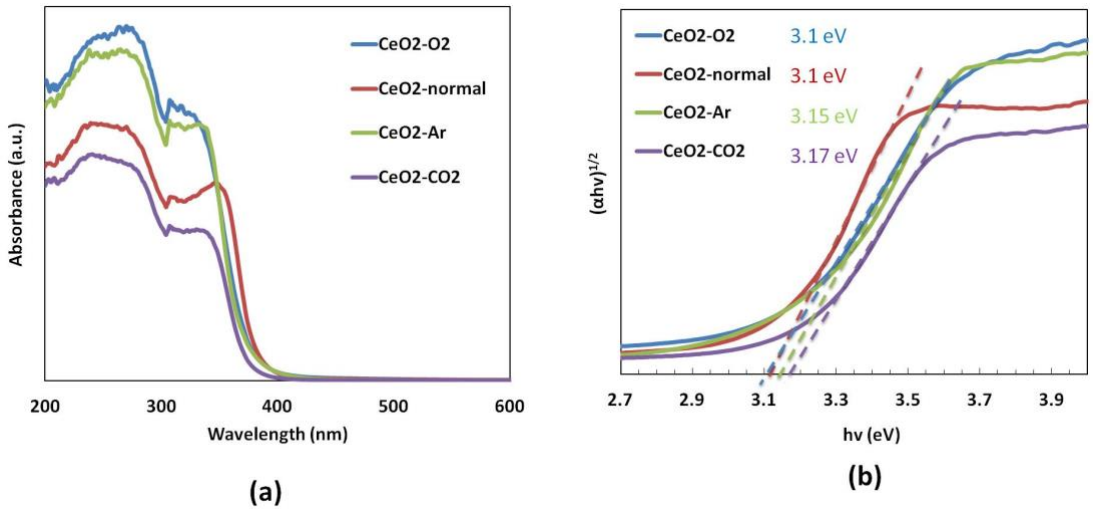

Figure 3.14. UV-vis spectra and KM transformed spectra of all the samples.

Figure 3.14a shows UV-vis diffuse reflectance spectra of all the samples. There is a strong absorption band from 200 nm to 400 nm in the spectra, which is assigned to the charge transfer from O^{2-} in O 2p to Ce^{4+} in Ce 4f. As a result, LED 365 lamp was chosen as the light source for photocatalytic evaluation. The plots (Figure 3.14b) with steep edges of the transformed Kubelka–Munk function versus light energy show the band gap of all the sample. The values (CeO_2 - normal: 3.1 eV, CeO_2 - Ar: 3.15 eV, CeO_2 - O_2: 3.1 eV, CeO_2 - CO_2: 3.17 eV) are pretty approaching, ensuring that all the sample can be excited by the light resource and conduct the photocatalytic process.

Photocatalytic activities

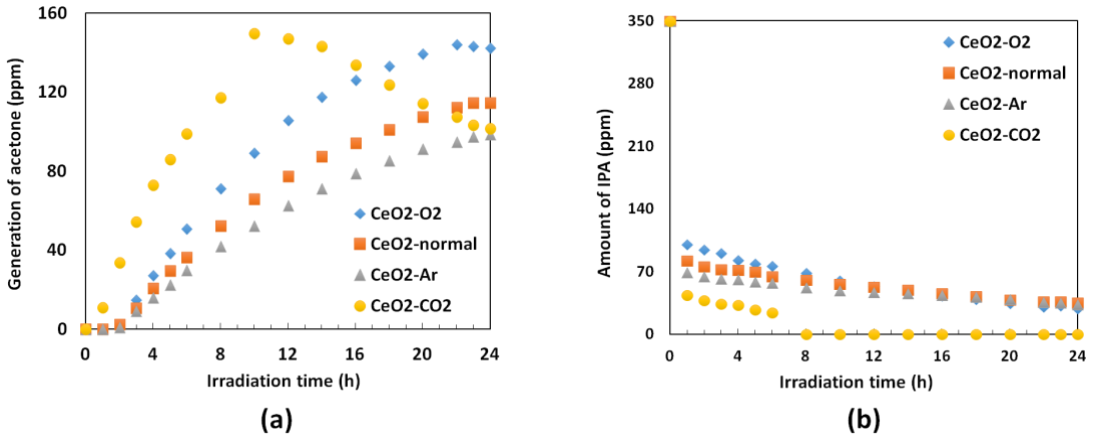

Figure 3.15. Photocatalytic activities of all the samples.

Photocatalytic activity was evaluated by the decomposition of isopropanol to acetone under LED 365 nm irradiation. Figure 3.15a shows activities of all the samples, and it is consistent with the anticipation that CeO_2 - CO_2 possesses the highest activity. CeO_2 - CO_2 not only obtained the highest conversion but also exhibited the fastest reaction speed. Conversion of other three samples was ignited at the third hour, but CeO_2 - CO_2 started for the first time. This excellent activity could be ascribed to the hollow structure that CeO_2 - CO_2 could absorb more reactants before irradiation (Figure 3.15b) and provide more active sites in the process. In addition, a moderate amount of Ce^{3+} also was a factor for high activity as mentioned above. CeO_2 - CO_2 with eighth irradiation, the amount of IPA gradually decreased due to saturation of acetone, and then decomposed to CO_2. The activity curve of CeO_2 - O_2 was approaching a platform after 22 h reaction, indicating that the amount of acetone was reaching the critical value. However, the photocatalytic processes of CeO_2 - normal and CeO_2 - Ar almost stagnated after the 22 h reaction, indicating that the photocatalysts were deactivated. All of the results reveal that atmosphere in the hydrothermal process has a great effect on the photocatalytic activity of CeO_2.

3.4.3 Conclusions

In summary, we present a facile hydrothermal approach to adjust the morphologies and photocatalytic performances of CeO_2 through a gas bubbling with O_2, Ar, and CO_2. This article investigates the atmosphere effect on the hydrothermal, showing that CO_2 atmosphere is in favor of hollow structure formation and improve the activity. In addition, the moderate content of Ce^{3+} also is important for photocatalytic activity. Because of that CeO_2 materials own substantial basic sites, CO_2 (acid gas) can match with it and then obtain the excellent performance. Most important of all is that we should choose the matching atmosphere with target product, only in this way can the product of excellent properties be obtained.

3.5 Porous hollow nano - spheres

3.5.1 Experimental section

Materials

Cerium (III) Nitrate Hexahydrate (Wako) Assay min 98.0%;

Ethanol (Wako) Assay min 99.5%;

Ethylene glycol (Wako);

Polyvinylpyrrolidone K30 (Wako) ;

Acetaldehyde (SIGMA-ALDRICH) ACS reagent Assay min 99.5%;

Pure air (Taiyo Nippon Sanso) CO_2 < 0.1 ppm;

Deionized water.

Synthesis process

CeO_2 hollow spheres with ca. 140 nm in diameters were synthesized by a simple one-step template-free solvothermal method with reaction in a mixed solution of water, ethanol and glycol together with PVP (polyvinyl pyrrolidone) as a surfactant. Typically, 1.0 g of cerium(III) nitrate hexahydrate and 0.10 g of PVP were dissolved in a mixture of EG (20 mL), C_2H_5OH (40 mL) and H_2O (20 mL) with magnetic stirring for 3 h. Then the suspension was transferred to a 100-mL Teflon-lined autoclave and heated at 180 °C for 24 h. After cooling to room temperature, the product was collected by centrifugation, washed with ethyl alcohol and water until the ionic strength was less than 10 μs/cm, and dried at 70 °C overnight. Finally, we obtained hollow-sphere cerium dioxide, which is denoted as CeO_2 - PH. For control experiments, ceria nanoparticles were obtained under same conditions as those described above but in the absence of glycol, and the nanoparticles are denoted as CeO_2 - NP. All the samples will be reserved under black - UV illumination for photocatalytic evaluation.

Characterization

The CeO_2 materials were characterized using X-ray diffraction (XRD), X-ray photoelectron spectroscopy (XPS), field emission scanning electron microscopy (FESEM), transmission electron microscopy (TEM), high-resolution (HRTEM), ultraviolet-visible absorption spectroscopy (UV - vis), Brunauer-Emmett-Teller (BET) surface area analysis and Raman spectra.

The crystal structure and composition were determined by XRD using a Rigaku MiniFlex II X-ray diffractometer with a Cu-Kα radiation source (γ = 1.5405Å). The morphologies of the samples were observed by FESEM (JEOL, JSM - 6701FONO) and TEM (Hitachi, H-9000NAR, 200 kV). HRTEM analysis was conducted using a Tecnai G2 F30 S-TWIN (300 kV). Nitrogen adsorption/desorption measurements were performed at 77 K using a Quantachrome Nova 4200e to calculate the specific surface area using the BET model. The pore size distribution was obtained from desorption-isotherm curves by the Barrett Joyner Halenda (BJH) method. Prior to measurements, the samples were degassed in vacuum at 180 ^{0}C for 3 h. Diffuse reflectance (DR) spectra were measured using a UV–vis spectrophotometer (Shimadzu, UV - 2500PC) equipped with an integrating sphere unit (Shimadzu, ISR - 240A). Raman spectra were obtained by a laser Raman spectrum (JASCO, NRS - 5100). An XPS experiment was carried on a Thermo ESCALAB 250Xi system at room temperature under Al Kα using monochromatic radiation and C1s peak (284.70 ± 0.1 eV) reference. The background of XPS spectra was subtracted by the Shirley procedure and the peaks were fitted using the Gaussian-Lorentzian function.

Evaluation of activity

The method for the activity evaluation is same as that of chapter 1.

Photocurrent response experiment

The steps of photoelectrochemical test are shown in Scheme 3.2. The prepared samples (0.03g) were dissolved into the acetone for 1h ultrasonic, and then added a grain of iodine for 30 min ultrasonic. The samples were electroplated on the surface of the ITO glass with an area of 6 cm^2. The Plating voltage is 15 V, and the time of duration is 10 min. Photoelectrochemical measurements were performed with a homemade photoelectrochemical system. A 500 W Xe lamp was used as the irradiation source. Photocurrent was measured on an ALS 604D electrochemical workstation. Photocurrent response measurements were conducted in 1.0 M Na_2SO_4 solution in a three-electrode system. Indium tin oxide (ITO) electrode with ceria was employed as the working electrode. A coiled Pt wire was used as the counter-electrode and a saturated Ag/AgCl as the reference electrode. The interval of light-on and light-off is 4 s.

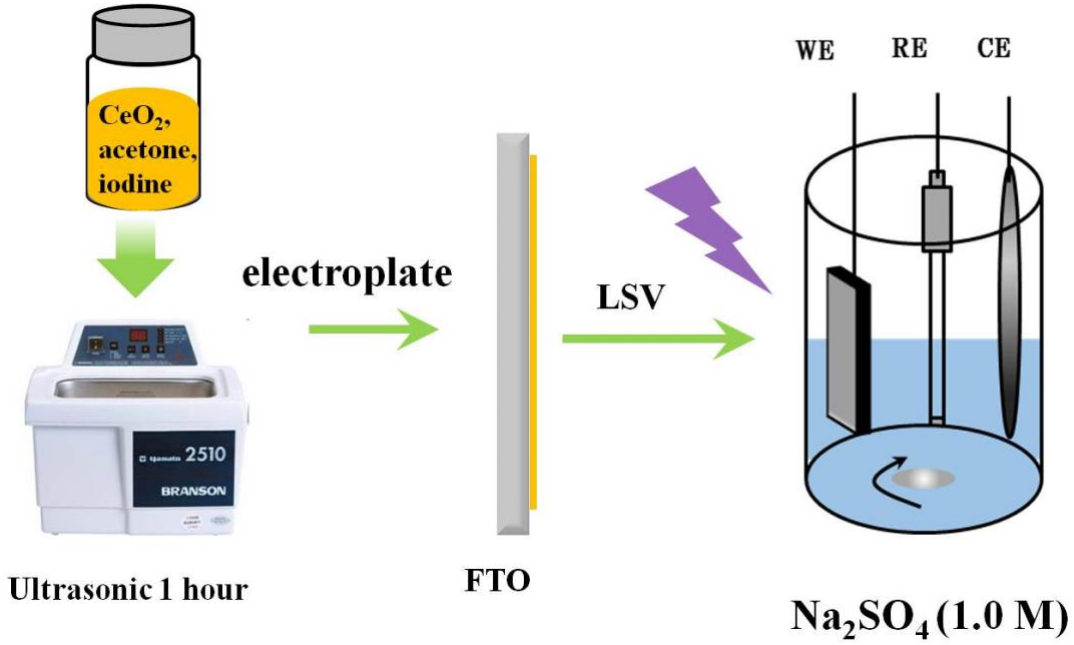

Scheme 3.2 Steps of photoelectrochemical test.

3.5.2 Results and discussion

FE – SEM and TEM

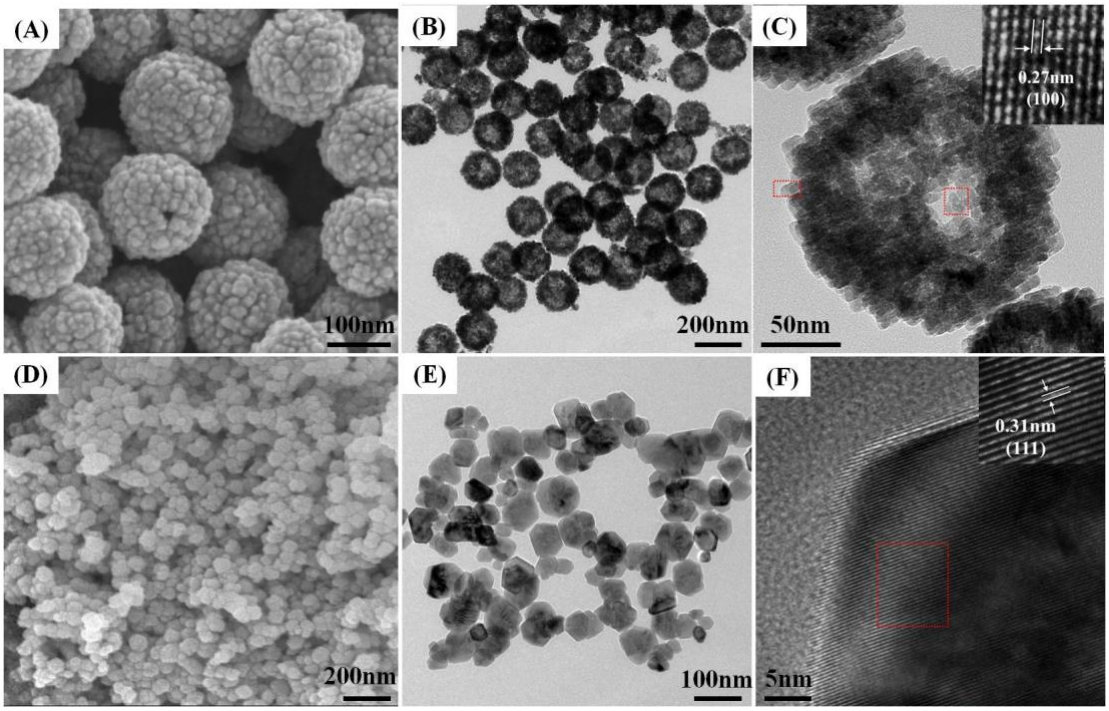

Figure 3.16. SEM images of (A) the CeO_2 hollow spheres, (D) the CeO_2 nanoparticles; TEM images of (B) & (C) the CeO_2 hollow spheres, (E) & (F) the CeO_2 nanoparticles, the inset is the HRTEM images.

The morphologies of the as-prepared CeO_2 photocatalysts were shown in Figure 3.16. Figure 3.16A shown an SEM image of ceria hollow spheres, which were composed of small nanoparticles. The diameter of the ceria hollow spheres was *ca.* 160 nm, and the particle size of the small nanoparticles was *ca.* 10 nm, which was in accordance with the XRD calculation. The voids that can be seen in Figure 3.16A suggested that the obtained ceria are porous - hollow spheres. TEM and HRTEM were performed to obtain more information about the special morphology. The low TEM image in Figure 3.16B clearly shown a hollow structure of the prepared sample. It had a narrow size distribution and the diameter was in accordance with the SEM observation. In the amplified TEM image shown in Figure 3.16C the contrast between the dark margins and

the pale center confirmed the existence of a hollow structure. Moreover, it revealed that the hollow ceria spheres consisted of small nanoparticles with a porous structure. This special morphology with a high specific surface area would be favorable for a photocatalysis process due to the full access of reactants (acetaldehyde in this study). The structure of the as-obtained ceria porous-hollow sphere nanocrystals was investigated in more detail by HRTEM (Figure 3.16C *inset*). The spacing of the measured 2D lattice fringes was close to 0.27 nm indexed to the interplanar spacing of the (100) plane of the outside and inside surfaces. Figure 3.16D ~ F show SEM, TEM, and HRTEM images of the ceria nanoparticles, which was set as the contrast samples. The sizes of nanoparticles were about 50 nm ~ 100 nm, and slight agglomeration can be seen in the SEM image in Figure 3.16D of the SEM image. Compared to previously prepared ceria, these ceria nanoparticles had better crystallinity as shown in the HRTEM image in Figure 3.16F though the dispersibility was not so good due to the absence of glycol. Glycol possesses a capping reagent function, and it also has a possibility of dissolution of the metal salt. The lattice fringe in the HRTEM image (Figure 3.16F inset) show a spacing of 0.31 nm from the (111) plane of the cubic ceria.

Formation schemes

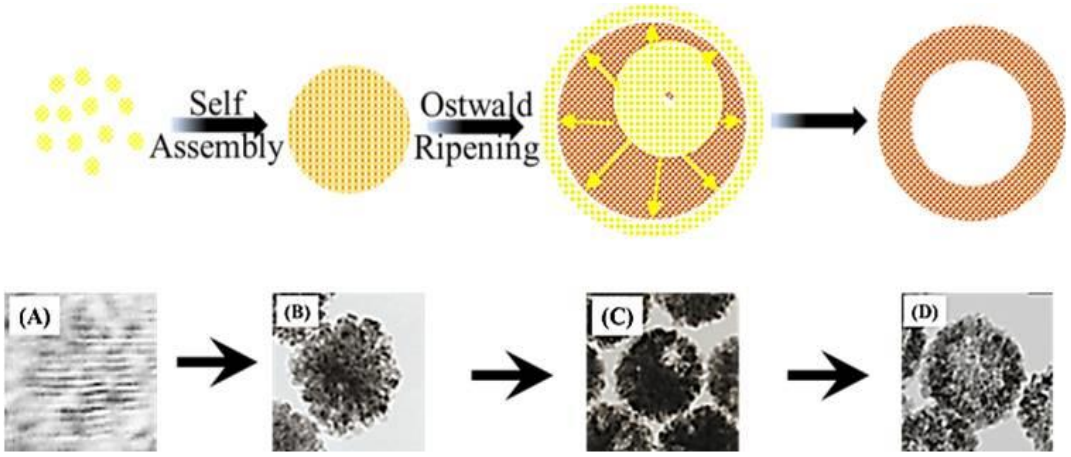

Scheme 3.3. Formation of the porous-hollow structure.

To understand the formation mechanism of the porous-hollow structure, samples synthesized with different reaction times were collected and analyzed. A plausible formation scheme of the hollow CeO_2 sphere is illustrated in Scheme 3.3. When PVP and $Ce(NO_3)_3{\cdot}6H_2O$ are dissolved in an aqueous ethanol and EG solution resulting in a homogeneous mixture, cerium ions are well surrounded by PVP molecules due to the strong interaction between the nuclei and surfactant. Nanoparticles followed by self-assembling of ceria nanoparticles to form a sphere shape because of the isotropic growth. The hollow shape is formed because cerium nanoparticles tend to move towards the wall of the sphere due to the density variation among nanoparticles and then undergo the Ostwald ripening process. Due to the difference of surface energy and particles located in the inner space of the spheres and this particles could be dissolved and merged by particles in the outer surface, and meanwhile the solid sphere gradually develops into a hollow structures.

XRD patterns

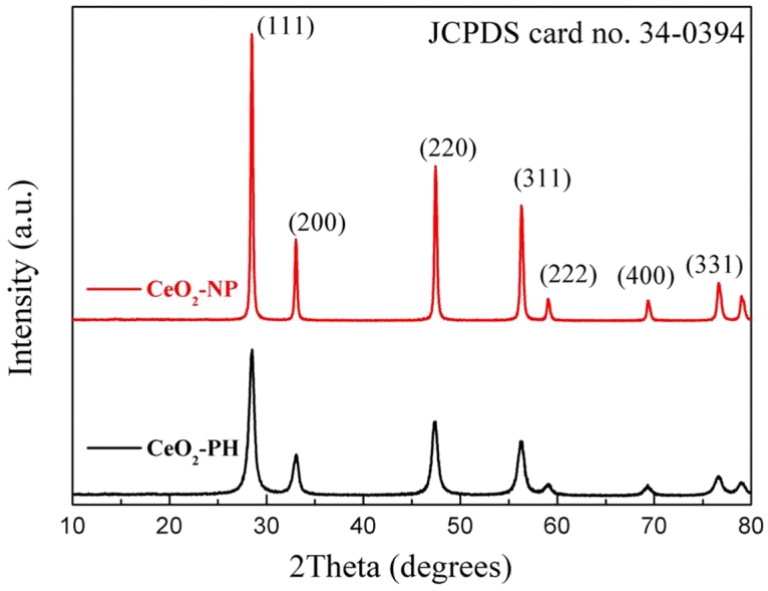

Figure 3.17 XRD patterns of both samples.

The phase purity of the prepared products was estimated by the XRD patterns. Figure 3.17 Shows the XRD patterns of CeO_2 - NP and CeO_2 - PH. All of the

characteristic peaks were indexed to the face-centered cubic phase with space group $Fm\bar{3}m$ of ceria (JCPDS card no. 34 - 0394). No other peaks were detected, and the sharp peaks indicated that the high purity and the highly crystalline nature of both samples. Compared with the CeO_2 - NP, the peaks of CeO_2-PH were relatively broad, demonstrating that the CeO_2 - PH was composed of smaller crystals. The average primary particle size was *ca.* 10 nm (Table 3.3), which is according to the calculation with the Debye-Scherrer formula for the strongest peak (111).

BET results

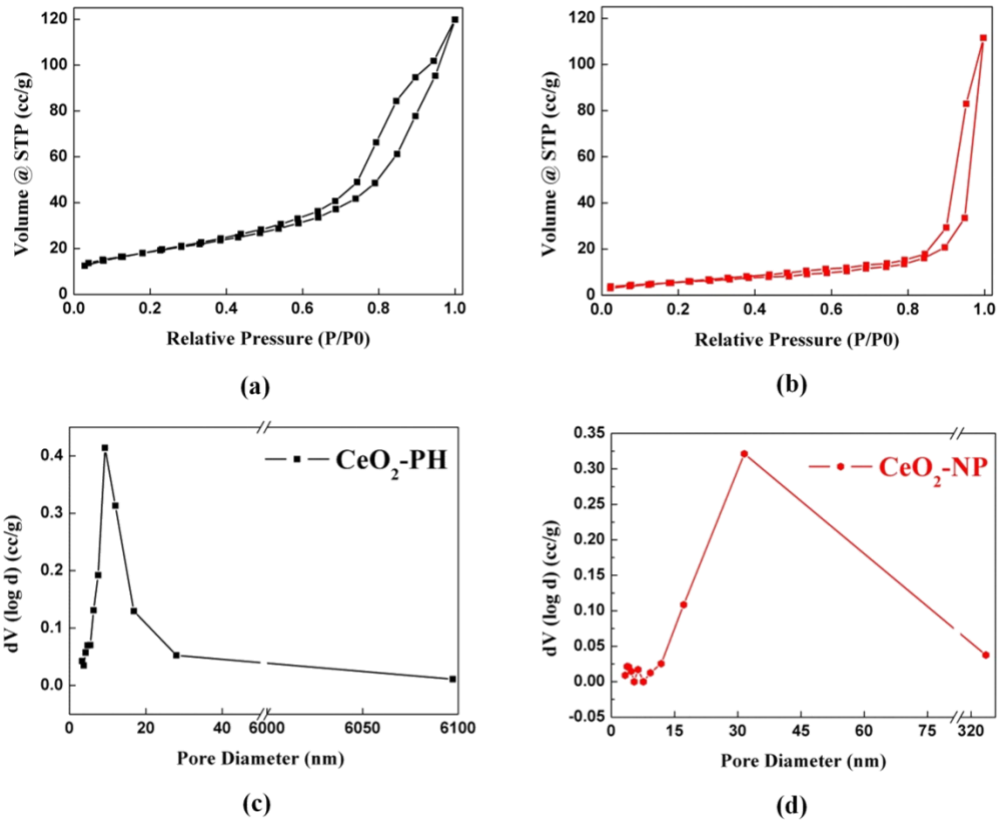

Figure 3.18. N2 adsorption–desorption isotherm, and the corresponding BJH pore size distribution curves, (a) – (c) CeO_2 – PH, (b) – (d) CeO_2 – NP.

Furthermore, the N_2 adsorption-desorption isotherms and pore size distribution of CeO_2 - PH and CeO_2 - NP are shown in Figure 3.18 The shape of the isotherm (Figure 3.18a) with a hysteresis loop ranging from 0.4 to 1.0 in the

relative pressure corresponds to a type - IV isotherm according to the Brunauer – Deming – Deming - Teller (BDDT) classification, simultaneously revealing the existence of a mesoporous structure in CeO_2 - PH. Figure 3.18b (CeO_2 - NP) exhibits the type - III isotherms with hysteresis loops at the relative pressures of 0.8 ~ 1.0, indicating the presence of structure. The pore size distribution of CeO_2 - PH (Figure 3.18c) was determined by the Barrett – Joyner - Halenda (BJH) method from the desorption branch of the isotherm. The pore size distribution is narrow, from 3 nm to 30 nm, in the mesoporous region, centered at 9 nm, and the pore volume is 0.181 cc/g, which is attributed to the aggregation of small crystal particles. However, CeO_2 - NP (Figure 3.18d) has a broad pore size distribution ranging from 10 nm to 350 nm and the pore volume is 0.173 cc/g, which is attributed to the void spaces among the stacked ceria nanoparticles. The specific surface areas of the CeO_2 - PH and CeO_2 - NP were 65.91 m^2/g, and 20.08 m^2/g respectively, which were calculated by the Brunauer – Emmett - Teller (BET) equation (Table 3.1).

Optical properties

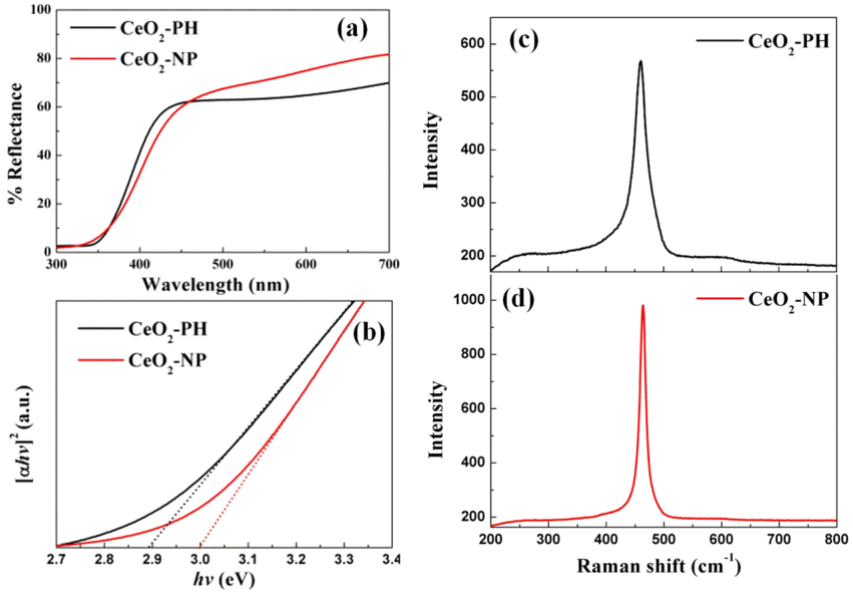

Figure 3.19. (a) UV - vis spectra, (b) KM transformed spectra, (c) – (d) Raman spectra.

The prepared CeO_2 - PH had fractional absorption in the visible region. As semiconductor materials, the indirect band gap (Eg) can be calculated from the equation of ahv = A (hv - Eg)^2, where hv is the photon energy, a is the absorption coefficient, and A is a constant of CeO_2. Calculated Eg values for CeO_2 - NP and CeO_2 - PH were 2.88 eV and 3.01 eV, respectively (Figure 3.19b), which are smaller than the theoretical value of 3.2 eV for bulk CeO_2. There are two plausible theories for the expatiation of the final moderato red-shift of the CeO_2 - PH. The existence of quantum confinement effect due to the nanoscale size of the primary particles forming the porous-hollow spheres resulted in a blue-shift in the UV - vis diffuse reflectance spectrum. Simultaneously, the decrease in primary particle size led to an increase in the Ce^{3+} ion concentration (XPS results in Figure 3.20). Chen et al. found out that the blue-shift of the absorption edge in a CeO_2 film occurred with a decrease in the Ce^{3+} content. Therefore, the red-shift of the band gap for CeO_2 - PH should originate from the transformation between Ce^{4+} to Ce^{3+}. In conclusion, band gap narrowing is the integrated result of the two mentioned reasons, which is beneficial for the photocatalytic process.

The visible Raman spectra are dominated by a strong F_{2g} symmetry mode of CeO_2 fluorite phase at 464 cm^{-1} on CeO_2 with weak bands at 258 cm^{-1} and 595 cm^{-1}, due to second-order transverse acoustic (2TA) mode and defect-induced (D), respectively. Compared with CeO_2 - NP (Figure 3.19d), CeO_2 - PH (Figure 3.19c) shown a stronger intensity in ca. 595 cm^{-1} (D), indicating that CeO_2-PH had much more intrinsic defects. The relative intensity ratios of I_D/I_{F2g} were calculated to be about 1.8% (CeO_2 - PH) and 0.5% (CeO_2 - NP). It has been proved that the presence of surface defects, such as large size oxygen vacancy clusters, would promote the transformation of Ce^{4+} to Ce^{3+} for CeO_2 - based materials.

Table 3.3 BET results and calculated values from XRD patterns

Samples	Surface area/g.m^{-2}	Grain size/nm
CeO_2 - PH	65.91	10.3
CeO_2 - NP	20.08	29.8

XPS spectra

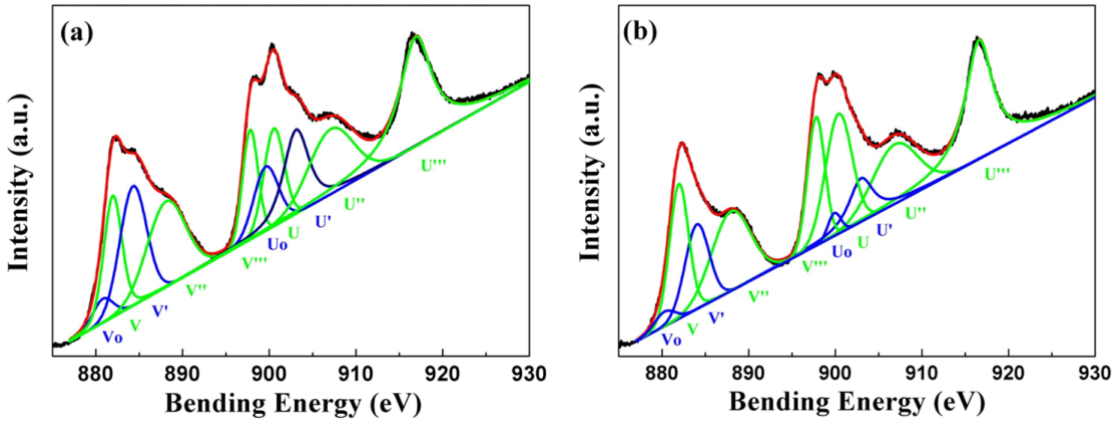

Figure 3.20. XPS spectra. (a) CeO_2 – PH, (b) CeO_2 – NP.

Figure 3.20 shows the Ce $3d_{3/2}$ and Ce $3d_{5/2}$ spectra of the CeO_2 - PH (a) and CeO_2 - NP (b), respectively. The spectra of Ce 3d can be decomposed into ten peaks by Gaussian-Lorentzian function fitting. According to previous research, the labels u, u'', u''', v, v'' and v''' refer to Ce $3d_{3/2}$ and Ce $3d_{5/2}$ are characteristic peaks of Ce^{4+} in CeO_2. For Ce^{3+}, the highest BE peaks U' and V' appear at 903.4 eV and 885.02 eV, respectively. These doublets correspond to Ce ($3d^94f^1$) O ($2p^5$). The lowest BE peaks U_0 and V_0 appear at 880.2 eV and 898.2 eV and correspond to Ce ($3d^94f^1$) O ($2p^6$). It can be seen that the chemical valence of cerium on the surface of the samples was a mixed valence state, and was mainly Ce^{4+} plus a small fraction of Ce^{3+}. The semi-quantified calculations of the amount of Ce^{3+} were following the equation $Ce^{3+} = [Av_o + Av' + Au_0 + Au'] / [Av_o + Av + Av' + Av'' + Av''' + Au_0 + Au + Au' + Au'' + Au''']$, and the values were 30.1% (CeO_2 - PH) and 17.6% (CeO_2 - NP), respectively. The high content of Ce^{3+} in CeO_2 - PH was ascribed to the

solvent (ethylene glycol), smaller primary particle size, and more oxygen vacancy defects. Ethylene glycol has reducibility and Ce^{4+} can be converted into Ce^{3+} in the reaction process. In the case of more oxygen vacancy defects, proved in Raman spectra (Figure 3.19), more oxygen vacancy defects facilitated more amount of Ce^{3+}. The reason why CeO_2 - PH (100) can generate a large amount of Ce^{3+} compared with CeO_2 - NP (111) is associated with the exposed crystal planes. The oxygen vacancy formation energy, nature and amount of the defects and low coordination sites are intrinsically affected by the surface planes of the ceria nanoshapes. Based on density functional theory calculations, the stability follows the sequence (111) > (110) > (100), while the activity follows the opposite order. The energy required to form oxygen vacancies on the (100) surface is less than those on the (111) and (110) surfaces due to its intrinsic high energy.

Photocatalytic activities

The photocatalytic activity of CeO_2 - PH was examined in acetaldehyde decomposition reaction under visible light irradiation, and the activity of CeO_2 - NP and P25 were also estimated in the same condition for comparison. Figure 3.21a shows the CO_2 evaluation activities of CeO_2 - NP, CeO_2 - PH and P25. After 24 h visible light irradiation, the degradation efficiencies of P25, CeO_2 - NP and CeO_2 - PH were ca. 5%, 25% and 92%, respectively. The activity of CeO_2 - PH sample was about 4-times higher than the contrast sample for CeO_2 - NP, and the 18 times higher than the P25 (P25 has no response to the visible light). One plausible reason of the higher activity is the larger S_{BET} of CeO_2 - PH. Compared with CeO_2 - NP the porous and hollow structure was the predominant reason for the higher S_{BET}, which provided superior adsorption and reactive sites for decomposition of acetaldehyde. Figure 3.21b shown the absorption and degradation of acetaldehyde. However, the primary particle size (ca. 10 nm) of the CeO_2 - PH was smaller than that of CeO_2 - NP (50 nm ~

100 nm), as observed in FESEM images. The presence of quantum effects has a great influence on properties of the surfaces of samples, such as electrical and optical performances. These special properties play the critical roles in the photocatalysis process, which can be as another more important credible reason for the excellent photocatalytic performance. The surface property and mechanism are discussed in detail in the following section. In order to estimate the stability of the CeO_2 - PH, cycling performance was tested. The result was shown in Figure 3.21c. After 6 h irradiation, the generation of CO_2 were 376.226 ppm (first), 361.593 ppm (second) and 370.159 ppm (third), which indicated that the stability of photocatalyst (CeO_2 - PH) was excellent.

Figure 3.21d shows the photocurrent responses of the photoanodes prepared from CeO_2 - PH and CeO_2 - NP. As anticipated, CeO_2 - PH exhibited an excellent photoelectrochemical response, being about 5 times higher than that of CeO_2 - NP. The enhancement of the photocurrent for CeO_2 - PH can be attributed to the improvement of light-harvesting, as shown in the result for band gap value. In addition, the high content of Ce^{3+} ions would be trapped by the photogenerated holes, and then facilitated the separation of the photogenerated electron - hole pairs. The trapped holes would restrain the recombination of the photogenerated electron - hole, and then enhanced the photocurrent response. As a result, CeO_2 - PH (higher Ce^{3+} ion content) has a stronger photoelectrochemical response, which is in accordance with activity in the evaluation of acetaldehyde degradation. Moreover, the defects, shown in Raman and XPS characterizations, in CeO_2 - PH might lead to the formation of a surface state energy band of oxygen and the oxygen adsorption, desorption and diffusion processes would easily occur on the surface, resulting in notable changes in the properties of CeO_2 - PH such as optical and electrical properties. When the incident light is larger than the band gap, previously adsorbed

oxygen on the surface of the CeO_2-PH will desorb and release free electrons, causing the conductivity to increase.

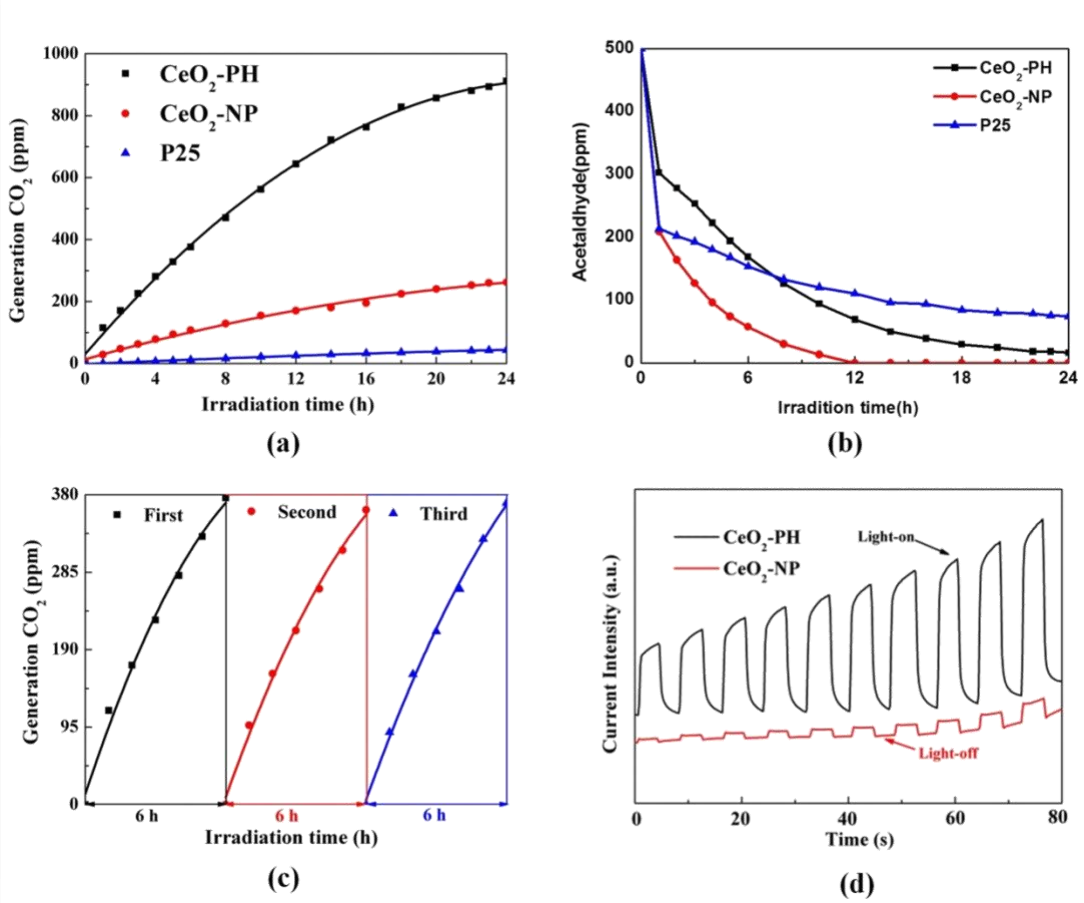

Figure 3.21. (a) – (b) Time courses of CO_2 evolution from acetaldehyde decomposition over the products under visible-light irradiation, (c) cycling performance of CeO_2 - PH, (d) photocurrent response.

3.5.3 Conclusions

In summary, porous CeO_2 hollow spheres were successfully synthesized by a one-step solvothermal method in the absence of any templates. Based on the morphology evolution of that time-dependent samples, it is thought that Ostwald ripening occurs and that it is the main driving force for the core evacuation of solid aggregates during the hollowing process. Furthermore, the prepared CeO_2 - PH has high activity for decomposition of the acetaldehyde. The presence of Ce^{3+} and oxygen vacancies in CeO_2 - PH enhanced the light

harvesting and provided activity sites in the photocatalytic process. In addition, this prepared special porous-hollow sphere can be used in many potential applications in the future.

3.6 Conclusions and improvement

In this chapter, various kinds of cerium dioxide with different morphologies have been prepared. Their surface area improved a lot. However, visible light absorption should be enhanced further.

In chapter 4, we will focus on the improvement of visible light absorption.

Chapter 4 Improvement of photocatalytic activity by cerium (III) control of cerium dioxide

4.1 Introduction

Although CeO_2 has been utilized as a photocatalyst, the band gap of CeO_2 is about 3.1 eV, and UV light would be necessary for its photocatalytic reactions to proceed. In order to utilize solar light that includes only 3% UV light and 50% visible light as a light source, the development of visible light - responsive ceria is necessary. Various strategies including morphology control, [4] ion doping, [5] combining with other materials, [6] and noble metal deposition [7] have been adopted to improve the photocatalytic property of CeO_2 via enhancing the absorption of visible light. Other researchers have also reported that visible light absorption of the photocatalysts was increased by loading Au, Ag, Pt and other noble metals on the CeO_2 surface. The improved photocatalytic performance can be contributed to surface plasmon resonance (SPR) effects. Ana et al. [12] reported that deposition of gold nanoparticles on the surface of photocatalysts with a small amount of loading improved the photocatalytic activity under visible light, which exhibited higher photocatalytic activity than the same material upon irradiation at its band gap. However, the main drawback of this method is that new material must be introduced. We have to bear the cumbersome synthesis steps and additional materials with high prices such as noble metals.

Herein, through a simple solvothermal method, we prepared a reduced CeO_{2-x} with special various morphologies (hollow porous sphere and confeito-like) and long range visible light absorption. Moreover, the proportion of visible light absorption is significantly improved compared with that of commercial CeO_2 (from HIGH PURITY CHEMICALS Co. Ltd.), labeled as HPC-CeO_2 , which could be attributed to the high content of Ce^{3+} . Additionally, a new absorption

peak is arose around 500 nm, which is extremely similar to Surface Plasmon Resonance (SPR) effect. [13] This is the first time for visible light absorption to be greatly improved by only regulating the trivalent cerium content without any doping or loading. In virtue of special morphology and good visible light absorption, their performances have been greatly improved.

4.2 Experimental section

4.2.1 Materials

The materials for the preparation of samples are same as that of chapter 3.5.

4.2.2 Synthesis of cerium dioxides with various contents of cerium (III)

The route for the synthesis of samples is same as that of chapter 3.5. The ratios of ethylene glycol were adjusted for the various contents of cerium (III). **Confeito like cerium dioxide.** All the processes are same, except the heating step. The suspension was transferred to a 100 - mL Teflon - lined autoclave and heated at 160 °C for 3.5 h, then warming up to 180 °C and keep for 20.5 h.

Pure cerium dioxide. Typically, 3.0 g of cerium (III) nitrate hexahydrate ($Ce(NO_3)_3 \cdot 6H2O$) was dissolved in 80 mL of NaOH solution (m_{NaOH} = 6.4 g) under vigorous stirring. The suspension was transferred to a 100 mL Teflon-lined stainless - steel autoclave and held in 140 °C for 9 h. After cooling to room temperature, the product was collected by centrifugation, washed with ethyl alcohol and water until the ionic strength was less than 10 μs/cm, and dried at 70 °C overnight. The sample will be reserved under black - UV illumination for photocatalytic evaluation.

4.2.3 Characterization

The characterizations for the properties are same as that of chapter 3.5.

4.2.4 Evaluation of activity

The method for the activity evaluation is same as that of chapter 3.4. The only difference is that the light source is visible light.

4.2.5 SERS

The as - prepared products were used as SERS active materials to detect MB molecules. Typically, 5 mg of as-synthesized both samples were added to 1 mL of different concentration of MB solution in a centrifuge tube. The mixture was allowed to equilibrate for 1 h. A total of 20 μL of the mixture were transferred to silica slides and allowing it to evaporate naturally. Raman spectra were obtained by a laser Raman spectrum (JASCO, NRS - 5100). Spectra were collected with accumulation times of 2 s and the laser power was maintained at 5.2 mW. Lasers with wavelength 523 nm was used as the excitation light source.

4.2.6 Photocurrent response experiment

The route for testing photocurrent response is same as that of chapter 3.5.

4.2.7 Computational methods

All calculations (geometric optimization, transition state search, frequency verification) were performed at the DFT B3LYP/6-31G (d,p) level of theory using the Gaussian 09 package with the tight SCF convergence criterion and fine integration grids. The energy of three states are - 194.36860681 Ha (isopropyl alcohol), - 194.34485549 Ha (acetone), and - 194.23074744 Ha (Trans State). After normalization based on isopropyl, the relative energy of three states are 0.00 eV, 0.65 eV, and 3.75 eV. 1 Hartree = 27.2138505 eV.

4.3 Results and discussion

4.3.1 Structure and composition

FE – SEM and TME

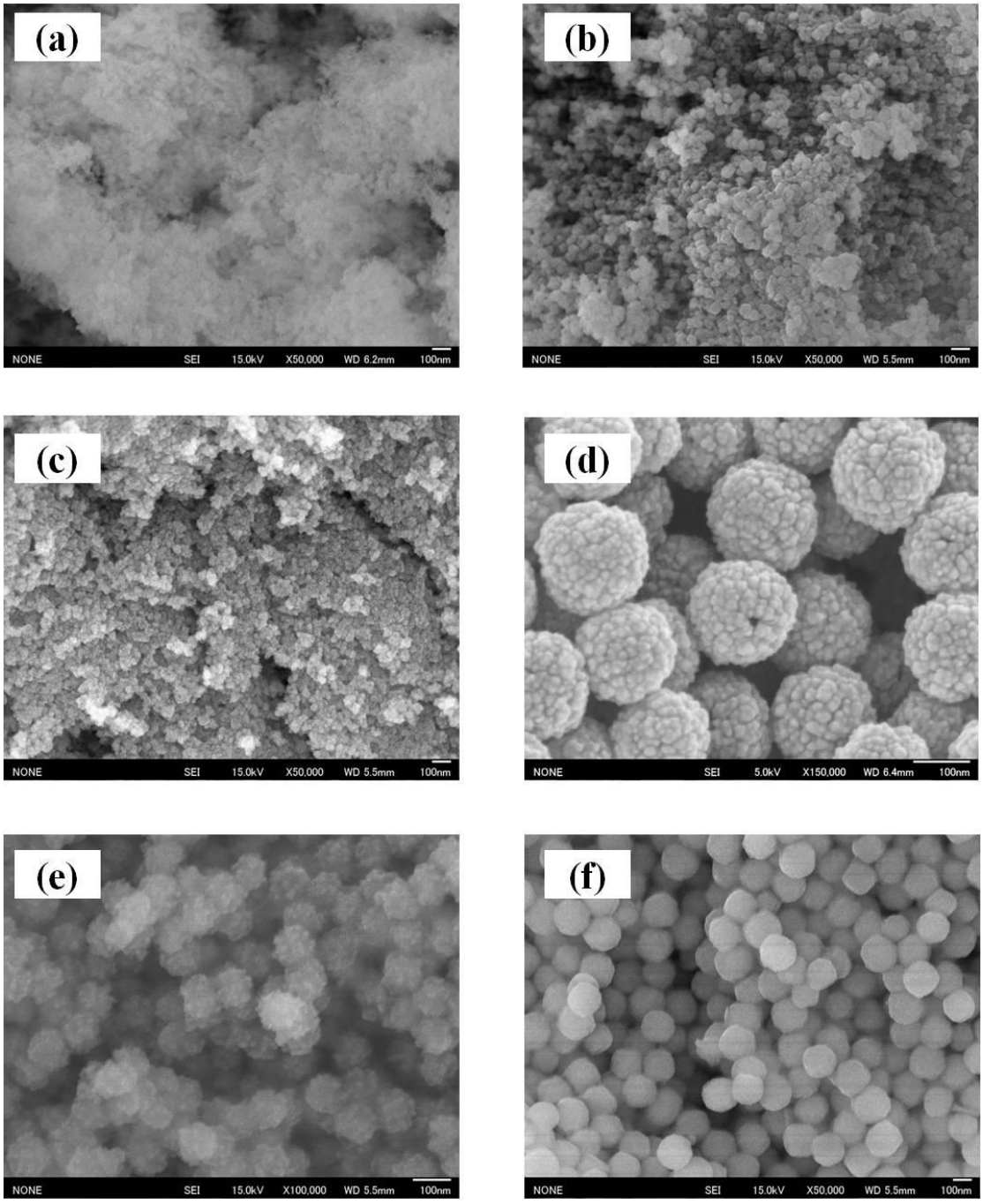

Figure 4.1. SEM images of all the samples. (a) CeO_2 – pure, (b) CeO_2 – EG (0 mL), (c) CeO_2 – EG (10), (d) CeO_2 – EG (20 mL), (e) CeO_2 – EG (30 mL), (f) CeO_2 – EG (40 mL).

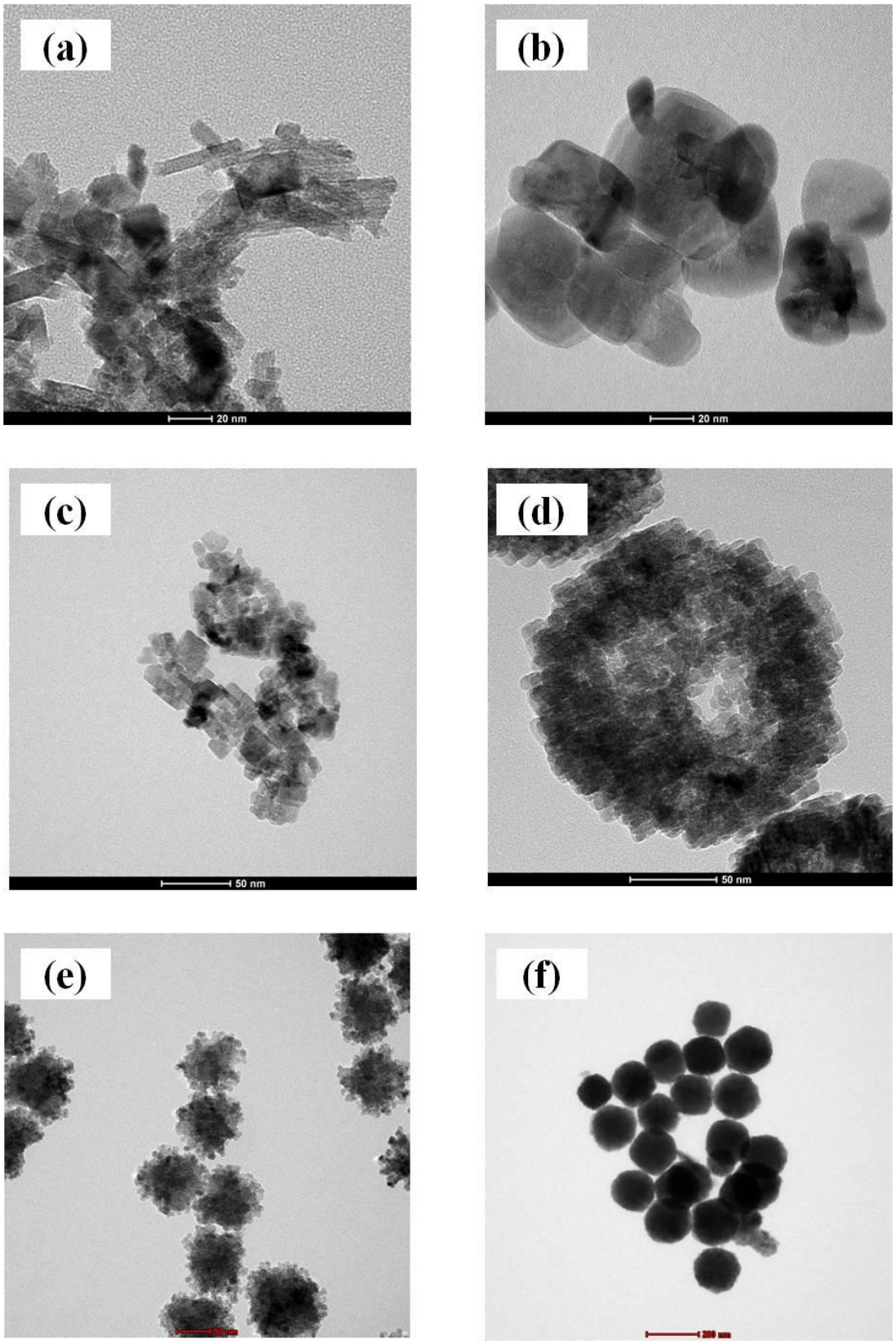

Figure 4.2. TEM images of all the samples. (a) CeO_2 – pure, (b) CeO_2 – EG (0 mL), (c) CeO_2 – EG (10), (d) CeO_2 – EG (20 mL), (e) CeO_2 – EG (30 mL), (f) CeO_2 – EG (40 mL).

The morphologies of the as-prepared various-CeO_2 photocatalysts are shown in Figure 4.1 and Figure 4.2. Figure 4.1 shows SEM images of ceria nanoparticles, nano sphere, porous sphere, confeito-like particles. With the different ratios of EG, different morphologies have been obtained. CeO_2 – pure, CeO_2 – EG (0 mL) and CeO_2 – EG (10 mL) are all irregular nanoparticles and with some agglomeration, showing Figure 4.1a ~ c. According to the TEM images, hollow structure could be confirmed. CeO_2 – EG (20 mL) is a porous-hollow sphere, which has been investigated previously, which has an excellent activity for degradation of acetaldehyde (Figure 4.2d). CeO_2 – EG (30 mL) is confeito-like particles, which diameter is ca. 100nm, showing Figure 4.2e. Moreover, CeO_2 – EG (40 mL) is a spherical particle, and its diameter is ca. 180 nm (Figure 4.1f). The detail information of the particles would be observed in TEM images. We can confirm that CeO_2 – EG (40 mL) didn't own hollow structure.

XRD patterns

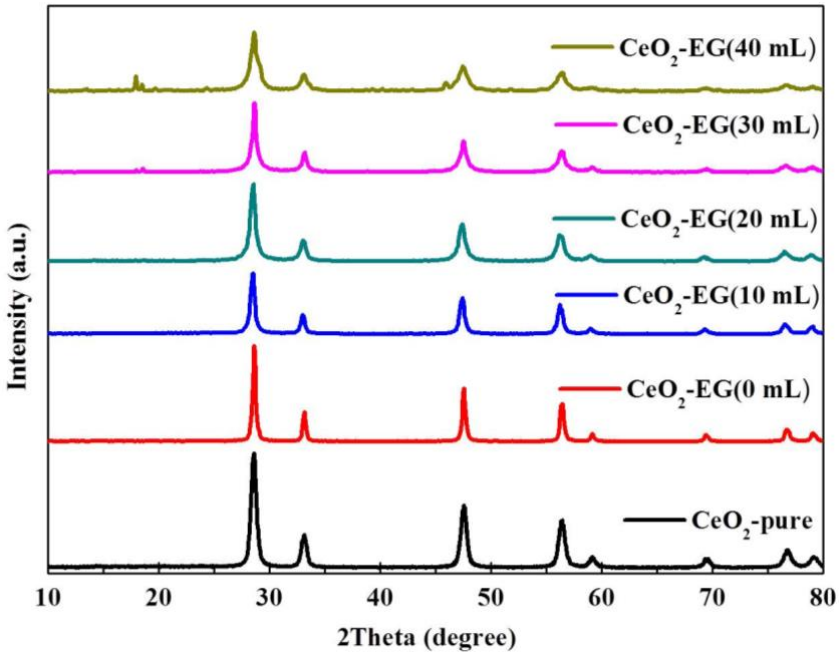

Figure 4.3. XRD patterns of all the samples.

The crystallinity of various CeO_2 was characterized by X-ray diffraction (XRD) in Figure 4.3. All the main peaks are assigned to the fluorite cubic CeO_2 phase

(JCPDS No. 04-0593). However, it should be note that there are some un-neglected peaks of sample EG (30mL) - CeO_2 and EG (40mL) - CeO_2. The new peak at ca.17°could be attributed to the CeO_{2-x} (Ce_2O_3, Ce_7O_{12}). It means that CeO_2 has been partial reduced due to the ratio of EG (reductant). When the amount of EG increased to 40 mL, the crystal phase started changing or generating new phase.

UV-vis spectra

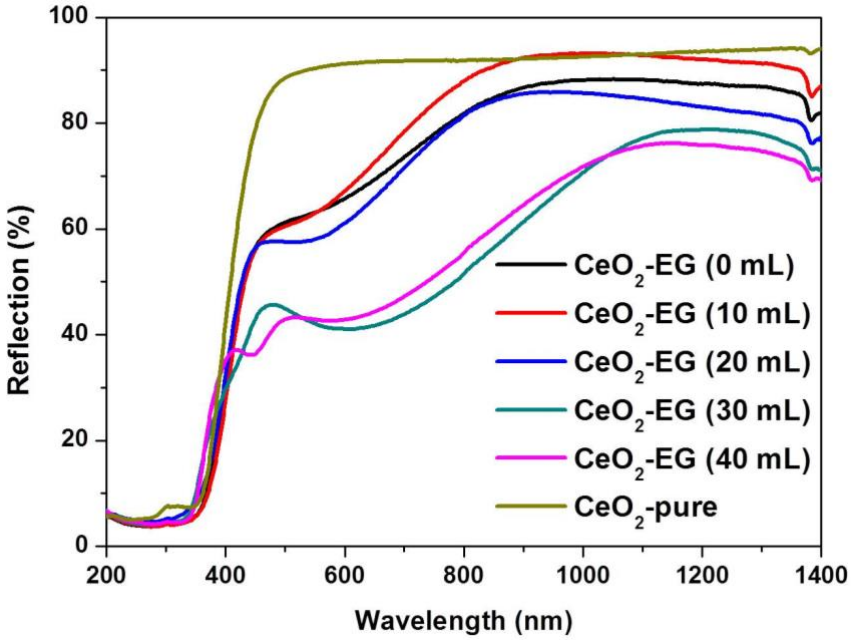

Figure 4.4. UV –vis spectra of all the samples.

In order to investigate the light response of the variou-CeO_2 photocatalysts, UV - vis characterization is necessary. Figure 4.4 shows the UV - vis diffuse reflectance spectra, all the CeO_2 has enhanced visible light response arrange from 400 nm to 900 nm compared to pure CeO_2, which phenomenon was similar to LSPR. And the strongest intensity of absorption is EG (30mL) - CeO_2. The effect could be attributed to the large content of Ce^{3+} (Figure 4.5), which could be confirmed by XPS results. According to the previous research, to sustain surface plasmons in a semiconductor, the concentration of accumulated free carriers (electrons or holes) must be above the threshold value,

turning its real part of dielectric permittivity negative. In general, this prerequisite in semiconductors is met through introduces aliovalent atoms or lattice vacancies. As a consequence, the upper limit of carrier concentration in semiconductors is determined by the equilibrium between Ce^{3+} and Ce^{4+}. CeO_{2-x} satisfied the requirements above, therefore leading to their plasmon resonance frequency.

XPS spectra

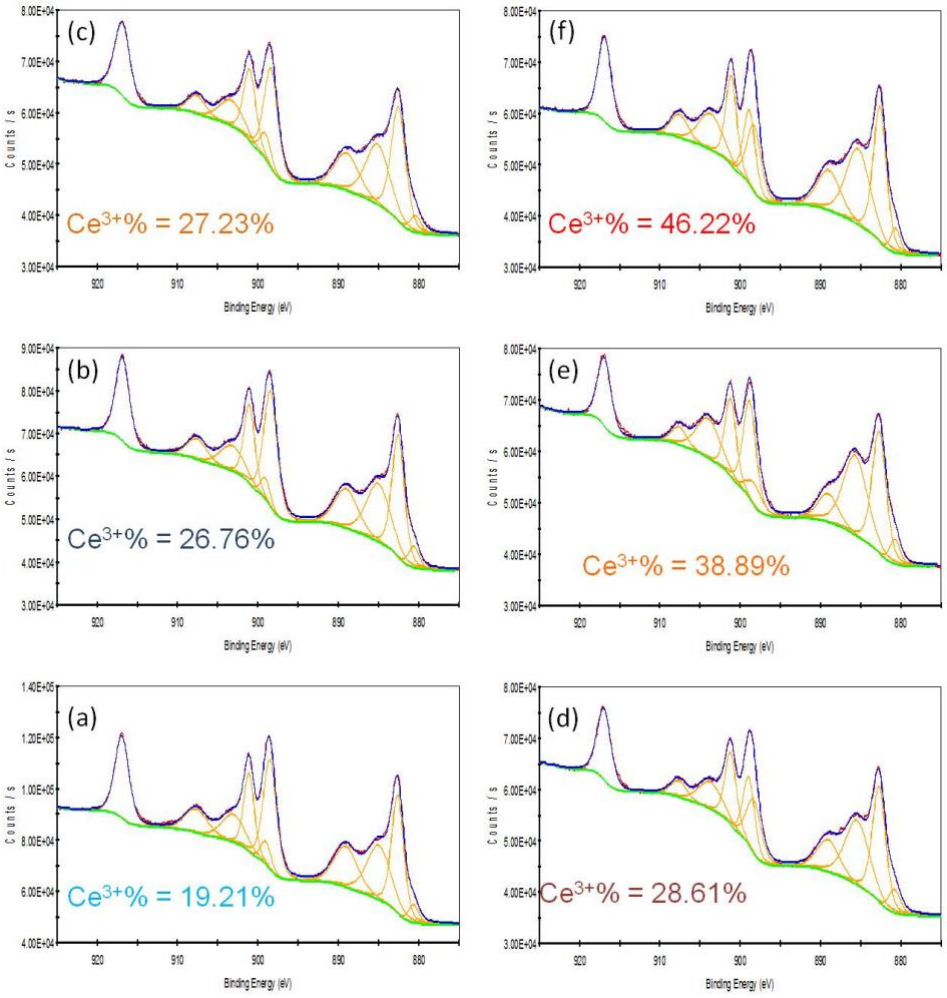

Figure 4.5. XPS spectra of all the samples. (a) CeO_2 – pure, (b) CeO_2 – EG (0 mL), (c) CeO_2 – EG (10 mL), (d) CeO_2 – EG (20 mL), (e) CeO_2 – EG (30 mL), (f) CeO_2 – EG (40 mL).

The relative contents of Ce^{3+} have been calculated, and the values were 19.21% (CeO_2 – pure), 26.76% (CeO_2 – EG (0 mL)), 27.23% (CeO_2 – EG (10 mL)), 28.61% (EG(20mL)-CeO_2), 38.89% (CeO_2 – EG (30 mL)) and 46.22% (CeO_2 – EG (40 mL)), respectively. It was clearly indicated that the content of Ce^{3+} enhanced with the increase of EG.

4.3.2 Investigation of the relationship between activity and cerium (III)

Activity results

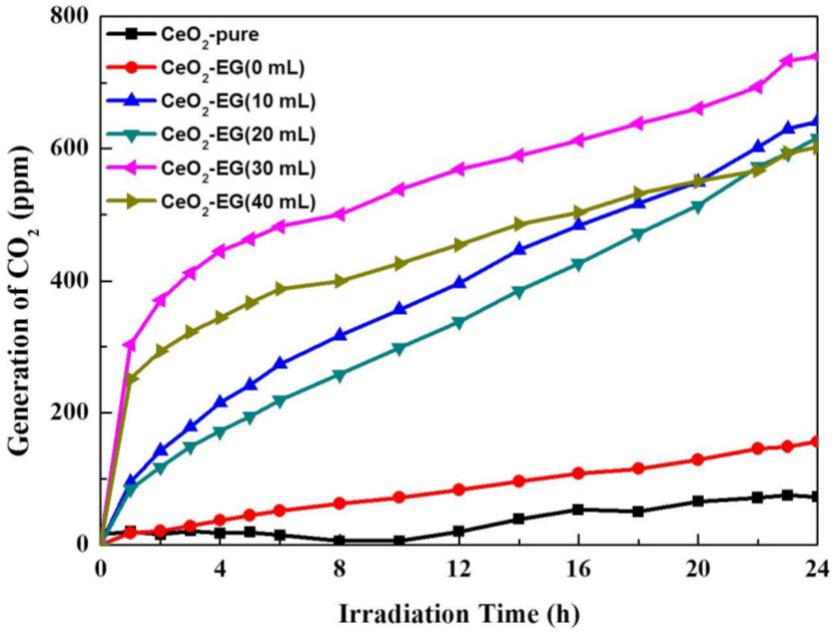

Figure 4.6. Photocatalytic activities of all the samples.

Figure 4.6 displays the time-online photocatalytic results for the gas-phase degradation of 2 - propanol over the various samples of different ratios of EG and commercial CeO_2. As can be seen, during the reaction of 24 h, the sample of EG (30mL) - CeO_2 exhibits the excellent photocatalytic performance toward the gas - phase degradation of 2 - propanol in view of the generation amount of CO_2, which is 10 times than that of commercial - CeO_2. The high activity could be attributed to strongest absorption due to high content of Ce^{3+} on the surface.

Relationship between Ce^{3+} and activities

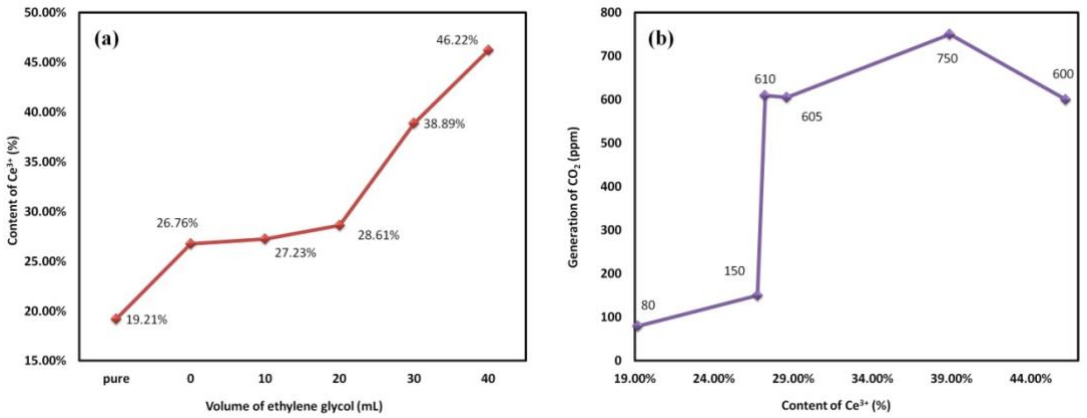

Figure 4.7. Relationships among EG, Ce^{3+}, and activities. (a) EG and Ce^{3+}, (b) Ce^{3+} and activities.

The relationships among EG, Ce^{3+}, and activities were shown in Figure 4.7. Figure 4.7a exhibited the relationship between EG and Ce^{3+}. With the increase in the proportion of EG, the content of Ce^{3+} also increased. According to the UV-vis spectra, the absorption has two variation tendency. Sharp increase – flat - sharp increase. Figure 4.7b shown the activities of all samples changed. With the increase of Ce^{3+}, the activity enhanced. However, continued to increase the content of trivalent cerium, activity decreased. The reason could be attributed to that the lager amount of Ce^{3+} could be a recombination center. So the activity decreased.

4.3.3 Conclusions

In this section, we investigated the relationships among the content of Ce^{3+}, ratio of ethylene glycol and the photocatalytic activity.

There is an optimum condition for the best photocatalytic activity: CeO_2 – confeito.

In next section, we explored the optimum condition for preparing the CeO_2 – confeito.

4.4 Confeito like cerium dioxide

4.4.1 FE – SEM and TEM

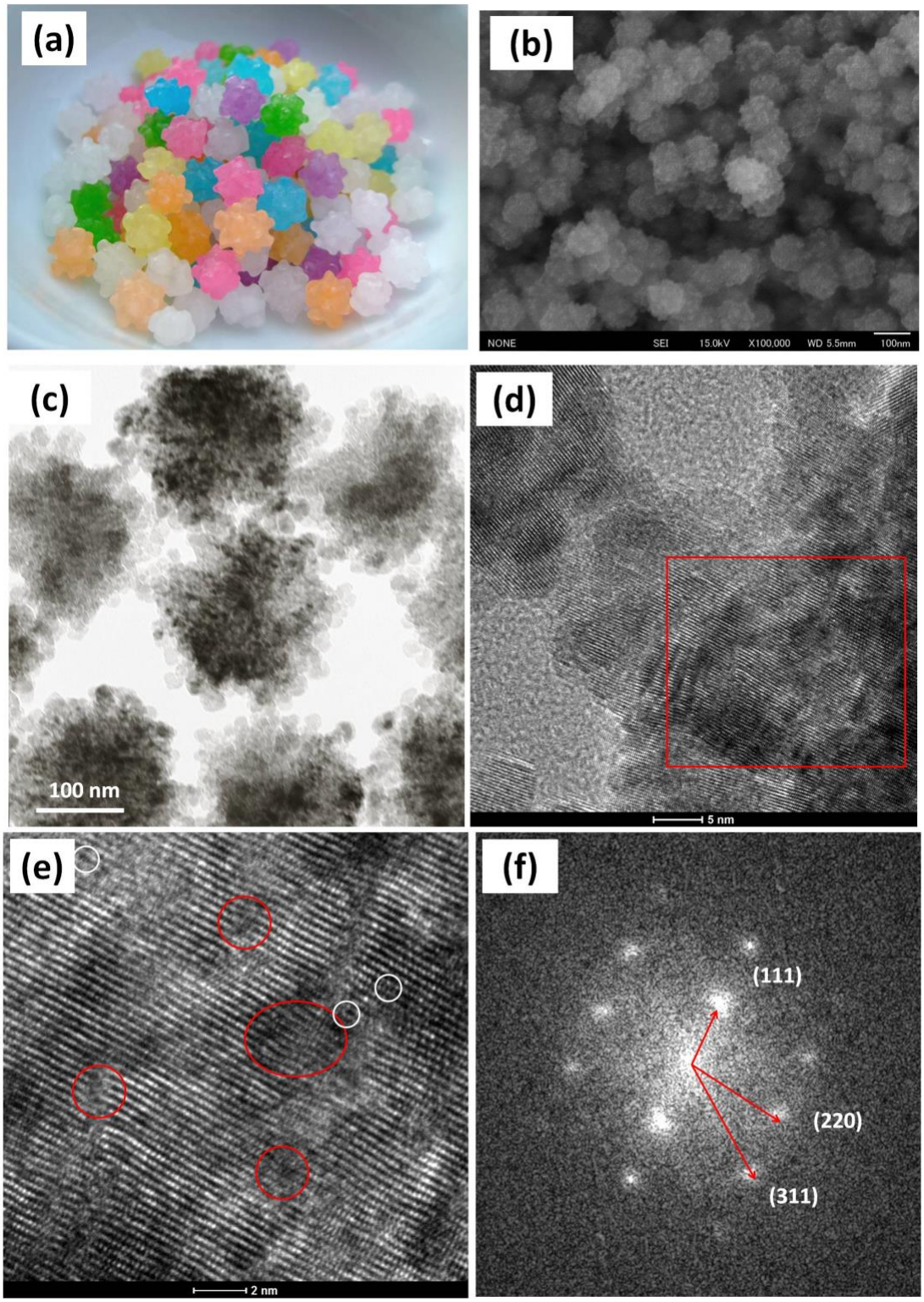

Figure 4.8. (a) Photo of confeito candy, (b) ~ (e) TEM images of CeO_2 – Confeito, (f) SAED result.

The unique morphology CeO_2 was prepared via a two-step solvothermal method. We speculated that crystal nuclei formed at a relatively low temperature, and then assembled into large particle at 160°C and growth at 180°C. We could observe the confeito-like morphology of CeO_{2-x} is shown in Figure 4.8. Its diameter is ca. 170 nm and there are some small tentacles on the surface. The size of the primary grains composed of large particles is about 10 nm, being in agreement with the XRD results. An HRTEM image and FFT (Fast Fourier Transformation) pattern are collected in Figure 4.8e ~ f, respectively, corresponding to the selected rectangular area in Figure 4.8d. There is a well-defined lattice fringe, indicating its better crystallinity. However, there are some oxygen vacancies and defects in the Confeito-CeO_2 lattice structure due to its high content of Ce^{3+}. The indexing of the FFT pattern shows (111), (110) and (311) lattice planes, which is in good agreement with the DFT results showing that oxygen vacancies preferentially form in the (110) facet. As for HPC-CeO_2, it indeed has a large surface area due to its small particle size as shown in SEM and TEM images (in chapter 2). However, aggregation, optical property, and band structure restrict its performance.

4.4.2 XRD patterns

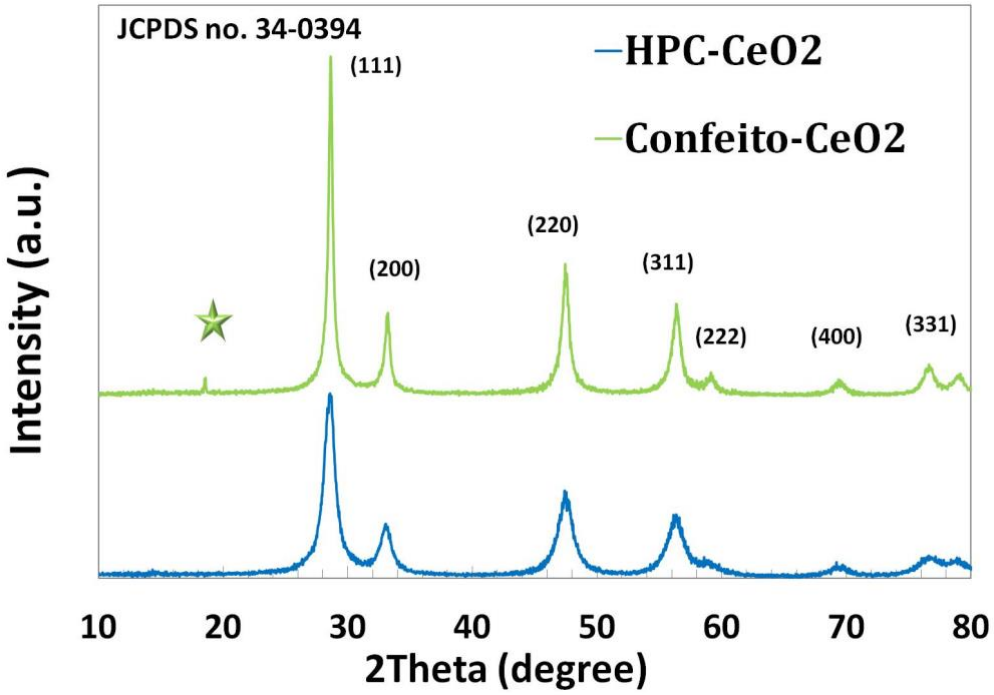

Figure 4.9. XRD patterns of both samples.

The crystallinities of HPC-CeO_2 and Confeito-CeO_{2-x} characterized by X - ray diffraction (XRD) are shown in Figure 4.9. All of the main peaks are assigned to the face-centered cubic phase with the space group $Fm\bar{3}m$ of CeO_2 phase (JCPDS No. 34-0394). The intensity and FWHM of Confeito-CeO_2 are stronger and narrower, respectively, than those of HPC-CeO_2, indicating that the crystallinity and grain size of Confeito-CeO_2 are better and smaller, respectively. The detail information of grain size is summarized in Table 1, which is according to the calculation by the Debye-Scherrer formula for the strongest peak (111). However, it should be noted that there are some unneglectable peaks of sample Confeito-CeO_2. A new peak appeared at ca.18.4°, which could be indexed to the reduced CeO_2, being attributed to the fact that CeO_2 had been partially reduced by the ratio of EG (reductant). The partial reductant material (CeO_{2-x}) would have a great impact on the visible light absorption and photocatalytic property.

4.4.3 UV-vis spectra and band gap structure

UV-vis spectra

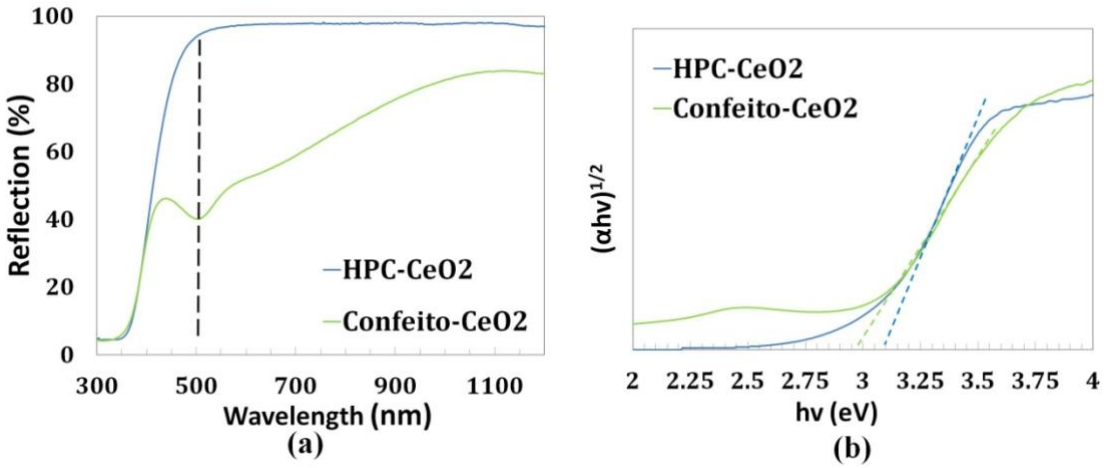

Figure 4.10. (a) UV-vis spectra, (b) KM transformed spectra.

Attention! UV - vis spectra are essential to photocatalytic activity. Confeito - CeO_2 possesses stronger absorption than that of HPC - CeO_2 in the wavelength range from 420 nm to 1000 nm in comparison to that of HPC - CeO_2 (Figure 4.10a). The improvement of visible light absorption has an intimate relationship with the reduced cerium dioxide (CeO_{2-x}). The analogous SPR absorption peak could be attributed to the substantial content of Ce^{3+} (38.8%), which could be confirmed by XPS results (Figure 4.5). According to plasmonic theory, to sustain surface plasmons in a semiconductor, the concentration of accumulated free carriers (electrons or holes) must be above the threshold value. In general, this prerequisite in semiconductors is met, through the introduction of aliovalent atoms or oxygen vacancies. As a consequence, it is reasonable to presume that the upper limit of the carrier concentration in Confeito - CeO_2 is determined by the equilibrium between Ce^{3+} and Ce^{4+}, corresponding to CeO_2 and CeO_{2-x}, thereby leading to their plasmon resonance frequency. Many researchers have obtained similar results in, for instance ITO, TiO_{2-x}, and MoO_{3-x}.[92-108] This SPR effect is originated to the free carriers by tuning the content of Ce^{3+}. In addition, the band gap values

of the samples were determined by plotting $[F(R)h\nu]^{1/n}$ vs. $h\nu$ (n = 2 for indirect band gap) as shown in Figure 4.10b. The narrowing of the band gap of Confeito - CeO_2 (Table 4.1) is associated with oxygen vacancies and formation of Ce^{3+}.

Mott-Schottky plots

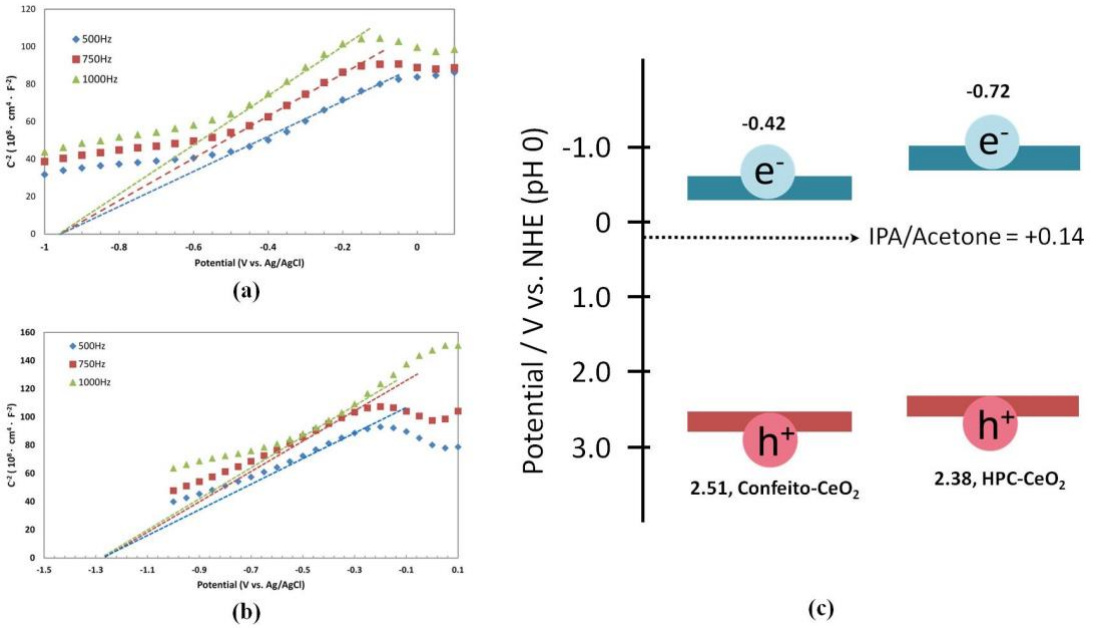

Figure 4.11. Mott-Schottky plots of both samples. (a) HPC - CeO_2; (b) Confeito - CeO_2, (c) Band structure diagram of both samples.

To obtain the band structure, Mott–Schottky analyses were carried out by using an Impedance Potential method at 0.5 kHz, 0.75 kHz and 1 kHz in Na_2SO_4 solution (pH = 6). Mott-Schottky plots of both samples are shown in Figure S6. Positive slopes at both frequencies were obtained, indicating that both samples behave as n - type semiconductors. In the case of n - type semiconductors, E_{fb} is generally located near the C.B., and it can be estimated from the intersection of a plot of $1/C^2$ against E by the following equation:

$$\frac{1}{C^2} = \frac{2}{e\varepsilon\varepsilon_0 N}\left(E - E_{fb} - \frac{kT}{e}\right),$$

where C is capacitance, e is the electron charge, ε is the dielectric constant, ε_0 is permittivity of vacuum, N is acceptor density, E is the electrode potential, E_{fb} is the flat band potential, k is the Boltzmann constant, and T is temperature. As shown in Figure 4.11, the x-axis intersections of the two samples are - 0.9 V (Confeito - CeO_2), and - 1.26 (HPC - CeO_2) vs. Ag/AgCl (pH = 6) for all frequencies (0.5 kHz, 0.75 kHz, and 1 kHz) and can be used to determine E_{fb} from the above equation $E_{fb} = E - kT/e$. The calculations showed that E_{fb} values were approximately - 0.44 V (Confeito - CeO_2), and - 0.72 (HPC - CeO_2) v.s. NHE (pH = 0) by correcting the solution pH. By combining with band gap results, we can roughly give the band positions of the two samples can be roughly given (Figure 4.11c). The oxidation potential of acetone/isopropanol was calculated by the Nernst equation, indicating that the V.B. level of both samples is sufficient for this reaction in theory.

4.4.4 BET results

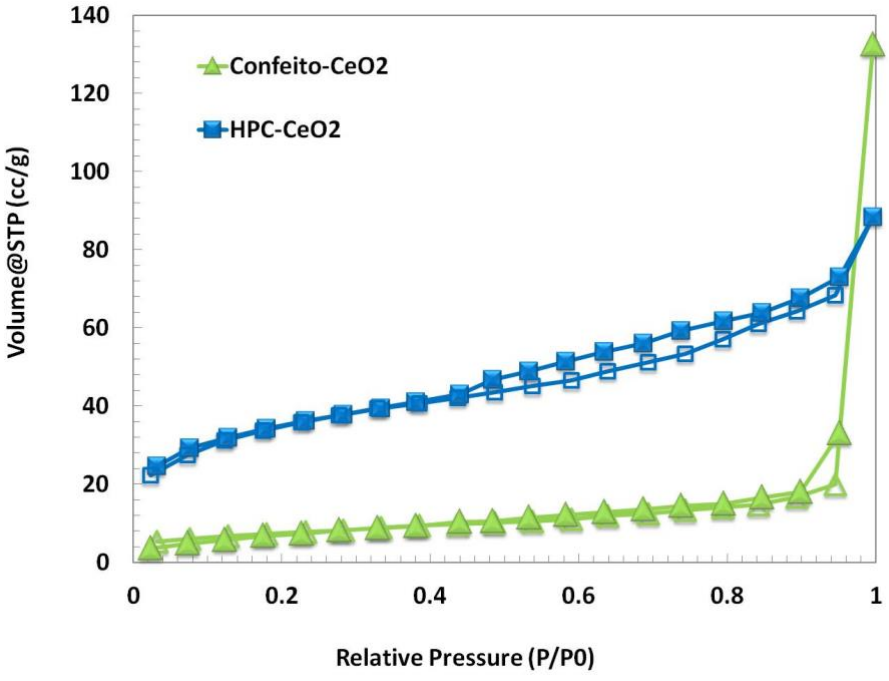

Figure 4.12. N_2 adsorption – desorption isotherm of both samples.

According to the Brunauer – Deming – Deming - Teller (BDDT) classification, HPC - CeO_2 and Confeito - CeO_2 are defined as Type - IV (mesoporous) and Type - III (macroporous), respectively (Figure 4.12). Mesoporous and macroporous are from the gap between particles. HPC - CeO_2 is mesoporous because of the aggregation of particles, and Confeito - CeO_2 is macroporous because the small tentacles on the surface widen the gaps between particles.

4.4.6 Photocatalytic activities

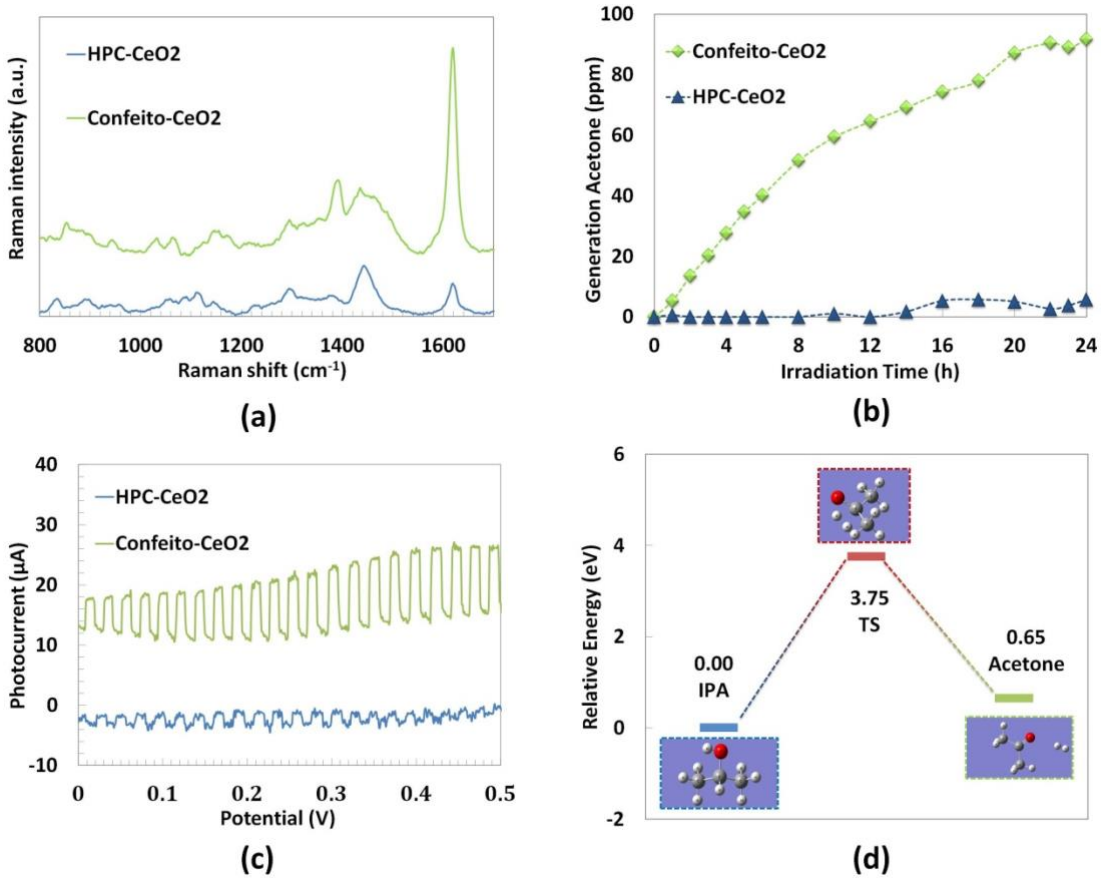

Figure 4.14. Performance of both samples. (a) SERS activity; (b) decomposition of IPA to acetone; (c) photocurrent response from Linear sweep voltammetry; (e) Gaussian-calculated relative energy profiles for transition state between IPA and acetone.

Herein, we obtained its SERS activity that based on plasmonics are shown in Figure 4.14a. It is apparent that the Raman signals of MB significantly enhance

on the surface of Confeito - CeO_2. It can be as indirect evidence of the SPR effect.

Based on the above results, we utilized CeO_{2-x} as a photocatalyst for the decomposition of isopropyl alcohol (IPA) to generate acetone. The time courses of acetone formation in photocatalytic oxidation of 2-propanol under Xe lamp (cutoff = 420 nm) irradiation are presented in Figure 4.14b. With irradiation for 24 h, the generated amount under Confeito - CeO_2 is approaching to 100 ppm. It is about ten-times greater than that of HPC - CeO_2. The paramount factor for such excellent activity is the substantial content of Ce^{3+} in Confeito - CeO_2. In the first place, Ce^{3+} will narrow the band gap, and then more visible light can be utilized for the photocatalytic process. Moreover, some CeO_{2-x} materials form due to Ce^{3+}, which further expands its absorption ranging from 420 nm to 1000 nm. There is one more point that should be noted: charge separation will also promote activity. The photoelectrochemical properties of the two types of CeO_2 were characterized by measuring the photocurrent under a 500 W Xe lamp equipped with a cutoff filter (λ = 420 nm). As anticipated, Confeito - CeO_2 exhibited an excellent photocurrent response, about 5-times higher than that of HPC - CeO_2 (Figure 4.14c). This result is evidence for better charge separation and light harvest. The last but not the least, the confeito unique shape also plays a role in the reaction. Moreover, 90% of IPA had been consumed via adsorption and conversion one hour later. However, the consumptions of IPA in the two samples are approaching, indicating that surface area is a negligible factor. Dominant factors are oxygen vacancies (due to Ce^{3+} and the (110) facet) and monodispersity.

Finally, we raise a question. Why is the rate of this photocatalytic process slow? How can we speed up the reaction? It is easy to think that there is a transition state between IPA and acetone. We therefore calculated transition state (TS) information with Gaussian software and verified its reliability by calculating the

frequency (only one imaginary frequency). Figure 4.14d shows the thermodynamic and kinetic process of the reaction. Although the full reaction is an uphill process, the energy is less than that of the ground state to transition state. According to this, we can speculate that the V.B. position of Confeito-CeO_2 satisfies the oxidation potential of TS, while the potential difference is not sufficient. In the future, we will adjust the content of Ce^{3+} to lower the V.B. position and speed up the reaction.

4.4.7 Conclusions

In summary, a reduced CeO_{2-x} material was successfully prepared via a simple hydrothermal method. The unique confeito-like particles possess a long range of visible light absorption due to the substantial content of Ce^{3+}. The special absorbed peak at ca. 500 nm even leads a SERS activity, indicating the generation of SPR effect. This SPR effect is originated to the free carriers by tuning the content of Ce^{3+}. Meanwhile, the valence band is modified to be more positive, which is beneficial for photocatalysis. Summed up the results, the Confeito - CeO_2 exhibits an excellent performance for decomposition of isopropyl alcohol to acetone. This work shows new opportunities for photocatalytic preparation with long range visible light absorption and more positive V.B. by controlling the content of Ce^{3+}.

4.5 Conclusions and improvement

In this chapter, visible light absorption of cerium dioxide has been improved via controlling the contents of Ce^{3+}. A optimized content of Ce^{3+} was confirmed via the ratio of ethylene glycol. However, this visible light absorption is not enough for the requirement of photocatalysis.

In future, we will focus on the significant improvement of visible light absorption by construction of cerium dioxide – based heterojunctions.

Conclusions and future plans

General conclusions

We have prepared various morphologies of CeO_2, including nano – octa, nano – sphere, nano – flake, porous hollow sphere, confeito – like. Compared with bulk CeO_2, these special CeO_2 nanoparticles own larger surface area, which can enhances the absorption amount of reactants and promotes the process of photocatalysis.

Light harvest is the key point for the activity of photocatalyst, so we has enhanced their light absorption by tuning the content of Ce^{3+}. Suitable content of Ce^{3+} is favor to the activity, however, continued to increase the content of trivalent cerium, activity decreased. The reason could be attributed to that the lager amount of Ce^{3+} could be a recombination center. So the activity decreased.

Future plans

In order enhance the visible light absorption, we will construction of cerium dioxide – based heterojunctions by utilizing the nano – flake, nano – spindle, and hollow structure cerium dioxide materials.

One visible light responding material, g – C_3N_4, can be as a candidate for combining with CeO_2. We have prepared a new g – C_3N_4 materials with excellent and long range of visible absorption, which can enhance the activity by constructing the heterojunctions.

References

[1] A. Fujishima, K. Honda, Electrochemical Photolysis of Water at a Semiconductor Electrode, Nature, 238 (1972) 37.

[2] N. Murakami, N. Takebe, T. Tsubota, T. Ohno, Improvement of visible light photocatalytic acetaldehyde decomposition of bismuth vanadate/silica nanocomposites by cocatalyst loading, Journal of hazardous materials, 211-212 (2012) 83-87.

[3] S. Kitano, K. Hashimoto, H. Kominami, Photocatalytic mineralization of volatile organic compounds over commercial titanium(IV) oxide modified with rhodium(III) ion under visible light irradiation and correlation between physical properties and photocatalytic activity, Catalysis Today, 164 (2011) 404-409.

[4] T. Ohno, TiO_2-Photocatalyzed Epoxidation of 1-Decene by H_2O_2 under Visible Light, Journal of Catalysis, 204 (2001) 163-168.

[5] M.G. Méndez-Medrano, E. Kowalska, A. Lehoux, A. Herissan, B. Ohtani, D. Bahena, V. Briois, C. Colbeau-Justin, J.L. Rodríguez-López, H. Remita, Surface Modification of TiO_2 with Ag Nanoparticles and CuO Nanoclusters for Application in Photocatalysis, The Journal of Physical Chemistry C, 120 (2016) 5143-5154.

[6] H. Kato, Y. Sasaki, N. Shirakura, A. Kudo, Synthesis of highly active rhodium-doped $SrTiO_3$ powders in Z-scheme systems for visible-light-driven photocatalytic overall water splitting, Journal of Materials Chemistry A, 1 (2013) 12327-12333.

[7] S. Yuan, Q. Zhang, B. Xu, Z. Jin, Y. Zhang, Y. Yang, M. Zhang, T. Ohno, Porous cerium dioxide hollow spheres and their photocatalytic performance, RSC Adv., 4 (2014) 62255-62261.

[8] W. Gao, Z. Zhang, J. Li, Y. Ma, Y. Qu, Surface engineering on CeO_2 nanorods by chemical redox etching and their enhanced catalytic activity for CO oxidation, Nanoscale, 7 (2015) 11686-11691.

[9] T.S. Wu, Y. Zhou, R.F. Sabirianov, W.N. Mei, Y.L. Soo, C.L. Cheung, X-ray absorption study of ceria nanorods promoting the disproportionation of hydrogen peroxide, Chem Commun (Camb), 52 (2016) 5003-5006.

[10] X. Wang, K. Maeda, A. Thomas, K. Takanabe, G. Xin, J.M. Carlsson, K. Domen, M. Antonietti, A metal-free polymeric photocatalyst for hydrogen production from water under visible light, Nature materials, 8 (2009) 76-80.

[11] M. Asadullah, K. Fujimoto, K. Tomishige, Catalytic Performance of Rh/CeO_2 in the Gasification of Cellulose to Synthesis Gas at Low Temperature, Industrial & Engineering Chemistry Research, 40 (2001) 5894-5900.

[12] L. Liao, H.X. Mai, Q. Yuan, H.B. Lu, J.C. Li, C. Liu, C.H. Yan, Z.X. Shen, T. Yu, Single CeO_2 Nanowire Gas Sensor Supported with Pt Nanocrystals: Gas Sensitivity, Surface Bond States, and Chemical Mechanism, The Journal of Physical Chemistry C, 112 (2008) 9061-9065.

[13] H.-P. Zhou, H.-S. Wu, J. Shen, A.-X. Yin, L.-D. Sun, C.-H. Yan, Thermally Stable Pt/CeO_2 Hetero-Nanocomposites with High Catalytic Activity, Journal of the American Chemical Society, 132 (2010) 4998-4999.

[14] A.M. da Silva, K.R. de Souza, G. Jacobs, U.M. Graham, B.H. Davis, L.V. Mattos, F.B. Noronha, Steam and CO_2 reforming of ethanol over Rh/CeO_2 catalyst, Applied Catalysis B-Environmental, 102 (2011) 94-109.

[15] A. Tanaka, K. Hashimoto, H. Kominami, Selective photocatalytic oxidation of aromatic alcohols to aldehydes in an aqueous suspension of gold nanoparticles supported on cerium(IV) oxide under irradiation of green light, Chem Commun (Camb), 47 (2011) 10446-10448.

[16] X. Du, D. Zhang, L. Shi, R. Gao, J. Zhang, Morphology Dependence of Catalytic Properties of Ni/CeO_2 Nanostructures for Carbon Dioxide Reforming of Methane, The Journal of Physical Chemistry C, 116 (2012) 10009-10016.

[17] R. Verma, S.K. Samdarshi, In Situ Decorated Optimized CeO2on Reduced Graphene Oxide with Enhanced Adsorptivity and Visible Light Photocatalytic Stability and Reusability, The Journal of Physical Chemistry C, 120 (2016) 22281-22290.

[18] M.J. Muñoz-Batista, M. Fernández-García, A. Kubacka, Promotion of CeO2–TiO2 photoactivity by $g\text{-}C_3N_4$: Ultraviolet and visible light elimination of toluene, Applied Catalysis B: Environmental, 164 (2015) 261-270.

[19] D. Gao, Y. Zhang, Z. Zhou, F. Cai, X. Zhao, W. Huang, Y. Li, J. Zhu, P. Liu, F. Yang, G. Wang, X. Bao, Enhancing CO_2 Electroreduction with the Metal-Oxide Interface, J Am Chem Soc, 139 (2017) 5652-5655.

[20] P. Li, Y. Zhou, Z. Zhao, Q. Xu, X. Wang, M. Xiao, Z. Zou, Hexahedron Prism-Anchored Octahedronal CeO_2: Crystal Facet-Based Homojunction Promoting Efficient Solar Fuel Synthesis, J Am Chem Soc, 137 (2015) 9547-9550.

[21] A. Tanaka, K. Hashimoto, H. Kominami, Preparation of Au/CeO_2 exhibiting strong surface plasmon resonance effective for selective or chemoselective oxidation of alcohols to aldehydes or ketones in aqueous suspensions under irradiation by green light, J Am Chem Soc, 134 (2012) 14526-14533.

[22] L. Vivier, D. Duprez, Ceria-based solid catalysts for organic chemistry, ChemSusChem, 3 (2010) 654-678.

[23] T. Montini, M. Melchionna, M. Monai, P. Fornasiero, Fundamentals and Catalytic Applications of CeO_2-Based Materials, Chemical reviews, 116 (2016) 5987-6041.

[24] C.M. Ho, J.C. Yu, T. Kwong, A.C. Mak, S.Y. Lai, Morphology-controllable synthesis of mesoporous CeO_2 nano- and microstructures, Chemistry of Materials, 17 (2005) 4514-4522.

[25] S.W. Yang, L. Gao, Controlled synthesis and self-assembly of CeO_2 nanocubes, Journal of the American Chemical Society, 128 (2006) 9330-9331.

[26] H. Gu, M.D. Soucek, Preparation and characterization of monodisperse cerium oxide nanoparticles in hydrocarbon solvents, Chemistry of Materials, 19 (2007) 1103-1110.

[27] M.K. Devaraju, S. Yin, T. Sato, Morphology Control of Cerium Oxide Particles Synthesized via a Supercritical Solvothermal Method, ACS Appl. Mater. Interfaces, 1 (2009) 2694-2698.

[28] H. Imagawa, S. Sun, Controlled Synthesis of Monodisperse CeO_2 Nanoplates Developed from Assembled Nanoparticles, The Journal of Physical Chemistry C, 116 (2012) 2761-2765.

[29] Y. Li, X. He, J.J. Yin, Y. Ma, P. Zhang, J. Li, Y. Ding, J. Zhang, Y. Zhao, Z. Chai, Z. Zhang, Acquired superoxide-scavenging ability of ceria nanoparticles, Angewandte Chemie, 54 (2015) 1832-1835.

[30] K. Zhou, X. Wang, Q. Peng, Y. Li, Enhanced catalytic activity of ceria nanorods from well-defined reactive crystal planes, Journal of Catalysis, 229 (2005) 206-212.

[31] Q. Wu, F. Zhang, P. Xiao, H. Tao, X. Wang, Z. Hu, Y. Lü, Great Influence of Anions for Controllable Synthesis of CeO_2 Nanostructures: From Nanorods to Nanocubes, The Journal of Physical Chemistry C, 112 (2008) 17076-17080.

[32] W. Gao, J. Li, X. Zhou, Z. Zhang, Y. Ma, Y. Qu, Repeatable fluorescence switcher of Eu^{3+}-doped CeO2nanorods byl(+)-ascorbic acid and hydrogen peroxide, J. Mater. Chem. C, 2 (2014) 8729-8735.

[33] M.M. Khan, S.A. Ansari, D. Pradhan, D.H. Han, J. Lee, M.H. Cho, Defect-Induced Band Gap Narrowed CeO2Nanostructures for Visible Light Activities, Industrial & Engineering Chemistry Research, 53 (2014) 9754-9763.

[34] Z. Guo, F. Du, G. Li, Z. Cui, Synthesis and Characterization of Single-Crystal $Ce(OH)CO_3$ and CeO_2 Triangular Microplates, Inorganic Chemistry, 45 (2006) 4167-4169.

[35] T. Yu, B. Lim, Y.N. Xia, Aqueous-Phase Synthesis of Single-Crystal Ceria Nanosheets, Angew. Chem.-Int. Edit., 49 (2010) 4484-4487.

[36] C.R. Li, Q.T. Sun, N.P. Lu, B.Y. Chen, W.J. Dong, A facile route for the fabrication of CeO_2 nanosheets via controlling the morphology of $CeOHCO_3$ precursors, Journal of Crystal Growth, 343 (2012) 95-100.

[37] Q. Dai, S. Bai, H. Li, W. Liu, X. Wang, G. Lu, Template-free and non-hydrothermal synthesis of CeO_2 nanosheets via a facile aqueous-phase precipitation route with catalytic oxidation properties, CrystEngComm, 16 (2014) 9817-9827.

[38] A. Corma, P. Atienzar, H. Garcia, J.Y. Chane-Ching, Hierarchically mesostructured doped CeO_2 with potential for solar-cell use, Nature materials, 3 (2004) 394-397.

[39] C.W. Sun, J. Sun, G.L. Xiao, H.R. Zhang, X.P. Qiu, H. Li, L.Q. Chen, Mesoscale organization of nearly monodisperse flowerlike ceria microspheres, Journal of Physical Chemistry B, 110 (2006) 13445-13452.

[40] L. Guicun, C. Kun, P. Hongrui, C. Kezheng, Z. Zhikun, Facile synthesis of $CePO_4$ nanowires attached to CeO_2 octahedral micrometer crystals and their enhanced photoluminescence properties, Journal of Physical Chemistry C, 112 (2008) 16452-16456.

[41] L. Yan, R. Yu, J. Chen, X. Xing, Template-free hydrothermal synthesis of CeO_2 nano-octahedrons and nanorods: Investigation of the morpholog evolution, Crystal Growth & Design, 8 (2008) 1474-1477.

[42] S. Kim, J.S. Lee, C. Mitterbauer, Q.M. Ramasse, M.C. Sarahan, N.D. Browning, H.J. Park, Anomalous Electrical Conductivity of Nanosheaves of CeO_2, Chemistry of Materials, 21 (2009) 1182-1186.

[43] S.K. Meher, G.R. Rao, Polymer-Assisted Hydrothermal Synthesis of Highly Reducible Shuttle-Shaped CeO_2: Microstructural Effect on Promoting Pt/C for Methanol Electrooxidation, ACS Catalysis, 2 (2012) 2795-2809.

[44] C. Zhang, F. Meng, L. Wang, Controlled synthesis and magnetic properties of bowknot-like CeO_2 microstructures by a CTAB-assisted hydrothermal method, Materials Letters, 119 (2014) 1-3.

[45] D.G. Shchukin, R.A. Caruso, Template Synthesis and Photocatalytic Properties of Porous Metal Oxide Spheres Formed by Nanoparticle Infiltration, Chemistry of Materials, 16 (2004) 2287-2292.

[46] C. Tang, Y. Bando, D. Golberg, R. Ma, Cerium phosphate nanotubes: synthesis, valence state, and optical properties, Angewandte Chemie, 44 (2005) 576-579.

[47] M.M. Titirici, M. Antonietti, A. Thomas, A generalized synthesis of metal oxide hollow spheres using a hydrothermal approach, Chemistry of Materials, 18 (2006) 3808-3812.

[48] G. Chen, C. Xu, X. Song, W. Zhao, Y. Ding, S. Sun, Interface Reaction Route to Two Different Kinds of CeO_2 Nanotubes, Inorganic Chemistry, 47 (2007) 723-728.

[49] M. Guan, J. Sun, M. Han, Z. Xu, F. Tao, G. Yin, X. Wei, J. Zhu, X. Jiang, Synthesis and luminescence of $CePO_4$ and $CePO_4$:Tb hollow and core–shell microspheres composed of single-crystal nanorods, Nanotechnology, 18 (2007) 415602.

[50] C.X. Guozhu Chen, Xinyu Song, Shuling Xu, Yi Ding, and Sixiu Sun, Template-free Synthesis of Single-Crystalline-like CeO_2 Hollow Nanocubes, Crystal Growth and Design, 8 (2008) 4449–4453.

[51] I.A. Kartsonakis, P. Liatsi, I. Daniilidis, G. Kordas, Synthesis, Characterization, and Antibacterial Action of Hollow Ceria Nanospheres with/without a Conductive Polymer Coating, Journal of the American Ceramic Society, 91 (2008) 372-378.

[52] X. Liang, X. Wang, Y. Zhuang, B. Xu, S. Kuang, Y. Li, Formation of CeO_2—ZrO_2 Solid Solution Nanocages with Controllable Structures via Kirkendall Effect, Journal of the American Chemical Society, 130 (2008) 2736-2737.

[53] G. Chen, S. Sun, X. Sun, W. Fan, T. You, Formation of CeO_2 Nanotubes from $Ce(OH)CO_3$ Nanorods through Kirkendall Diffusion, Inorganic Chemistry, 48 (2009) 1334-1338.

[54] N.C. Strandwitz, G.D. Stucky, Hollow Microporous Cerium Oxide Spheres Templated By Colloidal Silica, Chemistry of Materials, 21 (2009) 4577-4582.

[55] C.-Y. Cao, Z.-M. Cui, C.-Q. Chen, W.-G. Song, W. Cai, Ceria Hollow Nanospheres Produced by a Template-Free Microwave-Assisted Hydrothermal Method for Heavy Metal Ion Removal and Catalysis, The Journal of Physical Chemistry C, 114 (2010) 9865-9870.
[56] X. Liang, J.J. Xiao, B.H. Chen, Y.D. Li, Catalytically Stable and Active CeO2 Mesoporous Spheres, Inorganic Chemistry, 49 (2010) 8188-8190.
[57] Y. Song, J. Wei, Y. Yang, Z. Yang, H. Yang, Preparation of CeO_2 hollow spheres via a surfactant-assisted solvothermal route, Journal of Materials Science, 45 (2010) 4158-4162.
[58] Z. Yang, D. Han, D. Ma, H. Liang, L. Liu, Y. Yang, Fabrication of Monodisperse CeO_2 Hollow Spheres Assembled by Nano-octahedra, Crystal Growth & Design, 10 (2010) 291-295.
[59] Z. Yang, L. Liu, H. Liang, H. Yang, Y. Yang, One-pot hydrothermal synthesis of CeO_2 hollow microspheres, Journal of Crystal Growth, 312 (2010) 426-430.
[60] Z. Yang, J. Wei, H. Yang, L. Liu, H. Liang, Y. Yang, Mesoporous CeO_2 Hollow Spheres Prepared by Ostwald Ripening and Their Environmental Applications, European Journal of Inorganic Chemistry, 2010 (2010) 3354-3359.
[61] F.Z. Guozhu Chen, Xuan Sun,Sixiu Sun and Ruiping Chen, Benign synthesis of ceria hollow nanocrystals by a template-free method, CrystEngComm, 13 (2011) 2904-2908.
[62] Z.-R. Tang, Y. Zhang, Y.-J. Xu, A facile and high-yield approach to synthesize one-dimensional CeO_2 nanotubes with well-shaped hollow interior as a photocatalyst for degradation of toxic pollutants, RSC Advances, 1 (2011) 1772.
[63] L. Han, R. Liu, C. Li, H. Li, C. Li, G. Zhang, J. Yao, Controlled synthesis of double-shelled CeO_2 hollow spheres and enzyme-free electrochemical bio-sensing properties for uric acid, Journal of Materials Chemistry, 22 (2012) 17079.
[64] M. Kempaiah Devaraju, X. Liu, S. Yin, T. Sato, A rapid solvothermal synthesis of cerium oxide hollow spheres and characterization, Journal of Solid State Chemistry, 194 (2012) 43-47.
[65] Y. Jiao, F. Wang, X. Ma, Q. Tang, K. Wang, Y. Guo, L. Yang, Facile one-step synthesis of porous ceria hollow nanospheres for low temperature CO oxidation, Microporous and Mesoporous Materials, 176 (2013) 1-7.
[66] S. Liu, M. Xie, X. Guo, W. Ji, Synthesis of CeO_2 hollow nanospheres via redox reaction based self-templating approach, Materials Letters, 105 (2013) 192-195.

[67] X. Liu, H. Yang, L. Han, W. Liu, C. Zhang, X. Zhang, S. Wang, Y. Yang, Mesoporous-shelled CeO_2 hollow nanospheres synthesized by a one-pot hydrothermal route and their catalytic performance, CrystEngComm, 15 (2013) 7769.

[68] L. Wang, F. Liu, W. Yang, H. Zhao, Y. Zheng, X. Chen, W. Dong, Synthesis of multiple-shell porous CeO_2 hollow spheres by a hydrogel template method, Materials Letters, 107 (2013) 42-45.

[69] S. Yan, S. Ma, X. Xu, Y. Lu, H. Bian, X. Liang, W. Jin, H. Yang, Synthesis and gas sensing application of porous CeO_2–ZnO hollow fibers using cotton as biotemplates, Materials Letters, 165 (2016) 9-13.

[70] X.W. Liu, K.B. Zhou, L. Wang, B.Y. Wang, Y.D. Li, Oxygen Vacancy Clusters Promoting Reducibility and Activity of Ceria Nanorods, Journal of the American Chemical Society, 131 (2009) 3140-3141.

[71] Z. Wu, M. Li, J. Howe, H.M. Meyer, 3rd, S.H. Overbury, Probing defect sites on CeO_2 nanocrystals with well-defined surface planes by Raman spectroscopy and O_2 adsorption, Langmuir, 26 (2010) 16595-16606.

[72] N. Skorodumova, R. Ahuja, S. Simak, I. Abrikosov, B. Johansson, B. Lundqvist, Electronic, bonding, and optical properties of CeO_2 and Ce_2O_3 from first principles, Physical Review B, 64 (2001).

[73] N.V. Skorodumova, S.I. Simak, B.I. Lundqvist, I.A. Abrikosov, B. Johansson, Quantum origin of the oxygen storage capability of ceria, Phys Rev Lett, 89 (2002) 166601.

[74] N.V. Skorodumova, M. Baudin, K. Hermansson, Surface properties of CeO_2 from first principles, Physical Review B, 69 (2004).

[75] M. Nolan, S.C. Parker, G.W. Watson, The electronic structure of oxygen vacancy defects at the low index surfaces of ceria, Surface Science, 595 (2005) 223-232.

[76] H.-T. Chen, First-Principles Study of CO Adsorption and Oxidation on Ru-Doped CeO_2(111) Surface, The Journal of Physical Chemistry C, 116 (2012) 6239-6246.

[77] H.-J. Lin, J.-J. Tang, Q. Yu, H. Wang, L.-Z. Ouyang, Y.-J. Zhao, J.-W. Liu, W.-H. Wang, M. Zhu, Symbiotic $CeH_{2.73}/CeO_2$ catalyst: A novel hydrogen pump, Nano Energy, 9 (2014) 80-87.

[78] N. Kumari, N. Sinha, M.A. Haider, S. Basu, CO_2 Reduction to Methanol on CeO_2 (110) Surface: a Density Functional Theory Study, Electrochimica Acta, 177 (2015) 21-29.

[79] S.S. Pramana, T. Baikie, T. An, M.G. Tucker, J. Wu, M.K. Schreyer, F. Wei, R.D. Bayliss, C.L. Kloc, T.J. White, A.P. Horsfield, S.J. Skinner, Correlation of Local Structure and Diffusion Pathways in the Modulated Anisotropic Oxide Ion Conductor $CeNbO_{4.25}$, J Am Chem Soc, 138 (2016) 1273-1279.

[80] H. Wu, S. Ma, W. Song, E.J.M. Hensen, Density Functional Theory Study of the Mechanism of Formaldehyde Oxidation on Mn-Doped Ceria, The Journal of Physical Chemistry C, 120 (2016) 13071-13077.

[81] S. Yang, L. Gao, Controlled Synthesis and Self-Assembly of CeO_2 Nanocubes, Journal of the American Chemical Society, 128 (2006) 9330-9331.

[82] X. Liu, K. Zhou, L. Wang, B. Wang, Y. Li, Oxygen Vacancy Clusters Promoting Reducibility and Activity of Ceria Nanorods, Journal of the American Chemical Society, 131 (2009) 3140-3141.

[83] X. Lu, T. Zhai, H. Cui, J. Shi, S. Xie, Y. Huang, C. Liang, Y. Tong, Redox cycles promoting photocatalytic hydrogen evolution of CeO_2 nanorods, Journal of Materials Chemistry, 21 (2011) 5569.

[84] K. Otsuka, M. Hatano, A. Morikawa, Hydrogen from Water by Reduced Cerium Oxide, Journal of Catalysis, 79 (1983) 493-496.

[85] Y. Madier, C. Descorme, A.M. Le Govic, D. Duprez, Oxygen Mobility in CeO_2 and $Ce_xZr_{(1-x)}O_2$ Compounds: Study by CO Transient Oxidation and $^{18}O/^{16}O$ Isotopic Exchange, The Journal of Physical Chemistry B, 103 (1999) 10999-11006.

[86] T. Bansagi, T.S. Zakar, F. Solymosi, An FTIR study on the formation of NCO surface complexes over Rh/CeO_2, Applied Catalysis B-Environmental, 66 (2006) 147-150.

[87] J. Ahn, S. Choi, K.J. Yoon, J.W. Son, B.K. Kim, J.H. Lee, H.W. Jang, H. Kim, Strain-Induced Tailoring of Oxygen-Ion Transport in Highly Doped CeO_2 Electrolyte: Effects of Biaxial Extrinsic and Local Lattice Strain, ACS Applied Materials and Interfaces, 9 (2017) 42415-42419.

[88] H. Dai, Y. Ning, S. He, X. Zhang, L. Guo, G. Zhao, Surface Modification Allows High Performance for Solid Oxide Fuel Cells Fabricated by a Single-step Co-firing Process, Fuel Cells, 17 (2017) 905-908.

[89] Y. Polat, M. Ar**ı**, Y. Da**ğ**demir, Phase stability, thermal, electrical and structural properties of $(Bi_2O_3)_1(Sm_2O_3)(CeO_2)_y$ electrolytes for solid oxide fuel cells, Phase Transitions, 90 (2017) 387-398.

[90] S.S.B. Che Abdullah, T. Teranishi, H. Hayashi, A. Kishimoto, Millimeter-wave irradiation heating for operation of doped CeO_2 electrolyte-supported single solid oxide fuel cell, Journal of Power Sources, 374 (2018) 92-96.

[91] C. Artini, M. Pani, M.M. Carnasciali, J.R. Plaisier, G.A. Costa, Lu-, Sm-, and Gd-Doped Ceria: A Comparative Approach to Their Structural Properties, Inorganic Chemistry, 55 (2016) 10567-10579.

[92] C. Rhodes, S. Franzen, J.P. Maria, M. Losego, D.N. Leonard, B. Laughlin, G. Duscher, S. Weibel, Surface plasmon resonance in conducting metal oxides, Journal of Applied Physics, 100 (2006) 054905.

[93] C. Rhodes, M. Cerruti, A. Efremenko, M. Losego, D.E. Aspnes, J.P. Maria, S. Franzen, Dependence of plasmon polaritons on the thickness of indium tin oxide thin films, Journal of Applied Physics, 103 (2008) 093108.

[94] M. Kanehara, H. Koike, T. Yoshinaga, T. Teranishi, Indium Tin Oxide Nanoparticles with Compositionally Tunable Surface Plasmon Resonance Frequencies in the Near-IR Region, Journal of the American Chemical Society, 131 (2009) 17736-17737.

[95] T.R. Gordon, M. Cargnello, T. Paik, F. Mangolini, R.T. Weber, P. Fornasiero, C.B. Murray, Nonaqueous synthesis of TiO_2 nanocrystals using TiF4 to engineer morphology, oxygen vacancy concentration, and photocatalytic activity, J Am Chem Soc, 134 (2012) 6751-6761.

[96] K. Manthiram, A.P. Alivisatos, Tunable localized surface plasmon resonances in tungsten oxide nanocrystals, J Am Chem Soc, 134 (2012) 3995-3998.

[97] L. De Trizio, R. Buonsanti, A.M. Schimpf, A. Llordes, D.R. Gamelin, R. Simonutti, D.J. Milliron, Nb-Doped Colloidal TiO_2 Nanocrystals with Tunable Infrared Absorption, Chemistry of Materials, 25 (2013) 3383-3390.

[98] T.R. Gordon, T. Paik, D.R. Klein, G.V. Naik, H. Caglayan, A. Boltasseva, C.B. Murray, Shape-dependent plasmonic response and directed self-assembly in a new semiconductor building block, indium-doped cadmium oxide (ICO), Nano letters, 13 (2013) 2857-2863.

[99] K. Jongbum, G.V. Naik, N.K. Emani, U. Guler, A. Boltasseva, Plasmonic Resonances in Nanostructured Transparent Conducting Oxide Films, IEEE Journal of Selected Topics in Quantum Electronics, 19 (2013) 4601907-4601907.

[100] M.M. Alsaif, K. Latham, M.R. Field, D.D. Yao, N.V. Medhekar, G.A. Beane, R.B. Kaner, S.P. Russo, J.Z. Ou, K. Kalantar-zadeh, Tunable plasmon resonances in two-dimensional molybdenum oxide nanoflakes, Adv Mater, 26 (2014) 3931-3937.

[101] H. Matsui, S. Furuta, H. Tabata, Role of electron carriers on local surface plasmon resonances in doped oxide semiconductor nanocrystals, Applied Physics Letters, 104 (2014) 211903.

[102] H. Cheng, X. Qian, Y. Kuwahara, K. Mori, H. Yamashita, A Plasmonic Molybdenum Oxide Hybrid with Reversible Tunability for Visible-Light-Enhanced Catalytic Reactions, Adv Mater, 27 (2015) 4616-4621.

[103] A.M. Schimpf, S.D. Lounis, E.L. Runnerstrom, D.J. Milliron, D.R. Gamelin, Redox chemistries and plasmon energies of photodoped In2O3 and Sn-doped In_2O_3 (ITO) nanocrystals, J Am Chem Soc, 137 (2015) 518-524.

[104] H. Cheng, M. Wen, X. Ma, Y. Kuwahara, K. Mori, Y. Dai, B. Huang, H. Yamashita, Hydrogen Doped Metal Oxide Semiconductors with Exceptional and Tunable Localized Surface Plasmon Resonances, J Am Chem Soc, 138 (2016) 9316-9324.

[105] X. Tan, L. Wang, C. Cheng, X. Yan, B. Shen, J. Zhang, Plasmonic MoO_{3-x}@MoO_3 nanosheets for highly sensitive SERS detection through nanoshell-isolated electromagnetic enhancement, Chem Commun (Camb), 52 (2016) 2893-2896.

[106] R.W. Johns, M.A. Blemker, M.S. Azzaro, S. Heo, E.L. Runnerstrom, D.J. Milliron, S.T. Roberts, Charge carrier concentration dependence of ultrafast plasmonic relaxation in conducting metal oxide nanocrystals, J. Mater. Chem. C, 5 (2017) 5757-5763.

[107] Y. Li, J. Cheng, Y. Liu, P. Liu, W. Cao, T. He, R. Chen, Z. Tang, Manipulation of Surface Plasmon Resonance in Sub-Stoichiometry Molybdenum Oxide Nanodots through Charge Carrier Control Technique, The Journal of Physical Chemistry C, 121 (2017) 5208-5214.

[108] W. Liu, Q. Xu, W. Cui, C. Zhu, Y. Qi, CO2 -Assisted Fabrication of Two-Dimensional Amorphous Molybdenum Oxide Nanosheets for Enhanced Plasmon Resonances, Angewandte Chemie, 56 (2017) 1600-1604.

Achievement

Publications

[1] **Sàisài Yuán**, Bin Xu, Qitao Zhang, Sixiao Liu, Ju Xie, Ming Zhang and Teruhisa Ohno, Development of visible light response of CeO_{2-x} with the high content of Ce^{3+} and its photocatalytic property, ChemCatChem, DOI: 10.1002/cctc.201701767.

[2] **Saisai Yuan**, Qitao Zhang, Bin Xu, Sixiao Liu, Jinquan Wang, Ju Xie, Ming Zhang and Teruhisa Ohno, A new precursor to synthesize g-C_3N_4 with superior visible light absorption for photocatalytic application, catalysis science & technology, 7 (2017) 1826-1830. (Inside back cover)

[3] **S. Yuan**, Q. Zhang, B. Xu, Z. Jin, Y. Zhang, Y. Yang, M. Zhang, T. Ohno, Porous cerium dioxide hollow spheres and their photocatalytic performance, RSC Advances., 4 (2014) 62255-62261.

[4] **Qitao Zhang‡, Saisai Yuan‡**, Bin Xu, Yangsen Xu, Kuanhong Cao, Zhengyuan Jin, Ming Zhang, Chenliang Su, Teruhisa Ohno, A facile approach to build $Bi_2O_2CO_3$/PCN nanohybrid photocatalysts for gaseous acetaldehyde efficiently removal, Catalysis Today. (Under review, co-first author)

[5] J.Q. Wang, X.H. Wu, Y.Y. Wu, **S.S. Yuan**, Y.M. Xu, X.B. Chen, M. Zhang, Fabrication and Characterization of Tin Oxide Inverse Opal by Template Method, Key Engineering Materials, 562-565 (2013) 18-21.

[6] Y. Zhang, Y. Zhao, **S. Yuan**, H. Wang, C. He, Electrocatalysis and detection of nitrite on a reduced graphene/Pd nanocomposite modified glassy carbon electrode, Sensors and Actuators B: Chemical, 185 (2013) 602-607.

[7] Q. Zhang, B. Xu, **S. Yuan**, M. Zhang, T. Ohno, Fabrication and characterization of sesame ball-like CeO_2:Y^{3+}/P(St–AA) composite microspheres based on electrostatic interaction, Materials Letters, 121 (2014) 109-112.

[8] Y. Zhang, **S. Yuan**, Y. Zhao, H. Wang, C. He, Synthesis of novel yttrium-doped graphene oxide nanocomposite for dye removal, Journal of Materials Chemistry A, 2 (2014) 7897.

[9] Q. Huang, Q. Zhang, **S. Yuan**, Y. Zhang, M. Zhang, One-pot facile synthesis of branched Ag-ZnO heterojunction nanostructure as highly efficient photocatalytic catalyst, Applied Surface Science, 353 (2015) 949-957.

[10] Z. Jin, Q. Zhang, **S. Yuan**, T. Ohno, Synthesis high specific surface area nanotube g-C_3N_4 with two-step condensation treatment of melamine to enhance photocatalysis properties, RSC Advances, 5 (2015) 4026-4029.

[11] T. Ohno, T. Higo, H. Saito, **S. Yuan**, Z. Jin, Y. Yang, T. Tsubota, Dependence of photocatalytic activity on aspect ratio of a brookite TiO_2 nanorod and drastic improvement in visible light responsibility of a brookite TiO_2 nanorod by site-selective modification of Fe^{3+} on exposed faces, Journal of Molecular Catalysis A: Chemical, 396 (2015) 261-267.

[12] B. Xu, Q. Zhang, **S. Yuan**, M. Zhang, T. Ohno, Morphology control and photocatalytic characterization of yttrium-doped hedgehog-like CeO_2, Applied Catalysis B: Environmental, 164 (2015) 120-127.

[13] B. Xu, Q. Zhang, **S. Yuan**, M. Zhang, T. Ohno, Morphology control and characterization of broom-like porous CeO_2, Chemical Engineering Journal, 260 (2015) 126-132.

[14] B. Xu, Q. Zhang, **S. Yuan**, M. Zhang, T. Ohno, Synthesis and photocatalytic performance of yttrium-doped CeO_2 with a porous broom-like hierarchical structure, Applied Catalysis B: Environmental, 183 (2016) 361-370.

[15] B. Xu, Q. Zhang, **S. Yuan**, S. Liu, M. Zhang, T. Ohno, Synthesis and photocatalytic performance of yttrium-doped CeO_2 with a hollow sphere structure, Catalysis Today, 281 (2017) 135-143.

[16] Q. Zhang, B. Xu, **S. Yuan**, M. Zhang, T. Ohno, Improving g-C_3N_4 photocatalytic performance by hybridizing with $Bi_2O_2CO_3$ nanosheets, Catalysis Today, 284 (2017) 27-36.

Conferences

[a] **Saisai Yuan,** Ming Zhang, Ohno Teruhisa, The photocatalysis of ceria enhanced with monodisperse hollow spheres structure synthesized by one-sep template - free method, The 33th photo catalyzed chemistry symposium, 2014.7.18, Tokyo. (Poster)

[b] **Saisai Yuan**, Preparation of reduced CeO_{2-x} and their photocatalytic performance depending with the content of Ce^{3+}, The 6th Student WorkShop Between YZU-KIT, 2017.3.27, Kitakyushu. (Session Chair)

[c] **Saisai Yuan**, The 2th Beijing Kein Primary Quantum Chemistry Seminar, 2017.4.26 – 29, Beijing.

[d] **Yuan Saisai**, Zhang Ming, Ohno Teruhisa, Development of visible light response of CeO_{2-x} by controlling the contents of Ce^{3+} and its photocatalytic property, The 7th ChinaNano, 2017.8.29 -31, 4P-045, Beijing. (Poster)

Acknowledgments

First of all, I would like to acknowledge the financial support of funding agencies for my Ph.D. research: CHINA SHCOLARSHIP COUNCIL (No. 201608320207).

I gratefully acknowledge my supervisors, Professor Ming Zhang and Professor Teruhisa Ohno. Their supports, guidance and training enable me to complete my doctoral studies at the Yangzhou University and Kyushu Institute of Technology. I thank my committee members, Associate Professor Toshiki Tsubota, Professor Youichi SHIMIZU, and Professor Hiroyuki DEGUCHI for their support, inspiration, encouragement and helpful critiques on my research work. Furthermore, I am grateful to my current group mates: Qitao Zhang, Bin Xu, Sixiao Liu, Szuying Lee and my friends for their help and support.

Finally, I would like to dedicate this dissertation to my beloved wife and my parents who always trust and support me. They help me make the best decisions. Their love, encouragement and care enable me to finish my doctoral study.